ALMA MATER STUDIORUM · UNIVERSITÀ DI BOLOGNA

Scuola di Scienze
Dipartimento di Fisica e Astronomia
Corso di Laurea Magistrale in Astrofisica e Cosmologia

X-ray analysis and broad-band properties of [NeV]-selected type 2 AGN

TESI di LAUREA MAGISTRALE

Relatore:
Chiar.mo Prof.
Cristian Vignali

Presentata da:
Luigi Barchiesi

Co-relatori:
Dott. Roberto Gilli

Dott. Marco Mignoli

Dott.ssa Francesca Pozzi

Contents

Abstract

The study of obscured (type 2) Active Galactic Nuclei (AGN) is fundamental to the understanding of the evolution phases of AGN and of their influence on galaxy evolution. Some models (e.g., Hopkins et al. 2007) predict a phase during which AGN are enshrouded by a large amount of gas and dust, thus appearing as obscured sources. Studying such phase and how the AGN gets rid of the surrounding material is crucial to test and possibly understand the AGN-galaxy co-evolution scenario. Furthermore, AGN are the main contributors to the X-ray background (XRB); population synthesis models predict that the as yet unresolved XRB emission at $E \sim 30$ keV could be tied to heavily obscured AGN at $z \approx 1$ (Gilli 2013). Hence a census, as complete as possible, of obscured AGN at $z \sim 1$ is needed. The X-ray radiation is a good tracer of the emission of obscured AGN thanks to its high penetrating power; however, when the nucleus is obscured by column densities as large as $\sim 10^{24-25} \mathrm{cm}^{-2}$, even hard X-rays are severely depressed. Therefore, we must rely on other selection methods to identify type 2 AGN. One of them is based on the [O III]5007Å emission line, exploiting the fact that the narrow line region (NLR), where this line comes from, is not hidden by the obscuring material. However, at $z > 0.8$, the [OIII] line is redshifted out of the optical range. Thus, fainter high-ionization lines, like the [NeV]3426Å, which can be observed with optical spectroscopy up to $z \approx 1.5$, have to be used. The [NeV] flux is strictly related to the energy coming from the nucleus of the AGN and is considered a good proxy of the nuclear intrinsic emission. As such, the X/[NeV] ratio can be used to study the obscuration of the AGN, as the observed X-ray flux is correlated to the nuclear emission but also heavily dependent on the source obscuration (Gilli et al. 2010).

The goal of my master thesis project is the study of [NeV]-selected type 2 AGN at $z \approx 1$ in the COSMOS field, through the analysis of their X-ray spectra and optical-to-far-IR spectral energy distributions (SED). This type of analysis has been presented in previous works (Mignoli et al. 2013, Vignali et al. 2014) for the AGN in the C-COSMOS field. Now we are using the new X-ray data from the Chandra COSMOS Legacy catalogue (Civano et al. 2016, Marchesi et al. 2016), that extends the X-ray coverage of the COSMOS field from 0.9 to 2.2 deg² and provides a more uniform coverage. We also aim at studying the hosts of type 2 AGN to characterize their parameters, like stellar mass and star formation rate, and investigate whether these galaxies are different from "normal" galaxies due to the AGN influence.

More in detail, from the 20k zCOSMOS bright survey, 94 [NeV] type 2 AGN were selected (Mignoli et al. 2013); we matched these with the 4016 X-ray sources in the COSMOS Legacy catalogue, obtaining a sample of 36 optically selected AGN with X-ray detection at $z \approx 0.66 - 1.18$. This is an improvement with respect to the previous work that used shallower and less extended (in areal coverage) data, where the matches

were 23. For all the 36 sources we performed an X-ray spectral analysis in the range $E = 0.5 - 7.0$ keV (observed-frame) using two different models: a simple power law and a power law with fixed photon index ($\Gamma = 1.8$, typical of unabsorbed AGN emission) and intrinsic absorption. We used the Hardness Ratio (HR) and synthetic spectra to help us fitting the few sources with ~ 10 counts. We classified 28 of our sources as obscured ($N_H > 10^{22}$ cm^{-2}), 9 of them with $N_H > 10^{23}$ cm^{-2} and 2 as Compton-thick AGN ($N_H > 10^{24}$ cm^{-2}). We obtained a mean value of $L_{2-10 \text{ keV}}^{intr} \approx 5 \cdot 10^{43}$ erg/s, where the intrinsic luminosity of each source was derived taking into account their obscuration. Thanks to the $2 - 10$ keV rest-frame flux we also obtained the X/[NeV] ratio, which we used to obtain a second estimate of the sources obscuration, following Gilli et al. (2010). We obtained absorption values compatible with those from spectral analysis, hence confirming the reliability of the X/[NeV] ratio as obscuration tracer.

We also computed the rest-frame 2 - 10 keV flux upper limits for 58 sources without X-ray detection and used them to derive X/[NeV] upper limits. Thirty-nine sources ($\approx 67\%$) have X/[Ne V] ratios compatible with $N_H > 10^{23}$ cm^{-2}, two of these can be classified as CT AGN. In the X-ray undetected sample there are more obscured sources and they are, on average, more absorbed. Considering the whole [NeV] sample we found that at least half of the sources has $N_H > 10^{23}$ cm^{-2} and at least 4% can be classified as CT objects. These new data will be used to improve the estimate of the fraction of CT AGN at $z \approx 1$ and their contribution to the XRB.

We also performed an analysis of the SED of the sources, in order to characterize both the AGN and their host galaxies. The use of a SED fitting code allowed us to separate the AGN emission, in particular the mid-IR emission ascribed to the obscuring torus, that provided us with an estimate of the AGN bolometric power, from the galaxy emission. We used the latter to estimate the stellar mass (M_*) of the galaxy and the star formation rate (SFR). The average SFR of our sample is $\sim 35 \, M_\odot$/yr, obtained using the SFR-$L_{8-1000\mu m}$ relation (Kennicutt 1998a). We compared our results with those expected from the SFR-M_* at $z = 1$ relation (the "main sequence") observed in non-active galaxies and found that our sources do not differ significantly from "normal" galaxies, hence the AGN has, so far, a limited impact on the host-galaxy SF. We also compared, for the X-ray detected sources, the AGN bolometric luminosity, obtained via SED fitting, with the one obtained from the 2 - 10 keV intrinsic luminosity using the bolometric correction of Lusso et al. (2012). We found that the two luminosities are consistent, within a factor ~ 2.8, and with a mean of $L_{bol} \approx (7.9 \pm 1.7) \cdot 10^{44}$ erg/s ($L_{bol} \approx 6.5 \cdot 10^{44} \pm 1.2$ considering the entire sample). For eight sources the best-fit AGN contribution to the optical-IR SED is negligible, underlining the importance of a multi-wavelength approach to the study of obscured AGN. We found good correlations between the AGN $12 \, \mu$m and $2 - 10$ keV luminosities and between the AGN bolometric luminosities derived from the SED fitting and those from the rest-frame $2 - 10$ keV intrinsic luminosities. These correlations can be used to estimate the AGN power of sources for which X-ray data are either not available or too shallow.

One of the future developments will consist in making more detailed comparisons between our results and those from a sample of galaxies without evident AGN activity, with the aim of investigating further whether the AGN has an influence on the observed properties of their host (e.g. SFR at the same M_*, gas content and temperature), as predicted by AGN-galaxy co-evolution models. Other future plans involve the study of the evolution of obscured AGN properties in the COSMOS field as a function of the redshift. In fact, the use of different narrow, high-ionization lines can allow to selection of obscured AGN in different redshift ranges, i.e. [O III] selects up to $z \sim 0.8$ (Vignali et al. 2010), while C IV up to $z \sim 3$ (Mignoli et al. 2019). At this regard COSMOS is the ideal field to perform spectroscopic selections, as the zCOSMOS survey (Lilly et al. 2007 and 2009) was designed to provides a high and uniform sampling rate across the whole field. The X-ray spectral analysis and optical-IR SED fitting of samples at different redshifts will shed light on the redshift evolution of both the AGN and host-galaxy properties. Finally, the study of the environment around our sources could provide useful insight into the environment influence on the AGN activity and the SF processes.

Lo studio dei Nuclei Galattici Attivi (AGN) oscurati (di tipo 2) è fondamentale per capire le fasi evolutive degli AGN e la loro influenza sull'evoluzione delle galassie. Infatti, alcuni modelli (es. Hopkins et al. 2007) predicono l'esistenza di una fase durante la quale l'AGN è circondato ed oscurato da un'enorme quantità di gas e polvere. Lo studio di questa fase e di come l'AGN se ne libera è cruciale per cercare di comprendere lo scenario di coevoluzione AGN-galassia. Inoltre, gli AGN sono i responsabili principali della radiazione di fondo in banda X (*X-ray background - XRB*); di questo solo una frazione ne è stata risolta in sorgenti singole ad energia superiore a 30 keV. I modelli di sintesi dell'XRB predicono che questa parte ancora irrisolta possa essere dovuta ad AGN estremamente oscurati a $z \approx 1$ (Gilli 2013). Per affrontare questi problemi è fondamentale un censimento quanto più completo possibile di tali sorgenti. La radiazione X risulta essere un buon tracciante dell'emissione degli AGN oscurati, grazie al suo alto potere penetrante; tuttavia, nei casi in cui il nucleo risulta oscurato da densità di colonna oltre $\sim 10^{24-25} \text{cm}^{-2}$, anche la radiazione X è severamente depressa. Di conseguenza, dobbiamo affidarci ad altri metodi per poter identificare gli AGN di tipo 2. Uno di questi si basa sulla selezione tramite la riga in emissione dell'[OIII]5007Å e sfrutta il fatto che la *Narrow Line Region* (NLR) dove si origina questa riga, non è oscurata dal toro di gas e polveri, che invece assorbe la maggior parte dell'emissione proveniente dal nucleo. Tuttavia, per $z > 0.8$, questa riga si trova al di fuori dello banda ottica. Di conseguenza, bisogna affidarsi ad altre, sfortunatamente più deboli, righe ad alta ionizzazione, come il [NeV]3426Å che riesce ad essere osservato tramite spettroscopia ottica fino a $z \approx 1.5$. Inoltre il flusso del [NeV] è strettamente legato all'energia del nucleo che illumina la NLR e risulta, quindi, un buon tracciante dell'emissione intrinseca dell'AGN. Questo permette di usare il rapporto X/[NeV] per studiare l'oscuramento delle sorgenti, in quanto il flusso X osservato è esso stesso legato all'emissione del nucleo, ma subisce altresì gli effetti dell'oscuramento (Gilli et al. 2010).

L'obiettivo del mio lavoro di tesi magistrale consiste nello studio, nel campo COSMOS di un campione di AGN oscurati a $z \approx 1$, selezionato tramite la riga del [NeV]. Tale studio è stato condotto tramite l'analisi degli spettri X ed il fit delle distribuzioni di energia spettrale (SED). Lavori simili sono già stato effettuati (Mignoli et al. 2013, Vignali et al. 2014) utilizzando i dati provenienti della survey C-COSMOS. L'uso di dati dalla nuova survey COSMOS-Legacy (Civano et al. 2016, Marchesi et al. 2016) ci ha permesso di estendere la copertura X all'intero campo COSMOS (si è passati da un campo di 0.9 gradi quadrati ad uno di 2.2) e di avere a disposizione una copertura maggiormente uniforme. Inoltre si intende studiare anche le caratteristiche delle galassie che ospitano AGN di tipo 2, come ad esempio la massa stellare ed il tasso di formazione stellare (SFR) e vedere se l'influenza dell'AGN le differenzia rispetto alle "normali" galassie.

Entrando nel dettaglio, il nostro campione è composto da 94 AGN di tipo 2, selezionati da Mignoli et al. (2013) per la presenza negli spettri della riga stretta del [NeV]

a partire dal catalogo 20k zCOSMOS bright. Abbiamo confrontato queste sorgenti con quelle nel catalogo X COSMOS Legacy, ottenendo un campione di 36 AGN, con redshift compresi tra 0.66 e 1.18, rivelati nella banda X e selezionati in quella ottica. L'uso dei nuovi dati X fornisce un miglioramento rispetto al precedente lavoro che, sfruttando dati meno profondi e che coprivano un'area minore, aveva prodotto solamente 23 sorgenti individuate in entrambi i cataloghi. Per tutte le 36 sorgenti abbiamo effettuato un'analisi degli spettri X tra 0.5 e 7.0 keV (observed frame) tramite due modelli: uno a semplice legge di potenza ed uno a legge di potenza con indice spettrale fisso ($\Gamma = 1.8$, tipico di AGN non oscurati) ed un assorbimento intrinseco. Per aiutarci nel fitting degli spettri delle sorgenti con pochi (~ 10) conteggi abbiamo sfruttato l'*Hardness Ratio* (HR) e la creazione di spettri sintetici. Sulla base dell'assorbimento abbiamo classificato 28 sorgenti come oscurate ($N_H > 10^{22}$ cm^{-2}), 9 come molto oscurate ($N_H > 10^{23}$ cm^{-2}) e due come AGN Compton-thick (CT), ossia con $N_H > 10^{24}$ cm^{-2}. Una volta ricavato l'oscuramento abbiamo potuto calcolare la luminosità intrinseca delle sorgenti, il cui valore medio è $L_{2-10 \text{ keV}}^{intr} \approx 5 \cdot 10^{43}$ erg/s. Tramite il flusso $2-10$ keV (rest-frame) abbiamo ottenuto il rapporto X/[NeV], che abbiamo utilizzato per ottenere una seconda stima dell'oscuramento delle sorgenti, come nel lavoro di Gilli et al. (2010). I valori ricavati dal rapporto X/[NeV] sono in accordo con quelli dell'analisi spettrale, cosa che ci ha permesso di confermare la validità di questo rapporto come tracciante dell'oscuramento.

Per le sorgenti senza rivelazione nella banda X abbiamo calcolato i limiti superiori al loro flusso $2-10$ keV (rest-frame) ed usati per ottenere i limiti del rapporto X/[NeV]. Trentanove sorgenti, circa il 67%, hanno X/[NeV] tipici di sorgenti con $N_H > 10^{23}$ cm^{-2} e due possono essere classificate come oggetti CT. Tipicamente, nel campione senza rivelazione X, troviamo una frazione maggiore di sorgenti oscurate e queste tendono ad avere valori di N_H maggiori. Considerando l'intero campione di 94 AGN, almeno la metà è composto da sorgenti molto oscurate ($N_H > 10^{23}$ cm^{-2}) ed almeno il 4% da sorgenti CT. I nuovi dati che abbiamo prodotto saranno usati per migliorare le stime della frazione di AGN CT a $z \approx 1$ ed il loro contributo all'XRB.

Abbiamo anche effettuato un'analisi delle SED delle sorgenti, per caratterizzarne sia l'AGN che la galassia ospite. L'uso di codici di SED fitting ci ha permesso di separare l'emissione dell'AGN, in particolare quella mid-IR dovuta al toro, che abbiamo usato per ricavare l'emissione bolometrica dell'AGN, da quella galattica. Quest'ultima è stata sfruttata per stimare la M_* e lo SFR. Usando la relazione SFR-$L_{8-1000\mu m}$ (Kennicutt 1998a), abbiamo ottenuto uno SFR medio di $35 \, M_\odot$/yr. Confrontando questi valori con quelli aspettati dalla relazione SFR-M_* a $z = 1$ (la cosiddetta "main sequence"), valida per le galassie non attive, non abbiamo trovato differenze sostanziali, segno che le galassie del nostro campione non differiscono da galasssie "normali" e, di conseguenza, che l'AGN ha avuto per ora un impatto limitato sulla formazione stellare della galassia ospitante. Abbiamo anche confrontato, per le sorgenti con detection X, le luminosità bolometriche ottenute dal SED-fitting, con quelle ottenute grazie alla correzione bolometrica di Lusso et al. (2012) a partire dalle luminosità $2-10$ keV intrinseche. Abbiamo trovato valori

compatibili ed una luminosità media di $L_{bol} \approx 8 \cdot 10^{44}$ erg/s ($L_{bol} \approx 7 \cdot 10^{44}$ se consideriamo anche le sorgenti senza rivelazione X). Per otto sorgenti, il contributo alla SED dell'AGN è trascurabile, cosa che sottolinea l'importanza di un approccio multi-banda allo studio e alla ricerca degli AGN oscurati. È anche emersa la presenza di buone correlazioni tra la luminosità dell'AGN a $12\,\mu$m e $2 - 10$ keV e tra le luminosità bolometriche ottenute dal SED-fitting e dalla luminosità intrinseca. Queste correlazioni possono essere utilizzate per stimare la potenza dell'AGN laddove i dati X non siano disponibili oppure non sono abbastanza profondi.

L'intero lavoro ha sottolineato l'importanza di un approccio multibanda per lo studio delle proprietà degli AGN oscurati; un approccio di questo tipo potrà presto essere applicato sull'intero cielo, per esempio sfruttando dati IR *WISE* e le osservazioni X di *eROSITA*, appena queste saranno rese disponibili.

Uno degli sviluppi futuri di questo lavoro comprende un confronto più approfondito tra i risultati ottenuti e quelli prodotti da una simile analisi su un campione di galassie senza attività di AGN, con l'obiettivo di vedere se, come predetto dallo scenario di coevoluzione AGN-galassia, l'AGN abbia un'influenza osservabile sulle proprietà delle galassie ospiti, come SFR, contenuto di gas e frazioni relative tra le varie fasi del gas. Un altro lavoro si potrebbe basare sullo studio dell'evoluzione con il redshift delle proprietà degli AGN oscurati. Infatti, l'uso di differenti righe strette permette di selezionare AGN a redshift differenti, ad esempio l'[OIII] permette di selezionare fino a $z \sim 0.8$ con spettri ottici, mentre il C IV fino a $z \sim 3$ (Mignoli et al. 2019). A questo proposito COSMOS è il campo ideale per tali selezioni spettroscopiche; infatti la survey zCOSMOS è stata ideata proprio per avere una copertura uniforme sull'intero campo (Lilly et al. 2007 and 2009). Un'analisi spettrale e un SED fitting simili a quelli prodotti da questo lavoro permetterebbero di ricavare l'evoluzione in funzione del redshift sia delle proprietà degli AGN che delle galassie ospiti. Infine, lo studio dell'ambiente attorno alle sorgenti potrebbe fornire indizi sull'influenza che questo ha sull'attività di AGN e sui processi di formazione stellare.

Chapter 1

AGN: Active Galactic Nuclei

Active Galactic Nuclei (AGN) are a class of extra-galactic objects with extremely strong emission, which cannot be associated with ordinary stellar processes. Actually, around 1 and 10 % of the galaxies are known to host an Active Nucleus in their core. The nuclear emission can be orders of magnitude higher than the stellar emission of the galaxy and is originated in a very small region at the center of the galaxy, hence the name "active nuclei". This emission ranges from the radio to X-ray wavelength, and sometimes up to the γ-ray band. According to models, the driving mechanism of this enormous emission is the "combination" of a Supermassive Black Hole (SMBH), at the center of the galaxy, and the infalling gas.

In this chapter we will introduce the AGN, their structure (section 1.1), classification (section 1.2) and emission mechanisms (section 1.3). In section 1.4 we will discuss the obscured AGN population and their importance in astrophysics.

1.1 AGN structure

At present, the general structure of AGN is thought to be known; however the exact details are still matter of discussion.

At the very center of an AGN lies a **SMBH**, swirling around it an **accretion disk**. Around the disk, and maybe connected to it, there is an **obscuring torus**, mainly composed of gas and dust. Around the central SMBH and photo-ionized by the central engine, two regions can be identified and classified on the bases of the type of emission lines they produce : the **Broad Line Region** and the **Narrow Line Region**. The former is the innermost and can be hidden by the obscuring torus along some lines of sight, the latter is outer to the torus, and always visible. Some AGN have also **jets** of relativistic charged particles, originated near the nucleus and extending almost perpendicular to the disk up to Mpc distance. The jet-medium interaction can form extended radio emission region, known as **lobes**. The densest and most luminous regions

of the lobes are called **hot spots**.

Super Massive Black Hole

The SMBH is responsible for the huge emission of the AGN, via the liberation of a fraction of the energy of the infalling matter. Its mass is in the range $M_{SMBH} \sim 10^{6-10} M_\odot$ (Padovani et al. 2017). There are several ways to obtain an estimate of the SMBH mass: a first distinction is between *direct* and *indirect* methods.

- Direct measurements are those where the mass is derived from the dynamics of stars or gas accelerated by the black hole itself. Direct methods include stellar and gas dynamical modeling and reverberation mapping.

- Indirect methods are those where the black hole mass is inferred from observables that are correlated with the black hole mass. This includes masses based on correlations between black hole masses and host-galaxy properties, such as the velocity dispersion of bulge stars (Ferrarese et al. 2000), or the bulge luminosity (Kormendy et al. 1995), and masses based on AGN scaling relationships (Kaspi et al. 2000).

The most accurate and reliable mass measurements are based on studying the motions of individual sources that are accelerated by the gravity of the black hole. For example observations of the proper motions and radial velocities of individual stars near Sgr A* (Genzel et al. 2010) or of individual mega-maser sources in M106 (Herrnstein et al. 2005). However, these direct methods need resolved sources with measured velocities, hence, can be used only for few nearby SMBH. Another direct method, id the '*Reverberation Mapping*', relies on measuring the delay between the core (continuum emission) and BLR line-emission variability to assert the BLR distance from the core. The SMBH mass can be calculated as:

$$M_{SMBH} = f\left(\frac{\Delta V^2 R}{G}\right) \tag{1.1}$$

where ΔV is the line width and $R_{BLR} = c\tau$, where τ is the reverberation delay. The effects of everything unknown — the BLR geometry, kinematics, and inclination — are then included into the dimensionless factor f, which will be different for each AGN, but is expected to be of order unity (Padovani et al. 2017). The greatest problem in using *reverberation mapping* is that it relies on an unpredictable variability.

However, using *Reverberation Mapping*, a scaling relation between the distance of the BLR (from the core) and its luminosity has been found $R_{textBLR} \propto L_{BLR}^\alpha$ (Kaspi et al. 2000), with $\alpha = 0.67 \pm 0.05$ for the optical continuum and the broad Hβ luminosity (Kaspi et al. 2005). Again this allows us to estimate the SMBH mass from equation 1.1. Despite the higher uncertainties, linked to the dispersion of the scaling relation, this indirect method relies only on the measure of the luminosity and profile of the BLR lines.

We already mentioned that the energy emitted from the AGN comes from the liberation of potential energy of the infalling matter. Considering a particle of mass m falling in from infinity, we can write

$$E = \frac{1}{2}mv^2 = \frac{GMm}{R} \tag{1.2}$$

where M is the SMBH mass and R is the innermost stable orbit. If the rate at which mass is accreted onto the BH is $\frac{dm}{dt} = \dot{M}$, the luminosity of the AGN becomes

$$L = \frac{1}{2}\dot{M}v^2 = \frac{GM\dot{M}}{R} \tag{1.3}$$

If we call η the **efficiency** of the accretion process, i.e. the fraction of the incoming energy emitted by the AGN, $\eta = \frac{L}{\dot{M}c^2}$, we find that

$$\eta = \frac{G\dot{M}}{R} \tag{1.4}$$

Typically, for AGN a value of $\eta \approx 0.1$ is assumed. We can compare it with the efficiency of H fusion processed, typical of star cores, which results $\eta \approx 0.007$.

Accretion disk

The infalling matter is thought to form a rotating accretion disk around the SMBH. The **Innermost Stable Circular Orbit** (**ISCO**) "delimits" the inner radius of the disk and it is strictly correlated with the spin of both the SMBH and the disk. One of the first and most utilized disk model is the **Shakura & Sunyaev** (S&S) model (Shakura et al. 1973), with a geometrically thin and optically thick disk. The disk temperature is around $T \approx 10^{5-6}$ K, and it decreases with the distance from the SMBH. This disk emits via thermal Black Body (BB) mechanism, mainly in the optical and UV band. Another popular model is the **Advection Dominated Accretion Flow** (ADAF)(Ichimaru 1977), characterized by a geometrically thick but optically thin disk.

S&S and ADAF disks are respectively characterized by high and low accretion efficiency. The first seems to well reproduce Seyfert and QSO emission, while the latter should be associated with LLAGN and LINER (see section 1.2).

In case of a S&S disk, the viscosity and the differential rotation of each annular region of the disk slow the gas in the inner orbit, allowing it to fall into the SMBH.

Hot Corona

The hot corona is a low density region of gas over the disk, although its exact position and form depend heavily on the model. Recent X-ray reverberation studies (De Marco et al. 2013, Reis et al. 2013) suggest that the size of the hot corona producing the X-rays is

in the range $3 - 20\,r_g$, while dynamical microlensing on lensed quasars, restricted the hot corona dimension to a radius $< 30\,r_g$ (Chartas et al. 2016), where r_g is the gravitational radius defined as $r_g = \frac{GM_{BH}}{c^2}$.

The Hot Corona has a temperature around T$\approx 10^{8-9}$ K. Due to the fact that the electrons in this region are so energetic, the disk BB photons are up-scattered several times when they reach the Hot Corona, leading to a power law spectrum, that form the main feature of X-ray spectra. This power-law spectrum has an exponential cut-off between several tens and few hundreds keV, due to the fact that the photons' energies are similar to electrons' one and cannot be further up-scattered. The cut-off energy depends on the electron temperature and the optical depth of the corona (Lanzuisi et al. 2019).

Recent results from the Swift-BAT sample (Ricci et al. 2018) show that the average cut-off energy of the sample anti-correlates with the Eddington ratio.

Broad Line Region

At a distance of about 0.1-1 pc from the central BH there is a region where dense clouds lie (Mathews et al. 1985), which are are excited by the central engine. These clouds have temperatures around T$\approx 10^4$ K and densities $n \approx 10^{10-11}$ cm^{-3}, high enough to suppress several forbidden lines. The motion of these clouds around the SMBH, at velocity around 10^{3-4} km/s, leads to the broadening of the line profiles, from which this region takes its name, that can be used to estimate the velocity of these clouds, hence the SMBH mass.

The BLR is inside the torus so this region can be seen only at high equatorial angles (i.e. close to face-on position), where the line of sight does not intercept the torus. This explains why an obscured AGN does not show broad lines. However, sometimes, also obscured AGN can show broad lines in polarized light (Antonucci et al. 1985). This is explained thanks to the circumpolar gas that scatter and polarize, part of the BLR emission.

Obscuring torus

The obscuring torus is composed primarily of gas and dust and spans from ≈ 1 to 100 pc from the central BH. The exact nature and form of the torus is still matter of debate, but we can generally view it as composed of dense clouds, with column density $N_H \approx 10^{22-24}$ cm^{-2}. Due to high column density, few optical and UV photons can reach us when the line of sight intercepts them. For higher column density even the X-ray emission can be heavily dimmed.

This obscuration along certain lines of sight is the basic concept under the **unified model**, where most of the differences see among AGN types are ascribed to the orientation of the torus along our line of sight (see section 1.2).

The most used torus models are the *smooth torus* and the *clumpy torus*. The former describes the torus as composed by a smooth distribution of dust and gas (i.e. Pier

et al. 1992, Stenholm 1994, Efstathiou et al. 1995, Manske et al. 1998, Fritz et al. 2006) and where the temperature is a function of the distance from the nucleus; the latter describes the torus as composed by a multitude of small clouds, where the temperatures and density are not directly associated to the distance (e.g. Nenkova et al. 2002, Mor et al. 2009). Moreover, in clumpy models there is not a well defined angle that separates type 1 from type 2 AGN. It is possible to have low equatorial angles with direct view into the core and higher angles obscured by several clouds. The amount of obscuration is, then, a matter of the number of clouds intercepted (Alonso-Herrero et al. 2011), rather than only dependent on the viewing angle. Clumpy models are a more likely representation of the real dust distribution as a smooth dust distribution would result in collisions that would raise the temperature to levels too high for the dust to survive (see e.g. Krolik et al. 1988). On the other hand, smooth models were the first to be developed, being computationally simpler and, in many aspects, a good approximation when calculating the IR **Spectral Energy Distribution** (**SED**) of AGN. The success of both classes of models in fitting different parts of the observed AGN SEDs keeps the issue of the dust distribution in AGN open, as no conclusions can be drawn from the simple comparison between observed and model SED (Feltre et al. 2012).

Narrow Line Region

The Narrow Line Region is composed of clouds with low density $n \approx 10^{3-4}$ cm^{-3}, it's located between ≈ 100 pc and 1 kpc (Capetti et al. 1996) from the central BH and has temperatures around T$\approx 10^{3-4}$ K. Being less dense means that forbidden lines can be emitted by these clouds. Moreover, being these regions external to the torus, the emission lines are never obscured by it, regardless of the line of sight. Due to the fact that the clouds are so far away from the central BH, they have slower speed (a few hundreds-1000 km/s) and the emission line profiles are narrow, hence the name of the region. As the NLR should be photoionized by the nuclear emission, it should have a (bi)conical morphology, due to the light cones defined by the torus. High-resolution, narrow band imaging (or integral field spectroscopy) has indeed revealed such ionization cones on scales ranging from a few tens pc up to several hundreds pc, in many nearby AGN (Pogge 1988, Evans et al. 1991, Wilson et al. 1994, Barbosa et al. 2009).

Jets and Lobes

A fraction ($\approx 15\%$, but increasing with bolometric luminosity, Urry et al. 1995) of AGN are characterized by significant radio emission and defined as *Radio Loud* AGN (see section 1.2). Around 10% of them has extended radio emission. This comes from two types of structure: jets and lobes. The jets are composed of plasma of relativistic particles. These charged particles are accelerated up to ultra-relativistic speed by the magnetic field in the innermost regions of the AGN and "expelled" in polar directions,

forming two structures know are jets. The jets emit in the radio band via synchrotron emission and up to the γ-band (in case of Doppler boosting) via Inverse Compton.

The jets can remain ultra-relativistic up to kpc scales, then became very luminous and have strong interaction with the medium, in case of FRI sources, or up to Mpc scales, in case of FRII sources (see next section for the definition of FRI and FRII radio sources). The latter have less luminous and narrower jets, due to the fact that the jets have fewer interactions with the medium. In case of FRII, the jet-medium interaction produces large radio-lobes and hot-spots. These are regions where the jets collide and interact with the external medium, producing shocks and strong synchrotron emission.

1.2 AGN classification

There are various AGN classifications, based mainly on the band in which they are observed and the resulting properties. The first AGN spectrum dates to 1908, although E. A. Fath classified it as a nebula with strong emission lines.

The first scientist who classified AGN as a different type of object from other known sources was C. Seyfert in 1943, who studied and classified objects with strong emission lines, the broadening of which suggested of velocity up to thousands of km/s. These objects are now called **Seyfert** galaxies.

In the '50s, the first radio survey identified a peculiar class of object, with optical properties similar to normal galaxies but being point-like and having unknown emission lines. Years later these lines were identified as highly redshifted lines. This meant that these objects, known as **QUASAR** (QUASi-stellAR radio sources), were in fact far away galaxies, with before-unknown high luminosity.

From the '60s new types of AGN were discovered and this lead to many different classifications, based on the observed properties.

Radio classification

AGN are classified as **Radio Loud** (**RL**) or **Radio Quiet** (**RQ**), depending on their optical-to-radio flux ratio R_{r-o} (Kellermann 1989). The optical flux is measured at 4400 Å and the radio flux density at 5 GHz (both rest-frame). AGN with $R_{r-o} > 10$ are defined as RL, while the others as RQ. This classification goes all the way back to Sandage (1965), who realized, soon after the discovery of the first quasar, 3C 273, a very strong radio source, that there were many similar sources in the sky, which were however undetected by the radio telescopes of the time. It was later understood that these quasars were only "radio-faint", but the name stuck (Padovani et al. 2017).

Other flux, or luminosity, ratios can also be used to separate these two classes. For example, the ratio between radio and X-ray luminosity, defined as $R_X = \log \frac{\nu L_\nu (5\text{GHz})}{L_X}$. RL object has $R_X \leq -4.5$ (Terashima 2005).

The most used radio AGN classes are:

Radio Loud

- **Radio galaxies:** usually are associated to giant elliptical galaxies, the most powerful are in cluster cores. Radiogalaxies are dominated by radio non thermal emission. Their bolometric luminosity can reach 10^{47} erg/s. Radio-galaxies can be further divided in **FRI** and **FRII**, based on their radio morphology and radio power (Fanaroff et al. 1974). FRI have $P_{1.4\mathrm{GHz}} < 10^{24}$ W/Hz and their emission is dominated by the jets. As we already mentioned, these jets are relativistic only up to kpc scales and heavily influenced by their interaction with the medium. FRII have $P_{1.4\mathrm{GHz}} < 10^{24}$ W/Hz and their emission is dominated by the lobes. Their jets remain relativistic up to Mpc scales.

- **Radio Loud Quasars:** Very luminous, they can reach $L_{\mathrm{bol}} \approx 10^{48}$ erg/s and their optical counterparts appear as point-like sources with strong emission lines.

- **BL Lac:** Similar to Quasars but without emission lines. Their optical spectra are dominated by a flat continuum. BL Lac are highly variable sources. Together with **Optical Violent Variable** (**OVV**) and **Flat Spectrum Radio Quasar** (**FSRQ**), they are called **Blazar**.

Radio Quiet

- **Radio Quiet Quasars:** Similar to Radio Loud Quasar but without strong radio emission.

- **Seyfert:** Usually found in spiral galaxies. They have a broad band emission but their radio emission is usually faint (10^{20-23} W/Hz). Due to their relatively low luminosity it is usually possible to observe the host galaxy. They are further divided in Seyfert I or Seyfert II, based on the presence of both broad and narrow lines (Seyfert I) or only narrow lines (Seyfert II).

- **LINER:** Low Luminosity Narrow Emission-line Region are very low luminosity ($L_{\mathrm{bolo}} \approx 10^{40-42}$ erg/s) objects. Found in spiral galaxies, they are characterized by the presence of low-ionization narrow emission lines. Their exact nature is still a matter of debate, in particular their emission could be explained with low luminosity AGN or Starburst events and SN explosions.

Optical classification

The AGN optical classification is based on the presence and properties of optical emission lines. AGN with both broad emission lines (up to $\Delta v_{\mathrm{FWHM}} \approx 10^4$ km/s) and narrow

	Type 2	Type 1
Radio Quiet	Seyfert 2	Seyfert 1
	LINER	RQ Quasar
Radio Loud	NLRG(FR I + FR II)	BLRG
		Radioquasar (SSRQ + FSRQ)
		Blazar (BL Lac + OVV)

Table 1.1: A schematic view of AGN optical and radio classification.

emission lines (up to $\Delta v_{\mathrm{FWHM}} \approx 10^3$ km/s) are classified as **type 1** or **unobscured**, whereas AGN with only narrow emission lines are classified as **type 2** or **obscured**. Usually, type 1 AGN are more variable and luminous than type 2 AGN.

In Table 1.1 a compact, but not exhaustive, radio and optical AGN classification is shown.

Unified model

The spectral analysis of the AGN shows that some sub-classes share common characteristic but have also different features. Over the years numerous attempts were made to create a unified model of AGN, explaining the large number of AGN sub-classes.

In 1978 Osterbrock proposed to unify Seyfert I and II: the differences between these two types of object would be explained thanks to an obscuring torus of gas and dust that hides the central region and the BLR (Osterbrock 1978). This torus absorbs the optical, UV and X-ray emission, via photoelectric effect, and it emits termically in IR and mid-IR bands. If the line of sight intercepts the torus, the inner region and the broad lines are not visible and the source is identified as a Seyfert 2. If the AGN is seen in polar direction, the line of sight does not intercept the torus and we can see all the central region emission and the broad lines, and the source is classified as a Seyfert 1.

Another steps toward the unification was taken in the same year by Blandford and Rees (1978). They suggest that Blazar and Quasar could be radio-galaxies observed in at low polar angles, hence with the jet pointed along our direction. In this case, the effect of Doppler boosting, as the source of the synchrotron (and IC) emission (the electrons) are traveling at ultra-relativistic speed toward us, would enhance by several orders of magnitude both the observed flux and the variability. In particular, the observed flux would be

$$F_{\mathrm{obs}} \propto F_0 \cdot D^4 \tag{1.5}$$

where D

$$D = \frac{1}{\gamma(1 - \beta \cos \theta)} \tag{1.6}$$

is the Doppler Factor, γ the Lorentz factor $\gamma = 1/\sqrt{1 - \beta^2}$, $\beta = v_{e^-}/c$ and θ is the angle between the jet and the line of sight.

These and other works led to the **Unified model** (Antonucci 1993; Urry et al. 1995). In the unified model (Figure 1.1) the general AGN structure is the one described in section 1.2. The major observed differences between AGN spectra are related to the line of sight. At the zero order, at least in the local universe, the unified model is almost capable of explaining all the observable properties (and differences) of AGN classes.
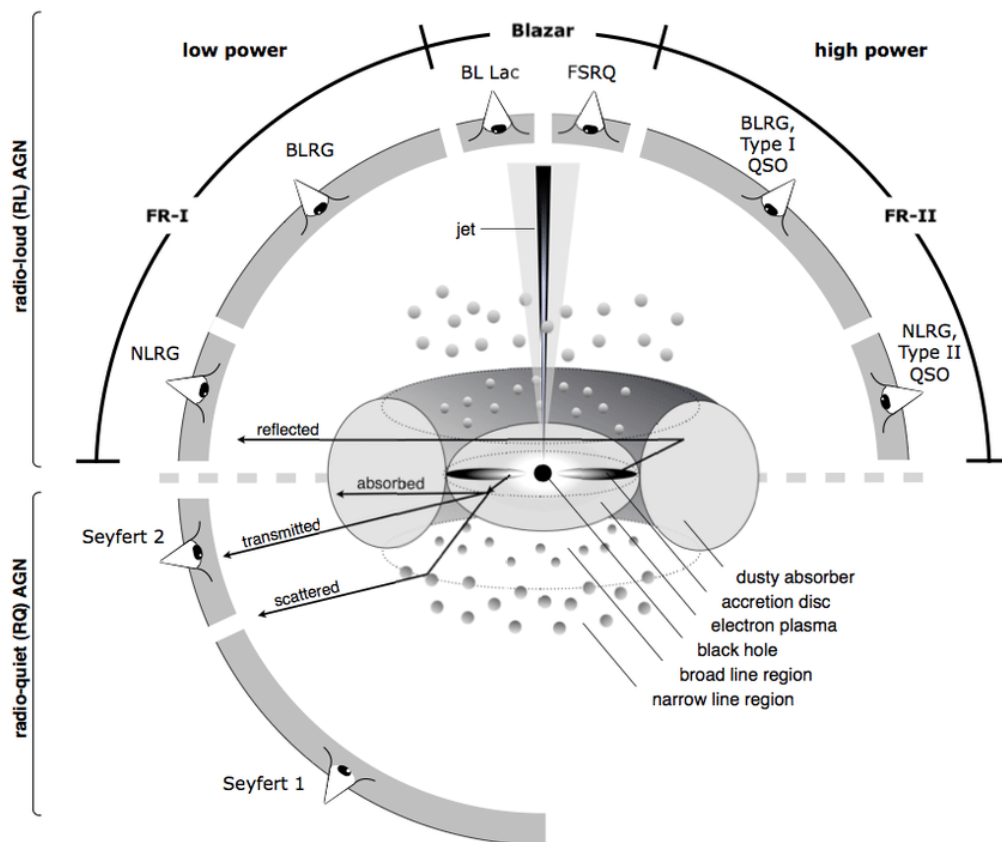

Figure 1.1: The AGN unified model (Beckmann and Shrader 2012).

1.3   AGN broad-band emission

AGN emission can extend from the Radio to the γ-rays. The typical AGN SED of a RQ AGN is shown in Figure 1.2.

Every band has its own features, that reflect different emission mechanisms. With few exceptions, the optical and UV emission-line spectra and the infrared to soft X-ray

continuum of most RL and RQ AGN are very similar (Sanders et al. 1989) and so must be produced in a similar way. The characteristics of radio-loudness itself may be related in some way to host galaxy type or to black hole spin (Blandford 1990), which might enable the formation of powerful relativistic jets (Urry et al. 1995).

Like line emission, broad band features depend heavily on the viewing angle. In type 1 AGN the typical three-bump SED is dominated by the UV/optical emission of the disk (known as Big Blue Bump), while on type 2 almost all the UV/optical emission is hidden by the torus. In case of the most absorbed AGN, soft and part of hard X-ray emission are also absorbed, leading to quite different spectral shape. In Figure 1.3 we can see a model of AGN FIR-to-UV emission for different viewing angles.
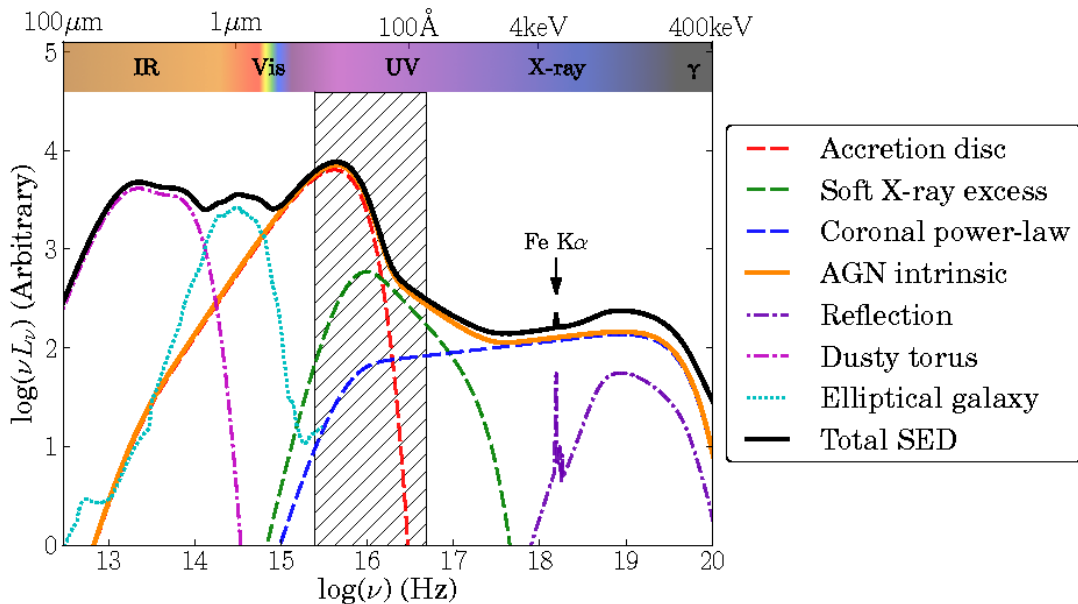

Figure 1.2: Simplified schematic diagram of an AGN SED (Collinson et al. 2017).

1.3.1 X-ray emission

The AGN X-ray emission comes from the inner region of the AGN and gives information about the SMBH, the hot corona and innermost region of the accretion disk. The X-ray emission comes from different sources and processes and can be considered a defining characteristic of the class of AGN. In addition, the X-ray flux shows a very fast variability (McHardy 1990) which indicates that it originates in a small region very close to the central object. The intrinsic X-ray emission from AGN is due to processes related to the accretion disk and hot corona (see Mushotzky et al. 1993, Done 2010), however, in
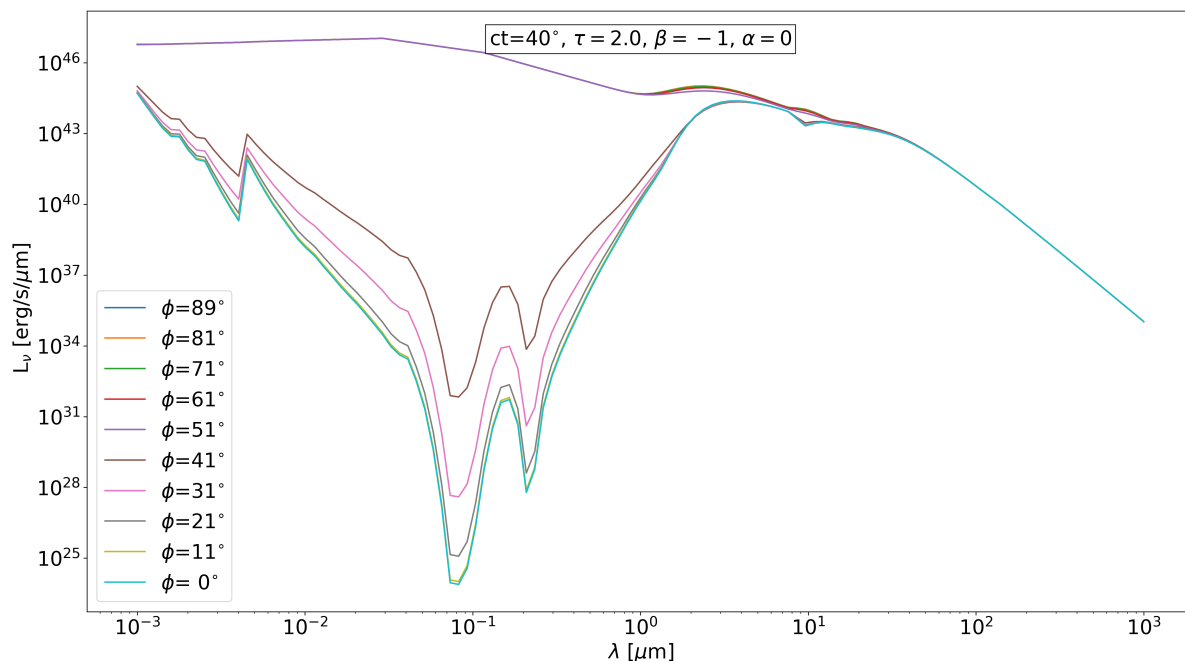
Figure 1.3: Models of AGN SED for different equatorial viewing angle ϕ (left-bottom part of the figure). In this model AGN with $\phi < 50°$ are edge-on, $\phi > 50°$ are face-on. Emission obtained from Fritz et al. 2006 and Feltre et al. 2012 models.

jetted AGN the jet can make a major contribution in the X-ray band as well (Padovani et al. 2017).

The primary process is thought to be inverse Compton scattering of the accretion-disk photons to X-ray energies via the hot corona. The X-ray emission is then modified due to the interaction with matter in the nuclear region (e.g. reflection, scattering, and photo-electric absorption of photons from the accretion disk and/or the obscuring AGN torus). The relative strength of these components can vary quite significantly from source to source, mostly due to differences in the geometry and inclination angle of the torus to the line of sight, leading to a broad range of X-ray spectral shapes.

Hot corona power law

This is the dashed blue line in Figure 1.2. The hot corona has a temperature around $T \approx 10^{8-9}$ K, so its electrons are very energetic. The optical and UV photons emitted by the disk, which has temperature around $T \approx 10^{5-6}$ K, turn out to be less energetic than the hot corona electrons and are up-scattered via IC. These photons go trough several up-scatters until their energy is similar to the electrons' energy. These scattering

produce a power law continuum with a thermal exponential cut-off.

The power law component is usually fitted with a spectral index $\Gamma = 1.8$, in the $F_E \propto E^{-\Gamma}$ notation. $\Gamma = \alpha + 1$, where $\alpha = \frac{-\ln\tau}{\ln A}$ is the spectral index, τ is the opacity, $A = e^y$ is the mean energy gained by the photons for each scattering and $y = \frac{4kT}{m_e c^2}$ is the comptonization parameter. However, the presence of gas can absorb part of the soft X-ray emission and, for highly obscured object, also the hard X-ray emission, leading to flatter slopes.

Reflection Bump and Iron Kα line

The hot corona emits isotropically, so a part of its emission should be directed toward the accretion disk. This leads to two different processes.

A part of this emission is reflected by the disk and we see an excess in hard X-ray spectra with respect to the pure power law from the hot corona. This excess is known as Reflection Bump (dark purple line in Figure 1.2).

A part of the hot corona emission is absorbed. These high-energy photons can liberate strong bounded inner electrons from high Z atoms. The most important transition is that involving the Iron Kα case. Photons of energy above E$\approx$ 7.1 keV can free a K shell electron, producing a "hole" in the innermost shell. This hole is then filled by an electron of an outer shell. The excess energy can be expelled in two different ways: by unbounding another electron from the outermost shell of the atom (this is known as *Auger effect*), or by the emission of a fluorescence Kα, or more rarely Kβ, photon. The former case is responsible for the 6.4 keV Iron line. This line is very important: on the one hand it should be very luminous and easily to identify, on the other hand it is generated at a few gravitational radii from the SMBH and should show gravitational redshift effects.

Soft excess

In the vast majority of AGN there is an excess at E $<$ 1 keV with respect to the hot corona power law (green dotted line in Figure 1.2), the nature of which is not yet well understood. Early models predict that it could be due to BB emission from the innermost regions of the accretion disk. However, even the ISCO should not reach sufficient temperatures in the case of SMBH. To the present days, models predict that it can be associated with atomic processes of partially ionized material (Done et al. 2007). Two different geometries of partially ionized material can explain the soft excess: one where the material is optically thick and out of the line of sight, seen via reflection, e.g. from an accretion disc (Crummy et al. 2006). Alternatively, the material can be optically thin and along the line of sight, seen in absorption, e.g. a wind above the disc (Gierliński et al. 2004).

Warm absorber

In case of high column density ($N_H > 10^{21}$ cm^{-2}) photons between $1 \le E \le 2$ keV can be absorbed. The responsible for this absorption is gas with T$\approx 10^{4-5}$ K, in region smaller than pc scale (e.g. Kaastra et al. 2000). In some cases the absorption lines are blue-shifted and it is believed that this absorber can origin from out-flowing gas maybe connected to AGN winds (Tombesi et al. 2013). The wind-absorber scenario could explain also the rare **Ultra Fast Outflow** (**UFO**), high-ionization absorption lines with velocities (from Doppler shift) typically of 0.1c (Tombesi et al. 2010). These UFOs could be related to AGN winds from the central region, where there are high temperatures, so the matter is highly ionized, and high energies, to accelerate up to quasi-relativistic speed. It has been argued that the absorbers, sometimes considered of different type, could actually be unified in a single, large-scale stratified outflow observed at different locations along the line of sight. The UFOs are likely launched from the inner accretion disc and the Warm absorber at larger distances, such as the outer disc and/or torus (Tombesi et al. 2013).

1.3.2 Optical emission

The main feature of the AGN optical emission is the **Big Blue Bump** (red dotted line in Figure 1.2), a high-luminosity continuum between 300 Å and 3000 Å. It is due to the BB emission of the accretion disk. In particular, the accretion disk has a range of temperatures, decreasing going outward, and the superposition of the various BB, each with its own temperature, creates a power law emission with $F_\nu \propto \nu^3$.

In the optical band there are also emission lines from the BLR (for type 1 AGN) and the NLR (for both type 1 and 2). As already reported in section 1.1, BLR lines have broad line profiles; NLR lines have narrower profile and, thanks to the lower density of the region, also included forbidden lines. The narrow lines are visible even for the most obscured AGN, thanks to the NLR being uncovered from the torus. Moreover, it is the inner region of the AGN that illuminates the NLR, hence exciting atoms and allowing the production of these lines. Therefore the NLR line (e.g. [OIII], [NeV]) flux can be used to estimate the intrinsic power of the AGN (Schmidt et al. 1998,Gilli et al. 2010, Vignali et al. 2010).

1.3.3 IR emission

The IR emission of AGN can be split into two different components: one from the dusty torus (light purple line in Figure 1.2) of the AGN and one from the dust of the host galaxy (light blue). The obscuring torus is heated as it absorbs the optical and UV photons. The dust grains then re-emit in the mid-IR. The majority of this thermal emission is between 10 and 20 μm, linked to dust temperature between 1000 and 2000

K, at higher temperature the dust grains sublimate. As for NLR lines, the energy source of this emission are photons from the AGN inner region. As such the mid-IR emission is, again, a proxy of the intrinsic nuclear emission (Gandhi et al. 2009).

However, in the mid-IR there is also a thermal emission from the host galaxy dust. This dust is linked to star-formation (SF) processes and is heated by UV emission from O and B stars. Having two overlapping components in mid-IR emission means that we need to separate them in order to unveil the AGN emission, but also that, if we succeed in it, we also get information about the host galaxy.

1.3.4 Radio emission

Except for SF-related processes, the radio emission in AGN is non-thermal and mainly produced by synchrotron. The electrons are accelerated up to ultra-relativistic speed by the magnetic field of the central region. With an ultra-relativistic electron of mass m_e and Lorentz factor γ into a magnetic field B, the magnetic field accelerates the electron, producing the emission of a photon of frequency $\nu \propto BE^2$, where $E = \gamma m_e c^2$. If we have a population of electrons with a power law energy distribution N(E)

$$N(E)dE \propto E^{-\delta}dE \tag{1.7}$$

we obtain a spectra with $F_\nu \propto \nu^{-\alpha}$, where $\alpha = (\delta - 1)/2$ and typical value around $\alpha \approx 0.8$. In dense region, the synchrotron photons can be absorbed by the same electrons that generated them. We have then a self-absorbed spectra with slopes $\nu^{5/2}$.

In RL AGN the radio emission is mainly located in jets, lobes and hotspot (section 1.1) and the nuclear emission is not usually dominant.

1.4 Importance of obscured AGN

With the term "obscured AGN" we refer to type 2 AGN, hence AGN seen at low inclinations with the majority of nuclear emission hidden by the torus. Despite the difficulty in the identification and study of type 2 AGN, they play a fundamental role in the context of the BH-galaxy co-evolution scenario and the missing X-ray background sources.

1.4.1 AGN-galaxy co-evolution paradigm

The presence of scaling relations between the mass of SMBH and the mass (or luminosity) of the spheroid (Kormendy et al. 1995) or the velocity dispersion of the spheroid (Ferrarese et al. 2000, Gebhardt et al. 2000) suggested a tight link between star-formation activity in the spheroidal components of galaxies and SMBH growth. Such link is confirmed by the striking similarity of the evolution of the SMBH accretion rate and of the star formation rate (or of the AGN) densities, especially at substantial redshifts where

the star formation mostly occurs in the spheroidal components (Shankar et al. 2009, Fiore et al. 2017). These relations lead to the formulation of the **BH-galaxy co-evolution paradigm** (e.g. Sanders et al. 1988, Di Matteo et al. 2005, Hopkins et al. 2006). In this scenario the growth phases of both SMBH and galaxy stellar mass are closely connected. The key to this link is the AGN activity.
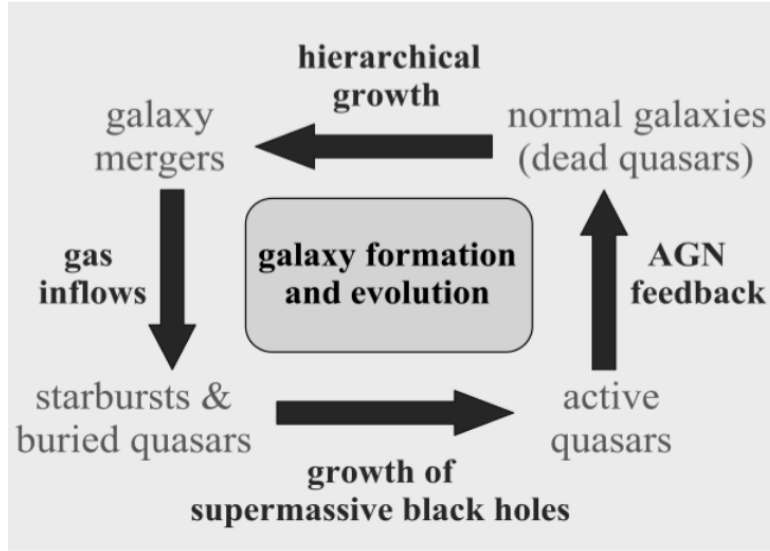

Figure 1.4: Schematic representation of a "cosmic cycle" for galaxy formation and evolution regulated by black hole growth in mergers (Hopkins et al. 2006).

As we can see from Figure 1.4, the BH and galaxy growth cycle in the AGN-galaxy co-evolution scenario can be split in several phases:

1. **Galaxy merger:** A **wet merger** (merger in which at least one of the galaxy has still cold gas) disrupts the gas equilibrium and triggers the SF processes. Mergers are expected to occur regularly in a hierarchical universe, particularly at high redshifts.

2. **SB and buried Quasar:** The merger driven SF rate is very high and we call these galaxies **Starburst Galaxies** (SBG). In this phase there is a large amount of cold gas and dust in the galaxy and sources of UV emission (O and B stars) capable of heating the dust. This leads to spectra with high IR emission from heated dust, hence the name **Ultra Luminous Infra-Red Galaxies** (**ULIRG**).

   The high quantity of gas which is present and the disruption of the gas equilibrium lead a part of the gas to fall into the central region and the SMBH. This has two effects: the growth of the BH and the activation of the AGN. However, due to the large quantity of gas both in the galaxy and infalling in the SMBH, the

AGN activity is not directly visible and obscured up to hard X-ray wavelength. Moreover, the AGN jets have to dig their ways out of the galaxy, again due to the large quantity of gas. Therefore, if we aim at studying this first phase of AGN and galaxy growth, we have to investigate heavily obscured **type 2 AGN**.

3. **Active Quasar:** There are two processes that concur to stop the SF and the SMBH growth. The first is the SF itself, as the gas in consumed by the SF processes. In case of low-mass galaxies, the SN explosions can also expel a large fraction of gas from the galaxy (Dekel et al. 1986). The second, and more important process, is the **AGN feedback**. The AGN activity transfers a significant amount of energy to the galaxy gas and makes it unsuitable to fuel further SF or simply blows it all out of the galaxy. Not having new cold gas available, this leads to SF quenching, but also stops the accretion of matter into the SMBH. Evidence in support to this scenario comes from observations of molecular outflows extending few kpc from the nucleus (e.g. Feruglio et al. 2010) and of ionized outflows (e.g. Nesvadba et al. 2008) and UFOs in the inner region (Tombesi et al. 2010).

   At this point the limited amount of gas still present is not sufficient to obscure the AGN and we have a short lived bright quasar phase.

4. **Normal galaxy:** Once that the AGN activity consumed all the remaining accreting gas, the AGN "dies", either becoming a Low Luminosity AGN or changing its accretion mode from a "merger driven" to a "secular smooth" accretion, using cooled ICM (Intra Cluster Medium) as fuel. What is left is an elliptical relaxed galaxy, without trace of significant cold gas and SF, and with a stellar population characterized by an intense and fast episode of SF.

   The remnant will then evolve passively and would be available as a seed to repeat the above cycle.

To study the AGN-galaxy co-evolution paradigm we need an AGN census as large and complete as possible. Here the problems come from the difficulty of both identifying and studying the heaviest obscured AGN, which should be the tracers of the first phase of the BH growth. The study of these objects could also help in shedding light upon how the AGN feedback mechanism works.

1.4.2 X-ray background

That a diffusive X-ray glow pervades the sky was first discovered by Giacconi et al. in 1962, in the first X-ray astronomy experiment. In Figure 1.5 the spectrum of the X-ray background (**XRB**) is shown. As far as today more than 90% of the XRB under 10 keV has been resolved in hundreds of millions of individual X-ray sources distributed across the entire universe. Most of them are AGN (Moretti et al. 2012). However, at
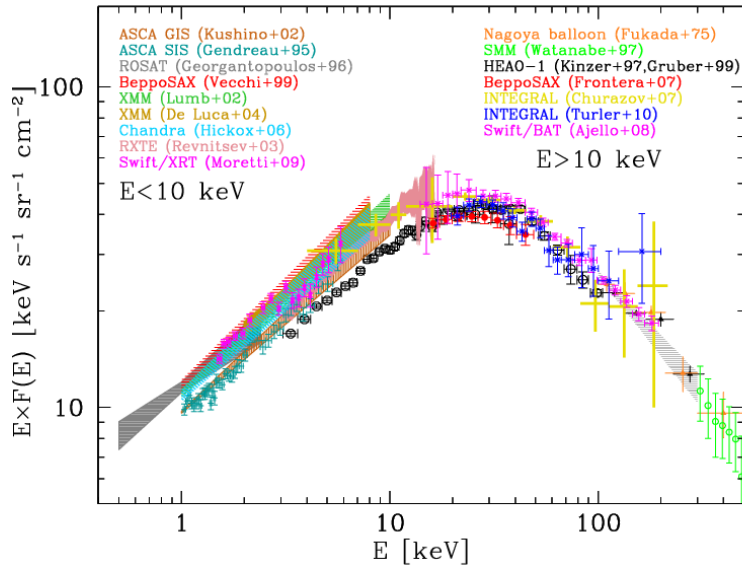
Figure 1.5: Compilation of the measurements of the cosmic X-ray background spectrum in the 0.5 - 400 keV energy range. Data points with different colors come from different combinations of missions and instruments as labeled and referenced (left labels: E < 10 keV; right labels: E > 10 keV) (Gilli 2013).

energies E $\sim$ 30 keV, where the XRB spectrum peaks, only 30%-40% of its emission has been resolved into individual sources (Harrison et al. 2016). A large portion of the XRB emission is expected to be produced by the same sources observed at lower energies, and these sources should be missing only because of the lower sensitivity of our instruments in the hard X-ray band. The very shape of the spectrum calls for a large population of **Compton Thick (CT) AGN**, hence with $N_H > 1/\sigma_T = 1.6 \cdot 10^{24}$ cm^{-2}, poorly sampled at low energies (Gilli 2013).

Since 1989, when it was firstly suggested that the hard XRB could be explained by the superposition of AGN spectra with different absorption degrees (Setti et al. 1989), many XRB synthesis models have been proposed. According to these models, 10% to 40% of the XRB emission above 30 keV is produced by CT AGN. Moreover, as we see in Figure 1.6, the majority of the missing XRB should be produced by CT sources between $z \sim 0.5$ and $z \sim 1.2$ (Gilli et al. 2007), so a direct study of these sources is highly desirable.

1.5 Goals of this project

My work is focused on the the study of type 2 AGN and their host galaxies in the $0.65 < z < 1.20$ redshift interval, selected by the mean of the [NeV] emission line in the
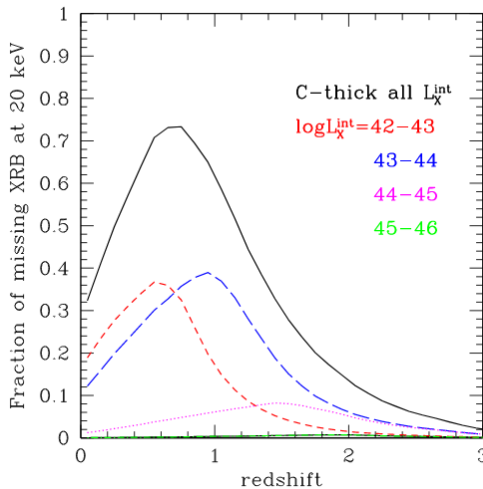
Figure 1.6: Fraction of the missing XRB emission at 20 keV produced by CT AGN at different redshifts in the Gilli et al. 2007 model. The emission from the whole CT population (black line) is split into four bins of intrinsic 2-10 keV luminosity L_{int}^x(color curves): most of the "missing" XRB is expected to be produced by objects with $L_{int}^x < 10^{44}$ erg/s and $z < 1$ (Gilli 2013).

COSMOS field. It consists of two parts: the analysis of their X-ray spectral properties and the characterization of AGN and host galaxy via SED-fitting of optical-to-far-IR data.

We used a sample of 94 type 2 AGN, selected from the zCOSMOS 20K Bright catalog (Lilly et al. 2007 and 2009). The selection was made by detection of the high-ionization [NeV]3426Å line and including the objects with narrow lines in their optical spectra (Mignoli et al. 2013). As reported in section 1.3.2, the [NeV] flux can be used to obtain the source intrinsic luminosity. Due to the fact that zCOSMOS data came from VIMOS observations, covering the $3600 < \lambda < 10000$ Å wavelength range, a selection based on [NeV] lines limited our analysis to AGN in the $0.65 < z < 1.20$ redshift range. This is important because, as reported in section 1.4.2, XRB synthesis models predict that the density of XRB missing sources with luminosity between $10^{43} - 10^{44}$ erg/s should peak at $z \approx 1$. To summarize, the use of [Ne V] selection method allowed us to properly select objects that should be the very XRB missing sources. In addition, as reported in section 1.4.1, we can target these highly obscured AGN to study the first phases of the AGN-galaxy co-evolution cycle. Due to the high obscuration of these sources, we cannot rely on single energy band observations. In fact, even high-energy wavelength, like X-rays, can be heavily dimmed by column densities higher than 10^{23} cm^{-2}. On the other hand, if we try to study these sources using only proxies, like the IR torus emission, there are other processes emitting at the same wavelengths and we need a way

to separate their emission from that of the AGN. To overcome these difficulties, we used a multi-wavelength approach, exploiting the broad energy range of COSMOS field data.

In particular, since one of the goals is searching for heavily obscured and CT AGN, we carried out X-ray spectral analysis to characterize AGN properties, like luminosity, spectral index, obscuration and intrinsic luminosity and performed statistical analysis of them. To further characterize the source obscuration, we used the X/[NeV] ratio (Gilli et al. 2010), where [NeV] is the observed [NeV] flux and X is the 2-10 keV rest frame (not corrected for the obscuration) observed flux. For X-ray undetected sources we calculated the flux limit and used it to obtain the X/[NeV] ratio, in order to have a limit on the source obscuration. Previous works investigated the X-ray properties of the same [NeV]-selected type 2 AGN sample using 2007 C-COSMOS data (Vignali et al. 2014). Exploiting the new 2014 COSMOS Legacy data, that extended the X-ray coverage to the whole COSMOS field and provided uniform sensibility all over it, we aimed at obtaining stricter constraints than previous works on the derived parameters, like column density and intrinsic X-ray luminosity. A by-product of this work is the study of source variability, exploiting the fact that X-ray observations in COSMOS field extended through several years.

In the AGN-galaxy co-evolution scenario, the phase of obscured AGN accretion is related to intense star formation events in the host galaxy. Given that our sample was composed of obscured AGN, we would like to investigate star formation rates and host properties. To do this, we used optical and IR data from COSMOS2015 catalog (Laigle et al. 2016) and the SED-fitting algorithm *sed3fit* (Berta et al. 2013, da Cunha et al. 2008), to separate the galaxy emission from that of the AGN. The SED-fitting analysis gave us both host properties, like SFR, stellar mass and amount of gas in the galaxy, and AGN properties, like angle of sight, torus optical depth and bolometric luminosity. We aim at verifying the goodness of our results using various correlations (e.g. SFR-L_{FIR}^{SF}, $L_{2-10keV}$-L_{bolo}^{AGN}, $L_{12\mu m}^{AGN}$-$L_{2-10keV}^{int}$) and compared the SED-fitting results with those from the X-ray spectral analysis. This with the double goal of checking the goodness of our results and confirming the correlations.

As in Vignali et al. 2014, we may expect that the most obscured AGN would be without X-ray detection, being the X-ray emission at E < 10 keV completely absorbed. For these sources we will derive limit X-ray luminosities and compare them with intrinsic luminosities found via SED-fitting. We expected intrinsic luminosities much higher than X-ray luminosity upper limits, confirming the CT nature of these AGN.

On a longer term, we would like to compare the SFR of our sample with SFR of galaxies without significant AGN activity, to investigate the AGN feedback influence on SF processes, upon which the AGN-galaxy co-evolution paradigm is based.

Chapter 2

Instrument and COSMOS field

As already mentioned in Chapter 1, the X-ray emission allows us to study the innermost region of the AGN and its physical properties. However, in case of CT AGN even these short wavelengths can be obscured. As we need type 2 AGN samples as complete as possible and aim at studying the sources with sufficient details, a **multi-wavelength** approach is needed.

In section 2.1 we give a brief introduction to telescope parameters. In our work we used X-ray data from the Chandra telescope (section 2.2) and IR and optical data from the COSMOS2015 catalogue. In section 2.3 we present the COSMOS field, the X-ray (section 2.3.2) and the IR and optical data-sets used (section 2.3.3) in our work.

2.1 Main parameters of the telescopes

We used both X-ray data, taken with the Chandra space telescope, and optical and IR data, taken with several different ground- and space-based telescopes. One of the
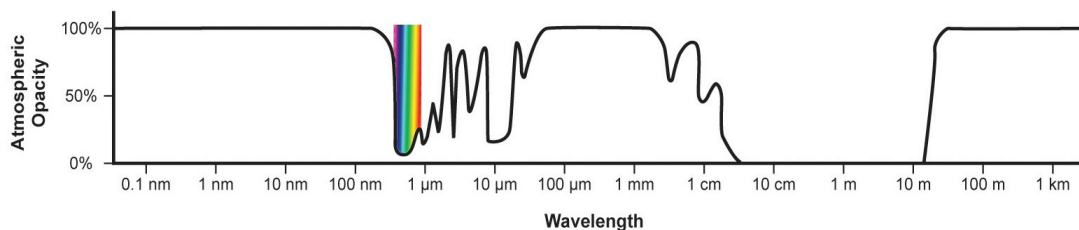

Figure 2.1: Atmospheric opacity

most important thing to consider about telescopes is the influence of the atmosphere. The atmospheric opacity (Figure 2.1) depends mainly on the wavelength considered. As all the X-ray emission is absorbed by the atmosphere before reaching ground, X-ray telescopes, as UV and IR ones, except for small wavelength windows, have to be in orbit

to be able to operate. Even when photons can reach ground, allowing us to use ground-based telescopes, the atmosphere continues to influence the image quality, via an effect called "seeing". When using data from different telescope, the different capabilities of each one have to be taken in account. There are several parameters that reflect each telescope capabilities and allow us to confront different telescopes.

- **Angular resolution:** It is the capability of distinguish sources as separated objects. It is defined as the minimum angular distance that two point-like sources can have in order to be seen as separated objects. The maximum resolution achievable for a telescope of diameter D is $\theta = 1.22\,\lambda/D$. However, ground-based telescope are affected by the seeing that lower the angular resolution.

  The **Point Spread Function** (**PSF**) describes how the telescope optics spread the light of a point-like source over the detector. The angular resolution is strictly linked to the PSF. As the PSF becomes narrower, the angular resolution lowers and the imaging capability improves.

- **Spectral resolution:** Similar to the angular resolution, but related to spectrography, it is the capability to distinguish two close spectral features. In an ideal instrument the spectral resolution is R $= \frac{\Delta E}{E}$, where E is the line energy and ΔE is the line width. If we assume Poisson regime, we have R$= 2.35 F/\sqrt{N}$, where F is the *Fano factor* and N is the number of charge carrier associated to the line.

- **Time resolution:** It is the capability of distinguish two temporally close events as separated. It is fundamental in creating light curves and to study brilliant source variability.

- **Sensitivity:** The sensitivity is the minimum flux that an instrument can detect. It is linked to the **Signal to Noise Ratio** (**SNR**), defined as

$$SNR = \frac{C_S}{N} = \frac{S}{\sqrt{\sigma_{\mathrm{S}}^2 + \sigma_{\mathrm{B}}^2 + \sigma_{\mathrm{INS}}^2}} \tag{2.1}$$

  where C_S are the source counts, σ_{S} its error, σ_{B}^2 the error associated to the background and σ_{INS}^2, the error associated to the instrumental noise. As the source and background follow Poisson statistic, their error are the square root of their counts and we obtain:

$$SNR = \frac{S}{\sqrt{S + B + \sigma_{\mathrm{INS}}^2}} \tag{2.2}$$

- **Field of view (FoV):** It is the sky area that can be covered in a single observation (i.e. without moving the telescope aim). It is particular important when doing surveys. The FoV is linked both to the telescope mirror's dimension and to its geometry.

2.1.1 X-ray telescopes

X-ray telescopes have to be in orbit, or at least in the upper layer of the atmosphere, to be able to operate, as the atmosphere is, luckily for us, completely opaque to X-ray wavelengths. Moreover X-ray photons are extremely difficult to reflect by usual mirrors, due to their high penetrative power. However, in 1923 Compton demonstrated that highly polished mirrors can deflect even X-ray photons if they have low incidence angle. There is a critical angle θ_c, under which all the incoming radiation is reflected, a process known as "grazing incidence". θ_c depends on the energy of the incoming photon and on the density of the mirror as $\theta_c \approx 10^{-2}\sqrt{2\rho}/\text{E}$, where ρ is the density of the reflecting material in g/cm^3 and E is the photon energy in keV (Weisskopf 2012). A grazing incidence telescope with just one parabolic mirror could focus X-rays, but only very close to the center of the field of view, as the rest of the image would suffer from extreme coma aberrations. Coma aberration results in off-axis point sources appearing distorted and to have a tail (coma) like a comet. Coma aberrations are usually not important in parabolic mirrors until the incidence angle of the radiation is near the axis of the parabola. However, the grazing incidence needs angles as close to the surface of the mirror as possible. In 1952, Hans Wolter outlined three ways an X-ray telescope could be built using grazing incidence mirror and without suffering coma aberration (Wolter 1952). These are called Wolter telescopes of type I, II, and III. Wolter's key innovation was that, by using two mirrors and a double grazing incidence, it is possible to create a telescope with a usable wide field of view.

X-ray telescope share some characteristic with optical telescope, but also have their own peculiarity and parameters.

- **Angular resolution:** X-ray instruments have PSF heavily dependent on the energy of the incoming photon and on the off-axis angle. High-energy photons give broader PSF, being more difficult to reflect them in the focus. Moreover, farther is a photon from the aimpoint, more difficult becomes to reflect and focus it. Hence, the resolution of X-ray telescope depends both on the energy of the incoming photons and on the off-angle axis. Usually it is defined at the aimpoint, where it has its maximum, for different photon energies and measured as the **HEW** (Half Energy Width), the width of the circle that contains half of the source energy. Moreover, due to the difficulty in reflecting high-energy photons, the angular resolution of X-ray telescopes is never close to the $\theta = 1.22\,\lambda/\text{D}$ limit.

- **Effective Area:** It is a parameter linked to the capability of the X-ray telescope to collect and detect the incoming photons.

$$A_{eff}(E, \theta, x, y) = A_{\text{geom}} \cdot R(E) \cdot V(E, \theta) \cdot QE(E, x, y) \qquad (2.3)$$

  - A_{geom} is the geometric area. It is the area covered by the co-focal shells.

- $R(E)$ is the reflectivity. It is the fraction of photons reflected by the mirrors. It is a function of the incoming photon energy.

- $V(E, \theta)$ is the *vignetting factor*. It is linked to the fraction of photons lost as a function of the off-axis angle (θ).

- $QE(E, x, y)$ is the *quantum efficiency*, the fraction of photons that succeed in producing a signal on the detector. It is a function of the photon energy and of the position on the detector.

- **SNR:** Likewise the optical SNR, it is defined as

$$SNR = \frac{C_S}{\sqrt{C_S^2 + C_B^2}} \tag{2.4}$$

where C_S are the source counts and C_B are the background counts. In X-ray astronomy, the source counts are obtained subtracting the background counts to the counts extracted from a region containing the source, so $C_S = (S + B) - B$. Assuming to be in Poisson regime, the error becomes

$$\sigma_S^2 = \sigma_{S+B}^2 + \sigma_B^2 = (\sqrt{S + B})^2 + (\sqrt{B})^2 = S + B + B = S + 2B \tag{2.5}$$

and the SNR:

$$SNR = \frac{S}{\sigma_S} = \frac{S}{\sqrt{S + 2B}} \tag{2.6}$$

The number of counts depends on the flux, the exposure time, the effective area and the energy bandwidth. The source counts depend also on the efficiency η (the ratio between the number of photons detected and the number of incoming photons). So $S = \eta F_S \Delta t A_{eff} \Delta E$ and $B = F_B \Delta t A_{eff} \Delta E$. The SNR becomes

$$SNR = \frac{\eta F_S \Delta t A_{eff} \Delta E}{\sqrt{\Delta t A_{eff} \Delta E (\eta F_S + 2F_B)}} = \eta F_S \sqrt{\frac{\Delta t A_{eff} \Delta E}{\eta F_S + 2F_B}} \tag{2.7}$$

In low-counts regime ($\eta F_S \ll F_B$)

$$SNR \approx \eta F_S \sqrt{\frac{\Delta t A_{eff} \Delta E}{F_B}} \tag{2.8}$$

From this equation we can obtain the minimum detectable flux, or sensitivity,

$$F_{\min} = \frac{SNR}{\eta} \sqrt{\frac{F_B}{\Delta t A_{eff} \Delta E}} \tag{2.9}$$

23

2.2 The Chandra X-ray Observatory

The Chandra X-ray Observatory is a NASA space telescope launched on July 23$^{\text{rd}}$, 1999. It has the best angular resolution of all X-ray telescopes, thanks to its high quality mirrors. It is composed of four instruments (with different characteristics and used for different scientific purposes) to detect the photons and of an array of mirrors (HRMA) to focus the incoming radiation on the detector.

The *High Resolution Mirror Assembly* (HRMA) is the structure used to focus X-ray photons on the instruments. It is composed of four nested co-focal shells, each made of a paraboloid mirror and an hyperboloid mirror. The mirror configuration is *Wolter I* (Figure 2.2), with a focal length of 10 m.
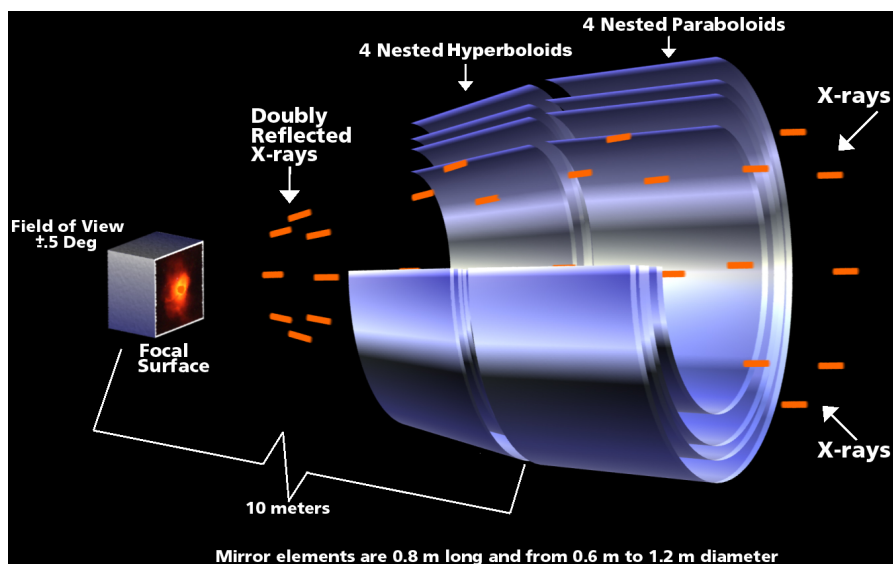

Figure 2.2: Design and functioning of the High Resolution Mirror Assembly (HRMA) on *Chandra* (Illustration: NASA/CXC/D.Berry).

Chandra's mirror are coated with Iridium, ensuring a critical angle of $\theta_c \approx 1°$. The *Wolter I* configuration exploits a double grazing incidence to focus the photons on the instruments, without occurring in coma aberrations. To detect the incoming X-ray photons Chandra has four different instrument, which, however, cannot operate simultaneously.

- **Advanced CCD Imaging Spectrometer (ACIS):** It is composed of two CCD arrays, that record both spatial and energetic information, allowing both imaging and spectroscopy. It has an angular resolution of ≈ 0.5" (HEW) and a spectral resolution of R$\approx 100 - 150$ eV at 1.49 keV (*ACIS Instrument Information* 2010). As we can see from Figure 2.3, there are 2 CCD configuration: ACIS-I, composed of 4 CCD in a 2x2 configuration, and ACIS-S with 6 aligned CCD. Every CCD covers
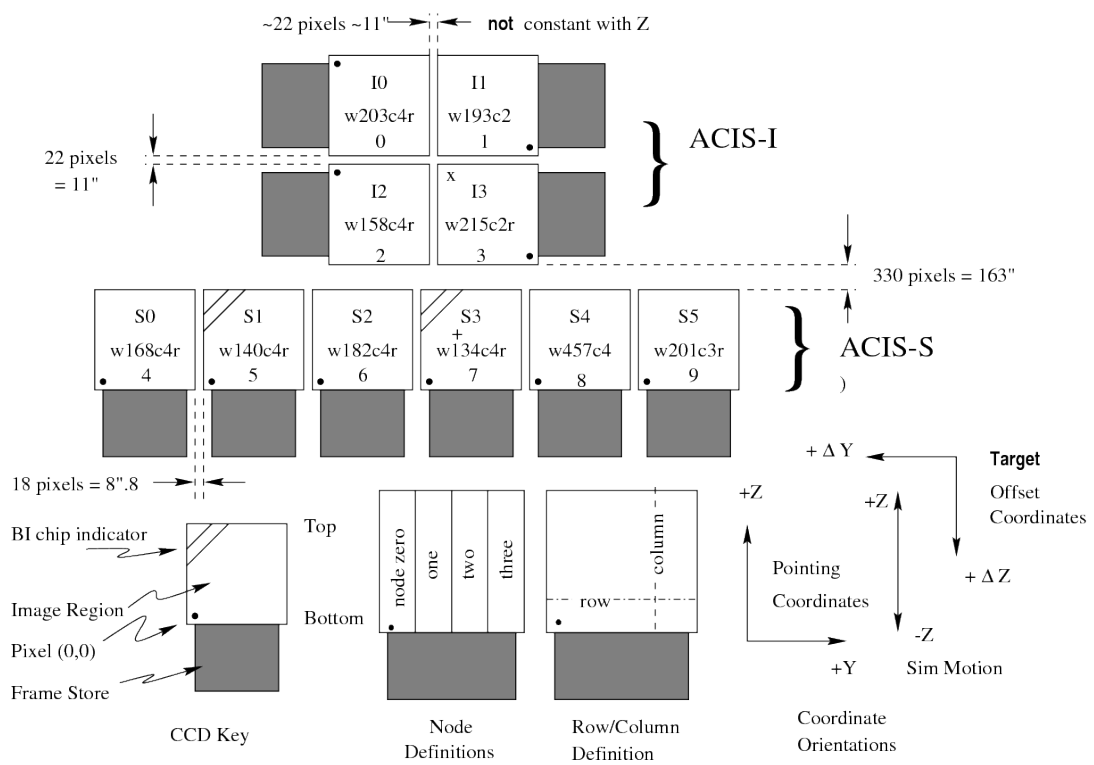
Figure 2.3: Chandra ACIS CCD disposition.

a 8.4'x8.4' sky area and it is a square of 1024x1024 pixels. Each pixel is a square of 24 μm side. All the CCDs, except two, are front illuminated CCDs. S1 and S3 are back illuminated CCD, that ensure greater effective area in the soft band, at the expense of minor effective area in the hard band and higher instrumental noise.

- **High Resolution Camera (HRC):** It is a *microchannel plates* detector with two instruments: HRC-I and HRC-S. The first has a wide (30'x30') field of view, a spatial resolution even better than ACIS and it is used to produce high resolution imaging. HRC-S is usually used together with LETG to produce high-resolution spectral data.

- **High Energy Transmission Grating (HETG) and Low Energy Transmission Grating (LETG):** They are high resolution grating spectrographs. The first has a range of 0.4-10 keV, the latter 0.07-10 keV. Their spectral resolution can be up to E/ΔE$\approx 100 - 1000$.

Given the telescope characteristics, Chandra is the best X-ray telescope to perform deep surveys (i.e. surveys with the objective to see faint sources). In fact, thanks to the high angular resolution, a good SNR can be achieved, as the majority of the source photons is focused on a small area with low background: at the aim point, approximately 90% of the encircled energy lies within 4 pixels (2 arcsec) at 1.49 keV and within 5 pixels (2.5 arcsec) at 6.4 keV. This allows to detect faint sources, as even 4 counts can be considered a detection.

In our work we used data taken with the ACIS-I instrument, that assured us a FoV of 16.9x16.9 arcmin^2, an energy resolution of 130 eV (at 1.49 keV) and 280 eV (at 5.9 keV) at the aim point, and a time resolution of 3.2 s.

2.3 The COSMOS field

All the data presented in this work come from the COSMOS field. The field takes its name from the first survey program that studied it. The COSMOS field is a 1.4°x1.4° square, centered at (J2000): RA +150.11916667 DEC +2.20583333. The field does no contain any bright X-ray, UV, or radio sources. Relative to other equatorial fields, COSMOS has exceptionally low and uniform Galactic extinction.

2.3.1 The COSMOS survey

The Cosmic Evolution Survey (COSMOS) (Scoville et al. 2007) is a deep, wide area, multi-wavelength survey, aimed at measuring the evolution of galaxies on scales from a few kpc to tents of Mpc. The field has been observed at all accessible wavelengths, from the X-rays to the radio bands, with most of the major space-based (such as Hubble,

Spitzer, GALEX, XMM, Chandra, Herschel, NuSTAR) and ground based telescopes, as Keck, Subaru, Very Large Array (VLA), European Southern Observatory Very Large Telescope (ESO-VLT), United Kingdom Infrared Telescope (UKIRT), the National Optical Astronomical Observatory (NOAO) Badde and Blanco telescopes, the Canada France Hawaii Telescope (CFHT), and others.

2.3.2 The Chandra COSMOS Survey

The X-ray data, used in my thesis work, come from the COSMOS Legacy survey, composed of data from the C-COSMOS survey (e.g. Elvis et al. 2009), that covered the central region of the COSMOS field, and new 2016 Chandra observations (Civano et al. 2016) covering the remaining area of the field.

C-COSMOS

The Chandra COSMOS Survey (C-COSMOS) is a large, 1.8 Ms, Chandra program that imaged the central 0.5 deg^2 of the COSMOS field with an effective exposure of ~ 160 ks, and an outer 0.4 deg^2 with an effective exposure of ~ 80ks (Figure 2.4).

The survey used the ACIS-I CCD imager of the Chandra X-ray Observatory. C-COSMOS employed a series of 36 partially-overlapping pointings of 50 ks each to have a uniform depth of $\sim 1.9 \cdot 10^{-16}$ erg/s/cm^2 (0.5–2 keV) over the inner area. The overlapping tiling strategy gives highly uniform exposure, therefore a well-defined flux limit. The observations took place in two main blocks: 2006 December–2007 January and 2007, April–June. The mean effective exposure time per field was 46.3 ks, when only the good time intervals were used. With only one exception, the range of exposures over the fully covered inner region varied by just ± 2.0 ks (4%).

Three bands were used for source detection: Soft (0.5-2 keV), Hard (2-10 keV) and Full (0.5-10 keV). C-Cosmos detected (in at least one band) 1761 X-ray sources down to a probability threshold chosen to balance completeness (the fraction of true sources detected) against reliability (the fraction of false sources detected)(see Elvis et al. 2009). We will refer to data from this catalog as **"cat09"**.

COSMOS Legacy

C-COSMOS only covered a quarter of the whole COSMOS field at ~ 160 ks depth, plus 0.5 deg^2 at ~ 80 ks depth (Figure 2.5). The Chandra COSMOS-Legacy survey is the combination of the old C-COSMOS survey and 2.8 Ms of new Chandra ACIS-I observations (56x50 ks pointings) approved during Chandra Cycle 14. COSMOS-Legacy uniformly covers the ~ 1.7 deg^2 COSMOS at ~ 160 ks depth, expanding on the deep C-COSMOS area by a factor of ~ 3, for a total area covered of ~ 2.2 deg^2. Fifty-six ACIS-I pointings were performed, 11 of which were scheduled as two or more separate
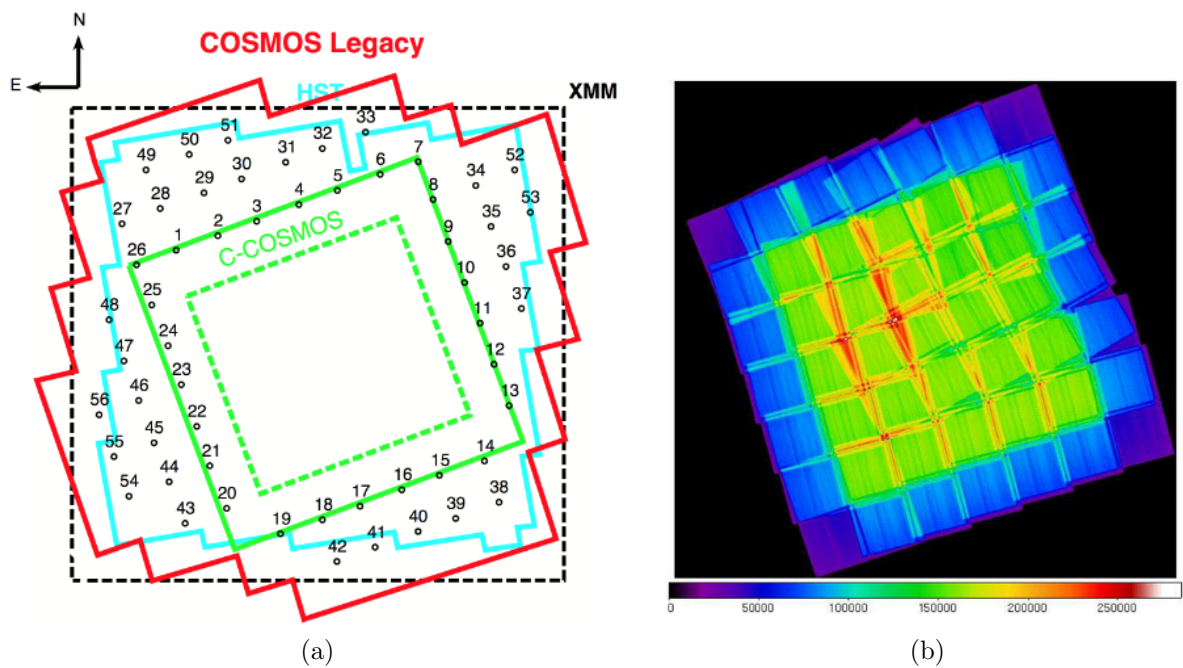
Figure 2.4: (a) COSMOS-Legacy tiling (red) compared to the area covered by HST (cyan), C-COSMOS (green solid: total area; green dashed: deeper area) and XMM-COSMOS (black) (Civano et al. 2016). The numbers refer to the number of the COSMOS Legacy observations, the black dot are their aimpoint. (b) Exposure map for the C-COSMOS survey in the soft (0.5-2 keV) band. The color bar gives the achieved effective exposure in units of seconds (Elvis et al. 2009).

28

observations, for a total of 68 pointings. The observations took place in four blocks: November, 2012 to January, 2013; March to July, 2013; October, 2013 to January, 2014; and March, 2014. The mean net effective exposure time per field was 48.8 ks (Figure 2.5). The tiling strategy used has given an approximately uniform combined PSF across the survey. The mean combined PSF width (size at 50% of the encircled energy fraction in the 0.5-7 keV band) peaks at around 3", 80% of the field has a PSF in the range 2"-4" (Civano et al. 2016).
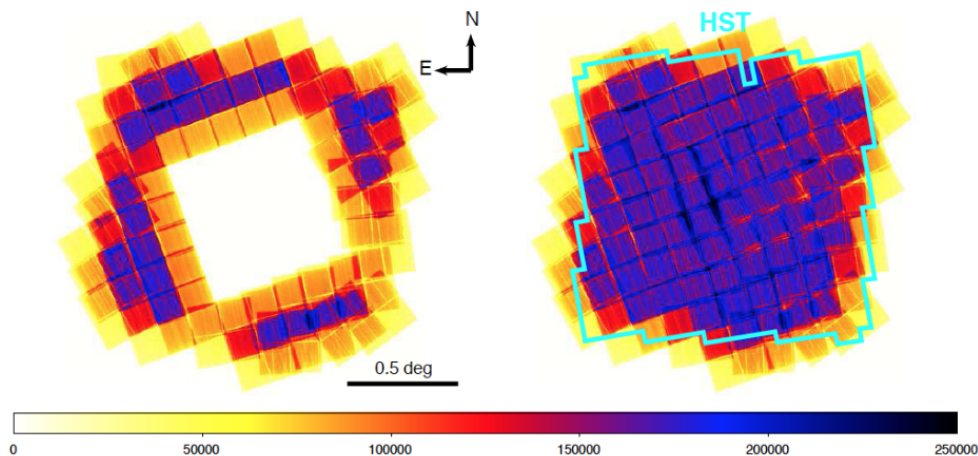

Figure 2.5: The mosaic of the exposure maps for the 2016 observations (left) and for the whole COSMOS-Legacy survey (right) in the Full band. The color bar gives the achieved effective exposure in units of seconds (Civano et al. 2016).

The COSMOS-Legacy survey shares the same tiling layout, exposure time per field and roll angle range of C-COSMOS. The same procedure and the same significance threshold for source detection were applied to the new dataset. In the new data, 2273 X-ray sources were detected, for a total of 4016 sources in the whole COSMOS-Legacy survey.

We will refer to data from COSMOS Legacy catalog as **"cat16"**.

2.3.3 COSMOS2015 Catalog

The optical and IR data, used in this thesis work, come from the COSMOS2015 catalog.

The COSMOS2015 catalog (Laigle et al. 2016) contains precise photometric redshifts and 30-band photometry, for more than half a billion objects in the COSMOS field. It has new, compared to previous versions, Y J H K_s images from the UltraVISTA-DR2 survey, Y-band from Subaru/Hyper-Suprime-Cam and infrared data from the Spitzer Large Area Survey with the Hyper-Suprime-Cam Spitzer legacy program. The COSMOS2015

catalog also offers a match with X-ray, near ultraviolet, and Far-IR catalogs, coming, respectively, from Chandra, GALEX, MIPS/Spitzer, PACS+SPIRE/Herschel.

In Table 2.1, the 30 photometric bands of the COSMOS2015 catalog.

2.3.4 [NeV] sample

In our work we studied type 2 AGN from a catalogue of [NeV] selected type 2 AGN (Mignoli et al. 2013). This catalogue will be referred to as [NeV] sample. The galaxy composing the [NeV] sample were selected from the zCOSMOS-Bright spectroscopic survey (Lilly et al. 2007, 2009).

zCOSMOS Bright survey

The zCOSMOS project (Lilly et al. 2007) is a major redshift survey of galaxies in the COSMOS field, using 600 hr of clear dark observing time on the VLT. The survey is divided into two parts: the first is composed of spectra of $\sim 20\,000$ galaxies selected to have $I_{AB} < 22.5$ across the COSMOS field and it is named zCOSMOS Bright survey. The second part, the zCOSMOS deep survey, consists of $\sim 10\,000$ spectra of galaxies with $B_{AB} < 25.25$, color-selected to have redshift approximately in the $1.4 < z < 3.0$ range. The zCOSMOS Bright survey was designed to have a high and uniform sampling rate across most of the COSMOS field, with a high success rate in measuring redshifts, and to have sufficient velocity accuracy to detect structures down to the scale of galaxy groups.

The input catalogue, from which the targets were selected, was based on "total" F814W magnitudes derived from the 0.1" resolution HST images (Koekemoer et al. 2007). Observations for the sample were carried out with the VIMOS multi-slit spectrograph mounted on the 8m VLT/UT3 telescope; it operates in the 5500 – 9700 Å range. The final redshifts were determined purely from spectral analysis, independently of photometric redshifts or other information about the objects.

[NeV] sample

The [NeV] sample is a sample of 94 type 2 AGN in the COSMOS field, selected, on the basis of their spectral properties, from the zCOSMOS 20k Bright survey.

Among the 20707 entries included in the zCOSMOS Bright spectroscopic catalog (version 4.2), a total of 18141 galaxies and AGN have measured redshifts, 1031 objects (5%) are spectroscopically classified as stars, and 1535 objects (7%) remain without redshift identification.

The first step in the selection process consisted in the exclusion of AGN previously identified as type 1 and sources with $z < 0.65$, to be sure that both the [NeV]3346Å and [NeV]3426Å emission lines fallen within the spectral range.

Instrument /Survey	Filter	Central λ (Å)	Width (Å)
GALEX	NUV	2313.9	748
MegaCam/CFHT	u^*	3823.3	670
Suprime-Cam /Subaru	B	4458.3	946
	V 5477.8		955
	r	6288.7	1382
	i^+	7683.9	1497
	z^{++}	9105.7	1370
	IA427	4263.4	206.5
	IA464	4635.1	218
	IA484	4849.2	228.5
	IA505	5062.5	230.5
	IA527	5261.1	242
	IA574	5764.8	271.5
	IA620	6233.1	300.5
	IA679	9781.1	336
	IA709	7073.6	315.5
	IA738	7361.6	323.5
	IA827	8244.5	343.5
	NB711	7119.9	72.5
	NB816	8149.4	119.5
HSC/Subaru	Y	9791.4	820
VIRCAM /VISTA (UltraVISTA-DR2)	Y^{UD}	10214.2	970
	J^{UD}	12534.6	1720
	H^{UD}	16453.4	2900
	K_S^{UD}	21539.9	3090
WIRCam /CFHT	k_S	21590.4	3120
	H	16311.4	3000
IRAC/*Spitzer* (SPLASH)	ch1	35634.3	7460
	ch2	45110.1	10110
	ch3	57593.4	14140
	ch4	79594.9	28760

Table 2.1: Summary of COSMOS2015 photometric bands. The central wavelength is the median wavelength weighted by transmission and the widths are defined using the half-maximum transmission points (Laigle et al. 2016).

The [NeV] selection procedure consisted of two steps. At first, all galaxy spectra were smoothed with a 3 pixel boxcar and plotted in the rest frame, in order to be able to detect the [NeV]3426Å emission line and compile a list of candidate AGN. The threshold for the emission line was 2.5σ above the continuum. Moreover, the line peak had to be within 20 Å from the expected position. The second phase consisted in an examination of sky-subtracted spectra to eliminate spurious detections, to mark as secure candidates galaxies where both [NeV] emission were lines clearly visible at the expected positions and to accurately verify the reliability of the [NeV]3426Å lines when the three times fainter [NeV] 3346 Å feature was not detectable. This procedure led to the identification of 94 zCOSMOS Bright AGN (in the $0.65 < z < 1.20$ redshift range) with a secure detection of [NeV] in their spectra. No broad line components were found in the selected spectra. The selection process is explained in details in Mignoli et al. 2013.

Several works have been published exploiting the [NeV] sample. In Mignoli et al. (2013) the excess luminosity of [OII] lines with respect to [NeV] lines was suggesting an enhanced star formation in the obscured population with respect to the unobscured one. The same work used the [NeV] sample to investigate the completeness of various AGN selection method ([NeV] selection - lines ratio selection - blue diagnostic diagram - Mass-Excitation diagnostic diagram (Juneau et al. 2011)). In 2014, 69 AGN in the [NeV] sample and covered by C-COSMOS observations were selected. The X-ray analysis for the X-ray detected sources were carried out to characterize spectral properties and estimate the CT fraction using the X/[NeV] ratio. It was found that the X-ray detected sources have a wide range of absorption. Approximately 40% of the X-ray undetected sources was composed of CT AGN and their space density was in good agreement with X-ray background synthesis model predictions (Vignali et al. 2014).

Thanks to the COSMOS Legacy data, all the 94 [NeV] selected sources has, now, X-ray coverage. Our thesis work aim at studying their X-ray, optical and IR properties, exploiting the "new" set of data. This will allow us to the update the fraction of X-ray detected sources in the [NeV] sample. Moreover, with these "new" data, we will be able to put better constrain the X-ray properties of the sample and, via the X/[NeV] ratio, on the CT fraction. In addition, the use of COSMOS2015 data of the [NeV] selected sources will allow us to perform optical-to-FIR SED fitting analysis, aiming at constrain both AGN properties, such as intrinsic luminosity and obscuration, and host-galaxy characteristics, such as stellar mass and star formation ratio.

Chapter 3

X-ray spectral analysis

We performed X-ray spectral analysis of the sample, with the aim of studying its characteristics and, in particular, the absorption and the fraction of obscured and CT sources.

The use narrow [NeV] emission lines as selection method assured us that the sample is composed only of type 2 AGN in the $0.65 < z < 1.20$ redshift range. As AGN population synthesis models predict that the missing fraction of the XRB is produced by heavily obscured objects and that the density of those in the $10^{43} < L < 10^{44}$ erg/s luminosity range should peak at $z \approx 1$, the study of X-ray spectral properties of our sample offers a good opportunity to shed light to this still open question.

We studied the X-ray properties of the sample via spectral analysis; the spectra were already been extracted by Marchesi et al. (2016). For the sources with X-ray detection, we focused on characterizing the source obscuration as well as obtaining both observed and intrinsic luminosity. We also used the rest frame $2 - 10$ keV flux (not corrected for the obscuration) to obtain the X/[NeV] ratio, that provided us with a second estimate of the source absorption. For the sources without X-ray detection we computed the flux upper limits and used those to calculate the X/[NeV] upper limits, thus obtaining an estimate on the source obscuration.

In section 3.1 we present the main properties of the sample, in section 3.2 the spectra extraction procedure. In section 3.3 we discuss the X-ray spectral analysis of the detected sources, with the presentation of the model used in the spectral fitting (section 3.3.1), the use of HR and simulated spectra to help in the fitting process (sec 3.3.2), the sources with peculiar spectral features (sec 3.3.3 and 3.3.4) and the results (sec 3.3.5). In section 3.4 we discuss the analysis of the X-ray undetected sources. Finally, in section 3.5, we present the X-ray spectral analysis results. Errors on the X-ray parameters are reported at the 90% confidence levels for one parameter of interest.

3.1 The sample

As reported in section 2.3.4, in my thesis work I analyzed a sample of 94 [NeV] selected type 2 AGN. In Table 3.1 we report the main information about this data set, as obtained by Mignoli et al. (2013). For the X-ray detected sources, we will refer to them with the *Chandra* COSMOS ID, where *cid* are the sources detected in the C-COSMOS survey and *lid* is associated with those detected in the COSMOS-Legacy survey.

The sample was composed of sources from redshift $z = 0.6606$ to $z = 1.1767$, with mean $z = 0.85 \pm 0.13$ and a median $z = 0.86$. The mean (aperture corrected) [NeV] flux was $F_{[NeV]} = (1.81 \pm 1.23) \cdot 10^{-17}$ erg/s, with median $F_{[NeV]} = 1.44 \cdot 10^{-17}$ erg/s, the mean [NeV] Equivalent Width $EW_{[NeV]} = -18.17 \pm 15.81$ Å with median $EW_{[NeV]} = -13.9$Å. The values reported together with the means are the standard deviations.

zCOSMOS-ID	z	RA	DEC	Flux [NeV] $\cdot 10^{-17}$ erg/s/cm^2	EW [NeV] Å
803886	0.8962	150.52977	1.725586	3.00 ± 0.11	-24.88 ± 1.05
803996	0.8326	150.49176	1.772574	3.19 ± 0.21	-11.7 ± 0.79
804237	1.0001	150.429977	1.684451	5.82 ± 0.06	-34.62 ± 0.42
804431	0.702	150.383041	1.745181	1.42 ± 0.33	-19.64 ± 5.37
805117	0.9999	150.22049	1.72972	1.19 ± 0.02	-11.79 ± 0.25
807963	0.9198	149.592178	1.682943	2.56 ± 0.35	-6.97 ± 0.96
809056	1.0705	150.766266	1.9035	1.12 ± 0.02	-9.13 ± 0.18
809579	0.9195	150.637222	1.873909	0.70 ± 0.12	-8.78 ± 1.58
809597	0.9653	150.632751	1.878463	2.26 ± 0.35	-3.34 ± 0.51
810378	0.9707	150.467621	1.935703	2.48 ± 0.18	-32.35 ± 2.41
811284	0.9558	150.269028	1.891863	3.30 ± 0.05	-31.81 ± 1.01
811645	0.8092	150.19516	1.84154	0.91 ± 0.16	-9.81 ± 1.93
811887	0.7297	150.144485	1.853603	4.90 ± 0.15	-34.27 ± 1.56
812111	0.7106	150.097778	1.845246	2.71 ± 0.78	-7.08 ± 2.03
812193	0.898	150.080215	1.84957	1.19 ± 0.10	-9.39 ± 0.87
812432	0.6611	150.025848	1.9264	10.10 ± 0.73	-32.49 ± 3.17
812665	0.7301	149.971375	1.885972	1.60 ± 0.03	-8.39 ± 0.19
812953	0.7742	149.90097	1.947447	2.43 ± 0.14	-25.41 ± 1.72
813250	0.7302	149.830582	1.902132	2.09 ± 0.14	-18.81 ± 2.70
813287	0.7488	149.820557	1.811719	1.56 ± 0.12	-3.41 ± 0.26
813366	0.6685	149.803879	1.795451	5.54 ± 1.18	-18.77 ± 4.76
813460	0.6646	149.780212	1.826555	0.88 ± 0.13	-7.76 ± 1.29
813850	0.6606	149.697205	1.905195	2.06 ± 0.13	-4.16 ± 0.24
814229	0.7618	149.60704	1.870499	3.86 ± 0.04	-30.68 ± 0.33
816439	0.8993	150.510666	2.029207	9.66 ± 0.13	-19.11 ± 0.17
817002	0.8649	150.418167	1.976701	3.90 ± 0.08	-17.25 ± 0.41

zCOSMOS-ID	z	RA	DEC	Flux [NeV] $\cdot 10^{-17}$ erg/s/cm^2	EW [NeV] Å
817871	0.6743	150.248688	1.972335	2.50 ± 0.44	-7.06 ± 0.06
817886	0.9603	150.244629	2.008821	0.73 ± 0.14	-6.43 ± 1.40
817977	0.9591	150.222534	2.01167	0.78 ± 0.04	-6.25 ± 0.34
818408	0.6689	150.135941	2.120217	3.93 ± 0.92	-19.02 ± 2.49
818478	0.8946	150.122849	2.085841	1.71 ± 0.05	-11.18 ± 0.38
819116	0.715	149.972672	2.049503	1.15 ± 0.71	-16.76 ± 8.91
819306	0.9394	149.929489	2.110626	1.92 ± 0.22	-19.81 ± 2.73
819469	0.6865	149.893555	2.107714	3.01 ± 0.21	-21.41 ± 1.61
819927	0.6973	149.768951	2.090306	2.44 ± 0.16	-14.38 ± 1.25
820589	0.8796	149.606232	2.062873	2.28 ± 0.21	-11.54 ± 1.08
820695	0.7642	149.580399	1.967788	2.79 ± 0.08	-15.48 ± 0.55
820742	0.9997	149.570389	1.990572	1.37 ± 0.04	-10.34 ± 0.33
820983	0.6752	149.521255	2.079391	2.37 ± 0.02	-9.33 ± 0.15
822904	0.8357	150.504761	2.224231	1.08 ± 0.17	-14.79 ± 0.40
823097	0.8044	150.469711	2.231583	3.57 ± 0.13	-35.36 ± 1.66
823162	0.8489	150.458023	2.260842	2.79 ± 0.25	-23.93 ± 2.28
823537	0.9225	150.380005	2.128212	1.79 ± 0.13	-11.51 ± 1.61
824025	0.8503	150.273239	2.273062	3.58 ± 0.05	-26.06 ± 0.32
824548	0.748	150.16394	2.29095	1.00 ± 0.15	-11.31 ± 1.63
824736	1.1427	150.123535	2.149813	6.85 ± 0.24	-45.13 ± 1.97
825282	0.9588	150.01886	2.147779	3.76 ± 0.87	-13.42 ± 3.22
825838	0.7864	149.907333	2.169099	1.77 ± 0.15	-7.97 ± 0.68
825958	0.7026	149.884903	2.238505	2.41 ± 0.33	-8.26 ± 1.28
826023	0.9508	149.872528	2.162082	1.93 ± 0.16	-38.2 ± 3.84
826095	0.764	149.856766	2.273134	2.00 ± 0.41	-5.2 ± 1.19
826693	0.6994	149.733231	2.132358	1.03 ± 0.10	-24.64 ± 3.61
826908	1.0246	149.695847	2.267107	6.41 ± 1.13	-29.83 ± 5.38
829551	0.8927	150.525146	2.456414	1.81 ± 0.53	-15.86 ± 5.34
829938	0.8821	150.446548	2.366708	1.61 ± 0.14	-12.62 ± 1.13
829955	0.8913	150.444427	2.369805	3.10 ± 0.13	-11.38 ± 0.49
830027	0.9307	150.431183	2.359476	3.53 ± 0.09	-24.64 ± 0.56
831655	0.7567	150.112289	2.387432	1.08 ± 0.13	-12.19 ± 1.39
831966	0.7295	150.062149	2.455	2.14 ± 0.46	-3.29 ± 0.76
832252	0.7878	150.013412	2.333157	0.80 ± 0.18	-16.57 ± 3.70
832576	0.7331	149.948395	2.449379	1.11 ± 0.35	-8.97 ± 5.20
832803	0.9274	149.90564	2.318273	2.36 ± 0.25	-18.62 ± 2.04
832900	1.023	149.884171	2.33815	8.55 ± 0.19	-40.99 ± 0.95

zCOSMOS-ID	z	RA	DEC	Flux [NeV] $\cdot 10^{-17}$ erg/s/cm^2	EW [NeV] Å
832907	0.9608	149.883438	2.373879	2.07 ± 0.06	-20.06 ± 0.75
833208	0.9106	149.826523	2.396749	1.08 ± 0.05	-15.24 ± 0.72
833510	0.9444	149.768112	2.431331	3.84 ± 0.22	-14.42 ± 0.89
833904	0.8643	149.691101	2.335542	1.55 ± 0.36	-10.89 ± 0.79
834572	0.8475	149.561752	2.421948	0.90 ± 0.09	-11.04 ± 3.57
836036	0.8819	150.632965	2.585403	2.33 ± 0.27	-3.56 ± 0.43
836868	0.6793	150.477036	2.494094	7.21 ± 0.26	-8.67 ± 1.37
837072	1.1475	150.439438	2.543515	4.08 ± 0.27	-74.82 ± 3.83
837402	0.8835	150.384003	2.588294	1.25 ± 0.07	-40.48 ± 4.31
837589	0.9214	150.347275	2.570119	1.32 ± 0.07	-10.25 ± 0.66
837988	0.7034	150.274323	2.511393	1.03 ± 0.58	-8.88 ± 0.50
839683	0.8887	149.968658	2.580962	2.04 ± 0.44	-5.76 ± 2.96
839719	0.8916	149.963074	2.613115	3.99 ± 0.43	-11.62 ± 3.01
840085	0.7535	149.91066	2.55467	3.21 ± 0.25	-3.87 ± 1.16
840744	0.7353	149.772919	2.555765	2.77 ± 0.40	-5.72 ± 0.45
841281	0.7348	149.655716	2.600811	6.65 ± 0.21	-16.42 ± 0.61
841340	1.1733	149.641724	2.476275	5.82 ± 0.63	-28.65 ± 3.24
841734	1.0062	149.552429	2.590777	2.58 ± 0.04	-10.61 ± 0.17
843107	0.8499	150.676208	2.772941	2.44 ± 0.67	-6.26 ± 1.76
844011	0.8626	150.497971	2.755856	0.72 ± 0.04	-13.9 ± 0.81
845677	0.7264	150.155685	2.787673	1.57 ± 0.02	-29.23 ± 0.67
846342	0.7353	150.041229	2.634787	6.32 ± 0.34	-20.14 ± 1.05
846478	1.1767	150.015457	2.665832	5.75 ± 0.32	-30.12 ± 1.90
846722	0.7681	149.971298	2.791711	1.09 ± 0.18	-5.16 ± 1.01
846946	0.7379	149.921646	2.638877	1.03 ± 0.17	-10.63 ± 2.18
847446	1.0273	149.815765	2.650275	2.06 ± 0.21	-19.59 ± 1.95
847932	0.6789	149.696823	2.672763	2.14 ± 0.71	-20.82 ± 7.40
850792	1.0151	150.227554	2.845847	1.29 ± 0.16	-10.49 ± 1.18
851740	1.0245	149.899109	2.820019	3.36 ± 0.02	-16.43 ± 0.16
900121	1.1684	149.597076	2.441275	3.75 ± 0.07	-122.5 ± 2.41
910023	0.9802	150.491974	2.458913	1.30 ± 0.04	-30.61 ± 0.85

Table 3.1: Main properties of the [NeV] sample. Columns are as follows: zCOSMOS ID, redshift and coordinates (RA, Dec); aperture corrected [Ne V] flux; [Ne V] equivalent width.

Using data from "cat16" (see section 2.3.2), 36 [NeV] selected type 2 AGN were detected by *Chandra* within 1.5″ from the optical position, with a maximum displacement of 1.33″ and a mean displacement of 0.45″. In table 3.2 we show the sources with X-ray detection. The CV+14 sample had 72 [NeV] AGN fallen in C-COSMOS mosaic, 23 of those with X-ray detection and a mean displacement of 0.46″ (Vignali et al. 2014).

To check the improvement with respect to CV+14 ascribed to the use of the 2016 COSMOS Legacy data (see section 2.3.2), we compared the "cat16" exposure time (see Civano et al. 2016) for each source with those from "cat09". The former ranges from 49 ks to 239 ks with a mean of 159 ± 33 ks, the latter from 36 ks to 190 ks, with a mean of 116 ks. In Figure 3.1 we compare these exposure times. It is worth noticing that the 2016 data had more source detected (the thirteen with only blue bars) and a more uniform distribution of exposure times, as the vast majority of the sources has an exposure time around 150 ks. We also created the $0.5 - 2keV$ exposure map, calculated
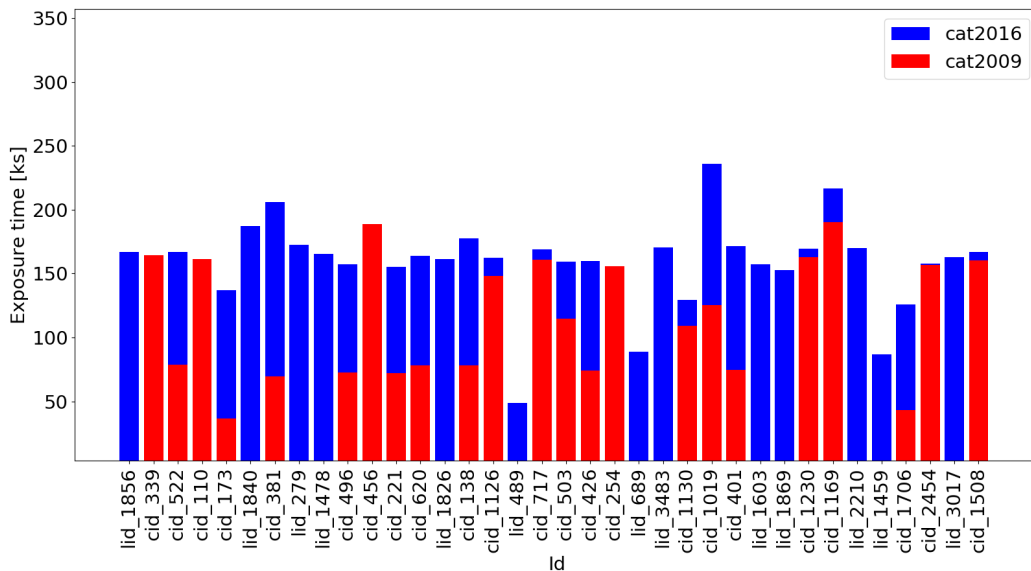

Figure 3.1: Comparison between C-COSMOS ("cat09", red) and COSMOS Legacy ("cat16", blue) exposure time. Sources with only blue bar are those that were undetected in the C-COSMOS survey either because of the lower exposure or because are not in the C-COSMOS field (which - I remember - covers only the inner part of the COSMOS field). We note that the COSMOS Legacy survey granted a more uniform coverage of the field and a general improvement in the source exposure times.

the exposure times of our sources and compared them with those obtained in CV+14. These exposure time are reported in Table 3.2. In Figure 3.2 we show a comparison between the exposure times. It is easy to note that the sources with the most significant improvement in exposure time are those with shorter exposure times in the previous survey. This was ascribed to the fact that these sources are in the outer region of the

zCOSMOS-ID	ID	Ncts 2019	Ncts CV+14	Exp Time 2019 ks	Exp Time CV+14 ks
841281	lid 1856	1827 ± 43		149	
819469	cid 339	373 ± 19	302 ± 17	165	161
833510	cid 522	336 ± 18	151 ± 12	157	78
831966	cid 110	313 ± 18	248 ± 16	163	156
820742	cid 173	242 ± 16	77 ± 9	117	53
841734	lid 1840	216 ± 15		161	
817002	cid 381	208 ± 14	73 ± 9	169	91
836036	lid 279	173 ± 13		157	
803996	lid 1478	168 ± 13		155	
816439	cid 496	165 ± 13	75 ± 9	138	72
832900	cid 456	162 ± 13	153 ± 12	178	181
813287	cid 221	142 ± 12	48 ± 7	147	63
846478	cid 620	126 ± 11	55 ± 7	158	79
841340	lid 1826	109 ± 10		154	
837988	cid 138	99 ± 10	76 ± 9	147	73
843107	lid 489	93 ± 10		48	
825282	cid 1126	93 ± 10	84 ± 9	142	164
829955	cid 717	85 ± 9	61 ± 8	162	162
833208	cid 503	80 ± 9	59 ± 8	139	132
833904	cid 426	75 ± 9	42 ± 6	149	73
812111	cid 254	60 ± 8	44 ± 7	149	146
820983	lid 689	59 ± 8		81	
813850	lid 3483	51 ± 7		162	
825838	cid 1130	48 ± 7	34 ± 6	113	124
813250	cid 1019	41 ± 6	25 ± 5	205	156
809597	lid 1603	39 ± 6		130	
810378	cid 401	39 ± 6	25 ± 5	157	75
900121	lid 1869	36 ± 6		136	
840085	cid 1230	35 ± 6	23 ± 5	163	163
817977	cid 1169	21 ± 5	30 ± 6	193	214
840744	lid 2210	18 ± 4		163	
804237	lid 1459	17 ± 4		75	
836868	lid 3017	15 ± 4		152	
826095	cid 2454	15 ± 4	10 ± 3	154	150
820695	cid 1706	15 ± 4	56 ± 2	115	36
817871	cid 1508	11 ± 3	11 ± 3	160	159
mean		156 ± 33	74 ± 72	146 ± 30	120 ± 48

Table 3.2: X-ray detected sources. Columns are as follows: zCOSMOS id; *Chandra* COSMOS id; Ncts 2019: background-subtracted counts (obtained from spectral analysis) of our sample; Ncts CV+14: background-subtracted counts (obtained from spectral analysis) of cat09 data from Vignali et al. 2014; Exp Time 2019: $0.5 - 2 keV$ exposure time (ks) of our sample; Exp Time CV+14: $0.5 - 2$ keV exposure time (ks) of cat09 data from Vignali et al. 2014.

C-COSMOS survey, thus with a lower effective exposure with respect to the inner region (see sec 2.3.2).
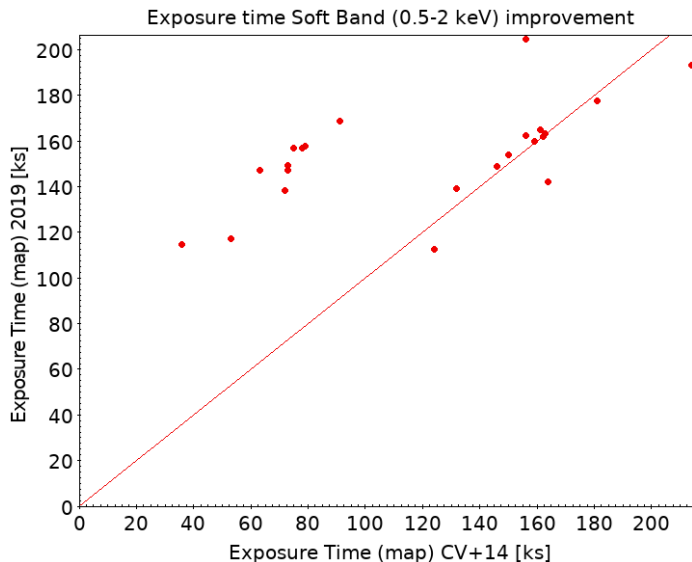

Figure 3.2: Comparison between this work and CV+14 $0.5 - 2$ keV exposure time of the previously detected sources. The sources that are in the outer region of the C-COSMOS survey, hence with lower (CV+14) exposure times, are those which benefit the most from the new COSMOS Legacy data.

Using *Xspec* we obtained the number of net (background-subtracted) count of each source. We compared them with those from "CV+14", as we can see in Figure 3.3. On average, we have an improvement by a factor two, going from a mean of Ncts $= 74 \, (\sigma = 72)$ to Ncts $= 156 \, (\sigma = 33)$. The source with the highest number of counts (1827) is *lid* 1856, the one with the lowest (11) is *cid* 1508. The mean background incidence (i.e. the fraction between the background counts and the total counts measured in the source region) was 15.6% and the median 9.6%.

We divided or sample into two groups: the **high-counts** sample, composed of 17 sources with net count > 90, and the **low-counts** sample, 19 sources with net counts < 90. The high-count sample had a mean background incidence of 6.2% and a median of 5.5%; while the low-count sample had a mean of 22.1% and a median of 19.9%. Unsurprisingly, the low-count sample has, on average, a higher background incidence.

3.2 Extraction of the X-ray spectra

For the source with X-ray detection we performed an analysis of their spectra. The spectra were extracted by S. Marchesi as described in Marchesi et al. 2016.
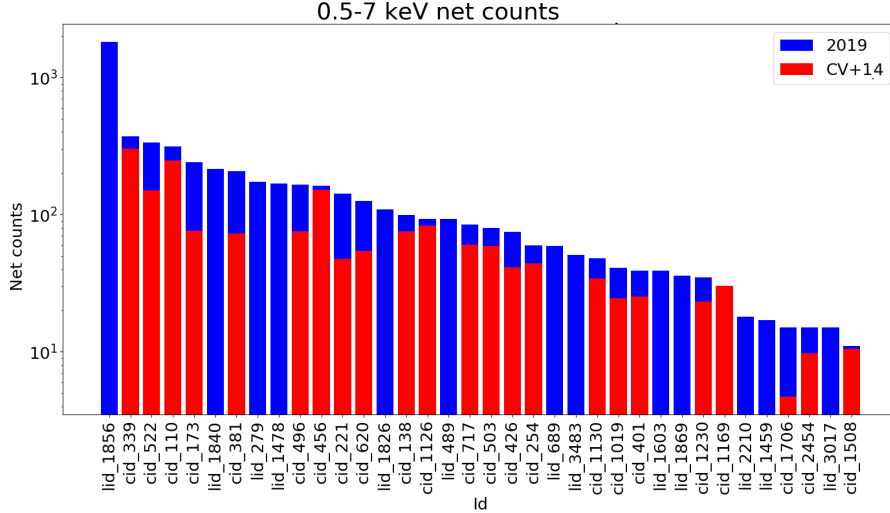
Figure 3.3: Bar charts showing the the $0.5 - 7$ keV net (background-subtracted) counts comparison between this work and CV+14. As in previous charts, red are the CV+14 data based on C-COSMOS survey, while blue are this work data based on COSMOS Legacy survey. Sources with only blue bar are those with X-ray detection in the COSMOS Legacy survey but not in the C-COSMOS.

The spectra extraction was carried out with the *CIAO* tool `specextract`. *CIAO* (Fruscione et al. 2006) is a software package developed by the Chandra X-Ray Center for analyzing data from the *Chandra X-ray Telescope*. The source spectra extraction consisted in two steps. First, circular regions of radius r_{90} were defined around each source in each observation that contained the source. r_{90} (i.e. the radius than contains 90% of the PSF in the $0.5 - 7$ keV (observed-frame) band) was computed, for each observation and source, with the *CIAO* tool `psfsize_srcs`. Then, the `specextract` tool was used to create source and background spectra, along with the response files ARF and RMF, of each extraction region from the event files.

The background spectra were extracted from event files in which the detected sources were removed to avoid contamination. The background extraction regions were annuli centered on the source position with inner radius $r_{90} + 2.5''$ and outer radius of $r_{90} + 20''$. These radii were chosen to avoid contamination from the source emission and to have enough counts to obtain a reliable background spectrum.

Finally, for each source, the spectra of from the individual observations were combined in a single spectrum, via the *CIAO* tool `combine_spectra`. This tool also associated background spectra and source and background response files (ARF and RMF).

3.3 X-ray spectral analysis

To analyze our source spectra we used the version 12.10.1 of *Xspec*, an X-ray spectral fitting software (Arnaud 1996). The spectral fitting works minimizing the statistic to find the best-fit model parameters for the current data. The nature of our data is intrinsically Poissonian; however, if a number sufficiently large of events is considered, the Poisson statistic tends to be a Gaussian one. Hence, for the high-counts sample we rebinned the source counts depending on their number and used Gaussian statistic. The sources with Ncts > 500 were rebinned at 25 counts per bins, the sources with 200 < Ncts < 500 at 15 counts per bin and the sources with 90 < Ncts < 200 at 10 counts per bin. The low-counts sources were rebinned at one count per bin and we used Cash statistic (Cash 1979). Adopting different statistics on the basis of the goodness of the data (i.e. the number of net counts) is a pretty standard approach.

The statistics used in parameter estimation is the maximum likelihood. This is based on the intuitive idea that the best values of the parameters are those that maximize the probability of the observed data given the model. The likelihood is defined as the total probability of observing the data given the model and current parameters. In practice, the statistics used is twice the negative log likelihood.

The likelihood for Gaussian data is

$$L = \prod_{i=1}^{N} \frac{1}{\sqrt{2\pi\sigma_i^2}} \exp\left[\frac{-(y_i - m_i)^2}{2\sigma_i^2}\right] \tag{3.1}$$

where y_i are the observed data rates, or in our case the rate of the bin i, σ_i their errors, and m_i the values of the predicted data rates based on the model (with current parameters) and instrumental response. Taking twice the negative natural log of L gives the familiar statistics:

$$S^2 = \sum_{i=1}^{N} \frac{(y_i - m_i)^2}{\sigma_i^2} \tag{3.2}$$

commonly referred to as χ^2.

The likelihood for Poisson distributed data is:

$$L = \prod_{i=1}^{N} \left[\frac{\exp(-tm_i)}{S_i!}(-tm_i)^{S_i}\right] \tag{3.3}$$

where S_i are the observed counts, t the exposure time, and m_i the predicted count-rates based on the current model and instrumental response. The maximum likelihood-based statistic for Poisson data is:

$$C = 2\sum_{i=1}^{N} (tm_i) - S_i \ln(tm_i) + \ln(S_i!) \tag{3.4}$$

The final term depends only on the data (and hence makes no difference to the best-fit parameters) so it can be replaced by Stirling's approximation to give :

$$C = 2 \sum_{i=1}^{N} (tm_i) - S_i + S_i(\ln(S_i) - \ln(tm_i)) \qquad (3.5)$$

which provides a statistics which asymptotes to S^2 in the limit of large number of counts.

3.3.1 Models

Since most of our spectra are in a low-counts regime, we chose to fit them with very simple models. In fact, using models with many components in case of low-statistic usually provides best-fit parameters with high errors and not-well constrained fits. We were mainly interested in the obscuration of the sources, so we chose two different simple models. The first one is a power-law model (*powerlaw*), modified by Galactic absorption, with two free parameter: Γ, the photon index of the power law, and K, the power law normalization. The second one is a power-law component with fixed photon index $\Gamma = 1.8$ and an absorption component (*zphabs*) to model the obscuration towards the source, modified by Galactic absorption, again with two free parameters: K, the power law normalization, and N_H, the equivalent hydrogen column of the absorption. The Galactic absorption is the absorption effect caused by the ISM of the Milky Way. It depends on the sky position of the source and was calculated for each source using *Xspec* command `nh` and modeled via a *phabs* component.

We will refer to the first model as **power-law** (PO) and to the second as **absorption** (ABS).

In the ABS model, we decided to fix the photon index because of the degeneracy $\Gamma - N_H$. In fact, if both the parameters were left free to vary, an obscured source could be equally fitted with either flat photon index or with high values of N_H. This degeneracy is even more troublesome in the case of low-statistics, because there are not enough counts to place constraints both on the spectral index and the absorption. Therefore, we decided to fix the photon index to a value of $\Gamma = 1.8$, the average photon index of unobscured AGN being $\Gamma \approx 1.8 - 1.9$ (e.g. Nandra et al. 1994), and to model the obscuration leaving the N_H parameter free to vary.

For all the sources we also tested for the presence of a 6.4 keV Kα iron line with a *zgauss* component and measured its best-fit equivalent width. Moreover, in few cases we also add a Gaussian emission line (*zgauss*) and test its significance with an F-test. In these cases we fixed σ (the line width) to 0.01 keV and left the line normalization as a free parameter. The line energy E_t was either fixed at 6.4, 6.7 or 6.97 keV (which are the Kα line transition associated respectively to neutral, He-like and H-like iron) or left as a free parameter.

3.3.2 Hardness Ratio simulation

For sources with very few counts, or when it is not possible to constrain sufficiently the model parameters, the **Hardness Ratio** (**HR**) helps to obtain some information on the source spectrum. The HR is defined as

$$\text{HR} = \frac{H - S}{H + S} \tag{3.6}$$

where H and S are the hard (2-7 keV observed-frame) and soft (0.5-2 keV observed-frame) net counts.

We used it, alongside simulated spectra, to help us asset the reliability of the best-fit N_H for *lid* 3017 and *cid* 1508, with respectively 15 and 11 net-counts. In fact, we did not succeed in obtaining good fit and acceptable parameter constrain of these sources, likely because of their low number of counts. Our procedure consisted of two parts: first, the creation of simulated spectra and the construction of HR curves as a function of redshift for each value of N_H, then a column density is derived from the source HR.

HR curves

With the aim of building curves of HR as a function of redshift and column density, we created simulated spectra with various redshift and N_H. Measuring the simulated spectra HR, allowed us to obtain the HR curves.

We simulated spectra, via the `fakeit` Xspec routine, using a model with a power-law component with fixed photon index $\Gamma = 1.8$ and an absorption component, modified by Galactic absorption. The simulated spectra had $N_H = (0.01, 0.1, 1, 2.5, 5, 7.5, 10, 100) \cdot 10^{22}$ cm^{-2}, redshift in the range $0.4 < z < 2.0$ with steps of 0.05. The spectra were constructed using the response file of the two sources *lid* 3017 and *cid* 1508. This step was made because different response file led, even for the same source, to different observed spectra and different HR. As a consequence, the curves that linked HR and N_H are, in theory, characteristic of each source, depending on the observation date and on the source position on the detector.

We produced a total of 512 simulated spectra. Measuring the HR of each spectra allowed us to create HR curves as a function of redshift for each value of N_H.

When we constructed the HR curves, we noticed that those obtained with *lid* 3017 response files where not so different from those obtained with *cid* 1508 response files. So we decided to use *lid* 3017's curves for both sources. As further justification of the goodness of our choice, we inspect the ARFs of all the X-ray detected sources (Fig 3.4) and created HR curves with the two most different (*lid* 489 and *lid* 1459). As we can see in Fig 3.5, those were similar in the light of the HR uncertainties (see Fig 3.7). In conclusion, we consider acceptable using the same HR curves for both sources, given the fact that the most different ARF gave similar HR curves.
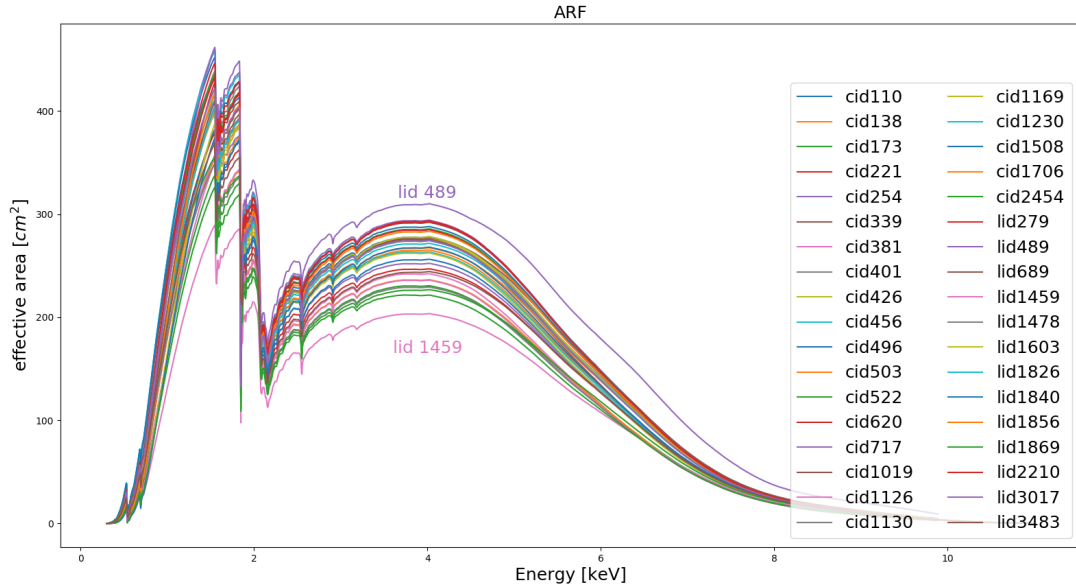
Figure 3.4: Effective area as a function of the photons' energy for each X-ray detected source. These ARFs are those used during X-ray spectral fitting.

We also compared the HR curves obtained with those from Peca 2018, who used them to constrain the redshift for a sample of 30 obscured AGN in the J1030 field. As we can see comparing figures 3.6 and 3.7, our HR curves are quite in agreement with those of Peca.

In Figure 3.7 we show the HR curves obtained and the HR measured values of *lid* 3017 and *cid* 1508.

Absorption estimates

One of the goal is to obtain estimates of *lid* 3017 and *cid* 1508 absorption via the HR curves.

To estimate a source absorption we started choosing the redshift value (between those used in simulated spectra) nearest to the source one. Then, from the HR curves we took the HR values at this redshift and interpolated them, hence obtaining a curve of N_H as a function of the HR. Using this curve and the measured HR of the source, it is easy to obtain an estimate of the source absorption.

For *lid* 3017 at $z = 0.70$, the measured HR$= 0.51 \pm 0.23$ corresponds to $N_H = 8.2^{+32.6}_{-3.1} \cdot 10^{22}$ cm^{-2} (Fig 3.8a). For *cid* 1508 at $z = 0.65$, the measured hardness ratio HR$= -0.14 \pm 0.24$ correspond to $N_H = 1.5^{+1.3}_{-1.7} \cdot 10^{22}$ cm^{-2} (Fig 3.8b).
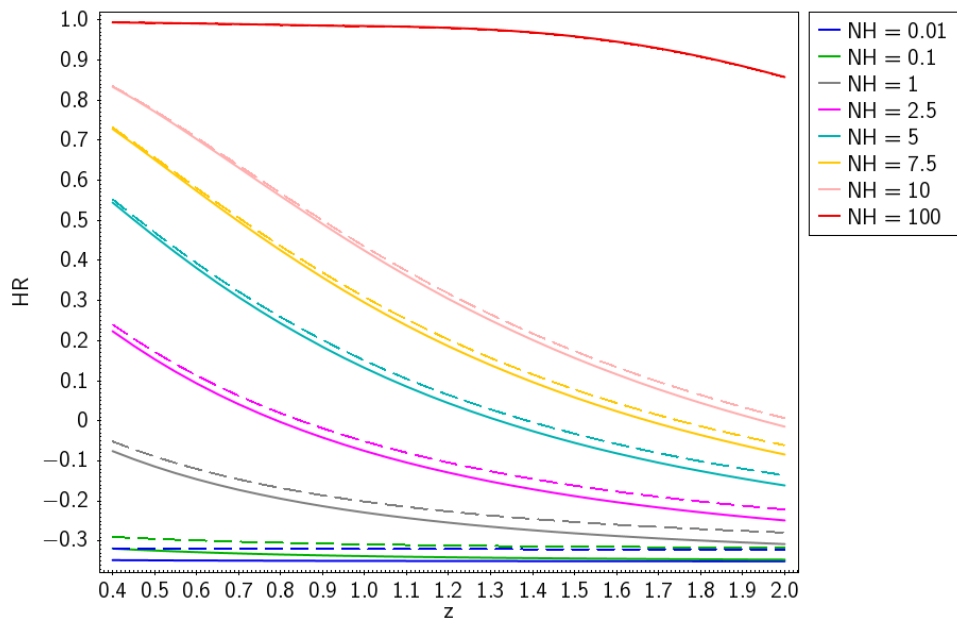
Figure 3.5: Comparison between HR curves obtained from *lid* 489's ARF (continuous lines) and those from *lid* 1459's ARF (dashed lines). N_H values are in units of 10^{22} cm^{-2}. These ARFs are the one showing the largest differences, but the HR obtained from them are quite similar.
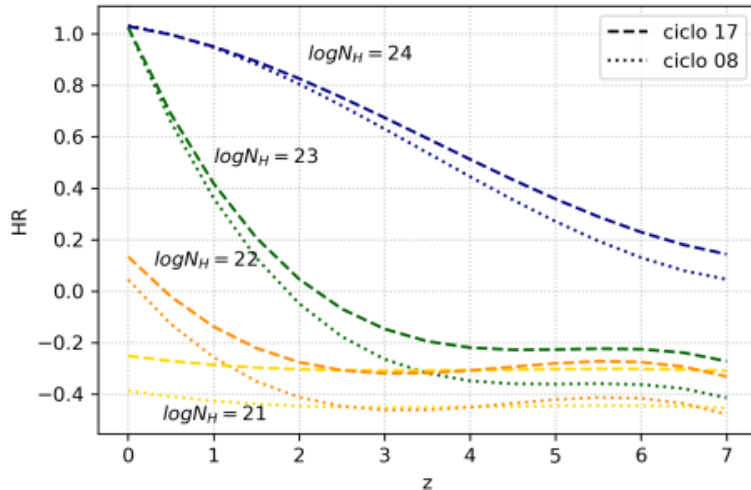
Figure 3.6: Curves of HR obtained by Peca (2018) as a function of redshift for various value of N_H and obtained from two ARFs from different years. The curves were made simulating 10000 spectrum with a power-law, with fixed photon index $\Gamma = 1.9$, and absorption. The HR curves were obtained using response files from *Chandra* cycle 17 (2016-2017) and cycle 08 (2007-2008), as reported in the inset.

In the case of *lid* 3017 the low number of counts led to best-fit parameters in the spectral fit that are poorly constrained. We obtained a $N_H^{\text{Xspec}} = 8.0^{+99.9}_{-5.5} \cdot 10^{22}$ cm^{-2}. The N_H value obtained from HR simulation confirmed the goodness of the spectral fit. For *cid* 1508 we did not even succeed in constraining N_H from the spectral fitting, so the N_H value obtained via HR simulation is the only estimate of the source absorption.

For *lid* 3017 we, also, calculated N_H using HR curves generated by ARF and RMF of *lid* 489 and *lid* 1459, obtaining $N_H^{\text{HR}(lid489)} = 7.7^{+29.5}_{-3.0} \cdot 10^{22}$ cm^{-2} and $N_H^{\text{HR}(lid1459)} = 7.6^{+29.7}_{-3.0} \cdot 10^{22}$ cm^{-2}. The fact that all the N_H values were in agreement is a point in favor of our method.

3.3.3   soft excess

Comparing the sed-fitting results with those from CV+14, we noted (Fig 3.9) that *cid* 1508 and *cid* 138 showed significant differences with the results obtained by CV+14. We will deal with *cid* 138 in section 3.3.4. Studying *cid* 1508 spectrum we noted that it showed a possible presence of a soft excess (Fig 3.10a). We decided to fit the spectra with a partial covering component. We used a model composed of a powerlaw with fixed photon index $\Gamma = 1.8$ and a partial covering fraction absorption *zpcfabs*, modified by Galactic absorption. This model is similar to the ABS model (section 3.3.1), but it takes into account that only fraction f of the power-law emission is effectively absorbed. The
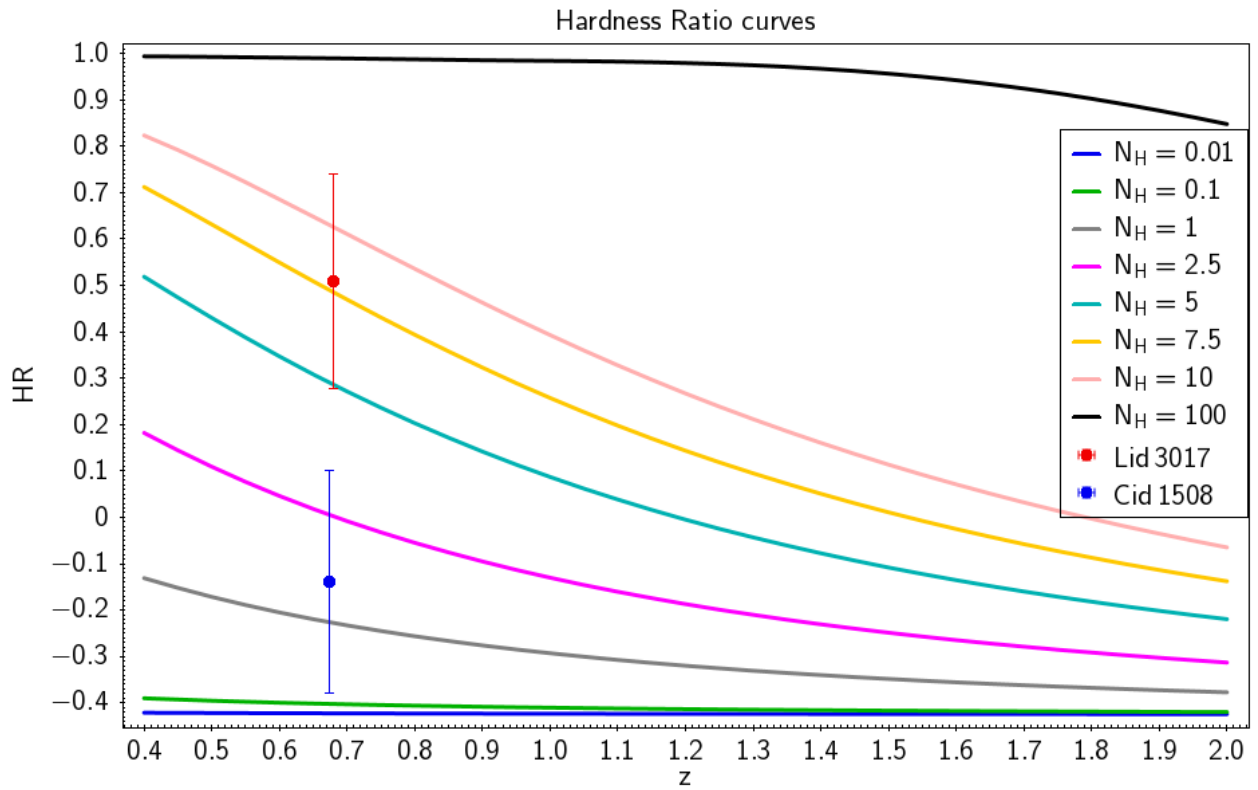
Figure 3.7: HR curves as a function of redshift for various value of N_H, HR values for *lid* 3017 and *cid* 1508 are shown respectively in red and blue with associated 1σ uncertainties; N_H value are in units of 10^{22} cm^{-2}.
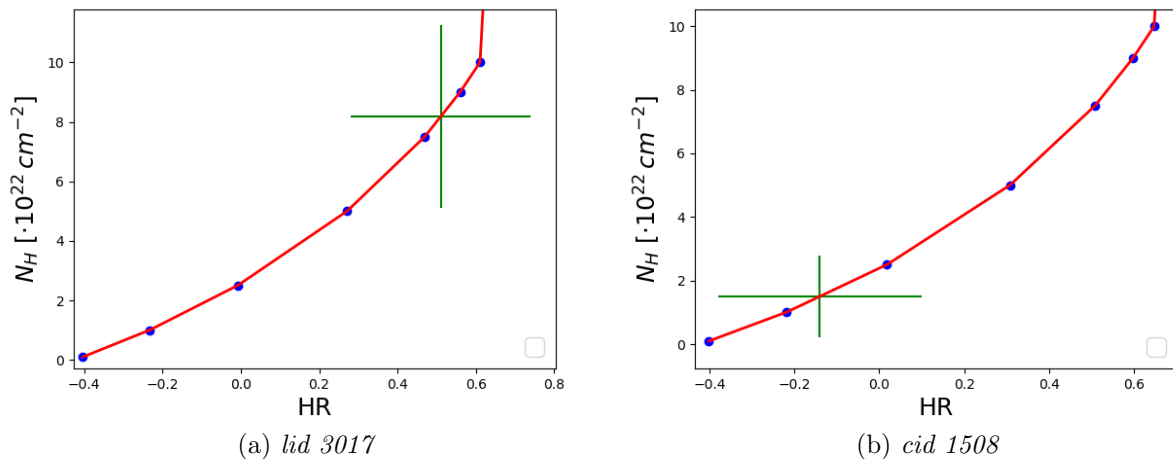
Figure 3.8: (a) Interpolation of the HR vs N_H relation at redshift $z = 0.70$. The green cross shows the HR measured for *lid* 3017, along with its 1σ uncertainties and *lid* 3017 measured HR with 1σ uncertainties. (b) Interpolation of the HR vs N_H relation at redshift $z = 0.65$. The green cross shows the HR measured for *cid* 3017, along with its 1σ uncertainties.

zpcfabs component replaces the *zphabs* and is given by

$$M(E) = f \exp[-N_H \, \sigma(E[1+z])] + 1 - f \qquad (3.7)$$

where $\sigma(E)$ is the photo-electric cross-section, N_H is a free parameter representing the equivalent column density (in units of 10^{22} cm^{-2}) and f is a free parameter called *dimensionless covering fraction* $(0 < f \leq 1)$. With a value of $f = 1$, the model is identical to the ABS, while for $f = 0$ there is no absorption. We will call this model **partial covering (PC)**. We decided to test this model also for *cid* 1019, *cid* 2454, *cid* 1706 because the soft band of their spectra showed a possible additional component with respect to the best-fit model of the hard band.

In Table 3.3 we show the best-fit values of N_H and f from the PC model and a comparison with the best-fit N_H obtained from ABS model. We note that it is difficult to constrain the f parameter, as in all the four source, considering the errors, it is compatible with a value of 1.

HR simulation

As in Section 3.3.2, we used HR simulations to help us asserting the reliability of the best-fit values. The simulated spectra were created using a power-law with fixed photon index $\Gamma = 1.8$ and *zpcfabs* component with $N_H = (0.01, 0.1, 1, 2.5, 5, 7.5, 10, 100) \cdot$
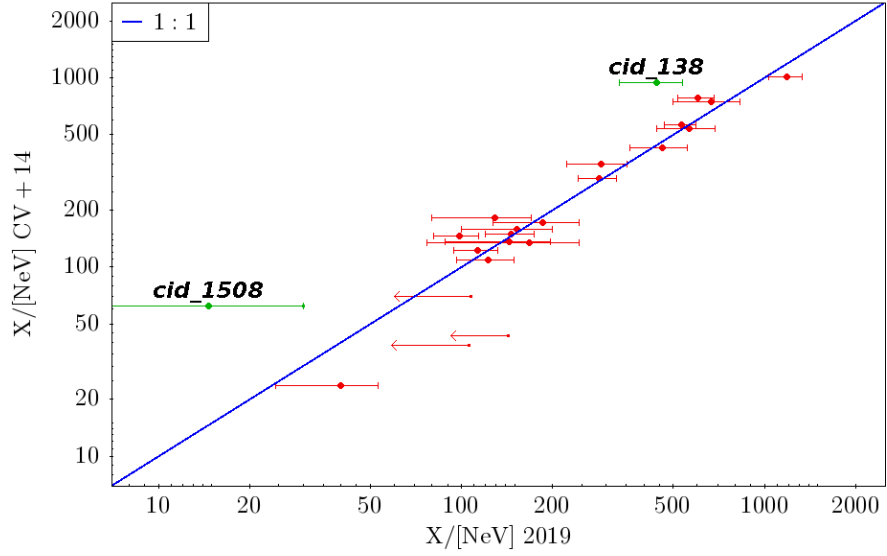
Figure 3.9: X/[NeV] ratio comparison between our results and those from CV+14 for 23 [Ne V] selected type 2 AGN detected both in C-COSMOS and COSMOS Legacy. Green points are *cid* 1508 and *cid* 138 that show significant differences with respect to CV+14.
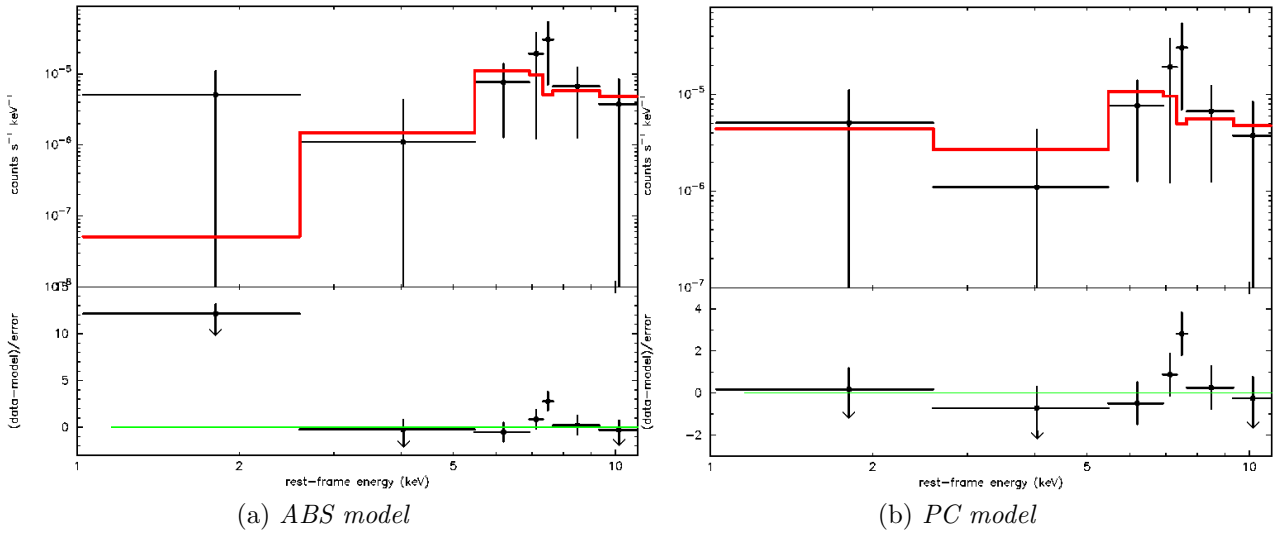

(a) *ABS model*

(b) *PC model*

Figure 3.10: *cid* 1508 folded spectrum (i.e. not corrected for the instrumental response), rebinned for display purpose, and residual. The first data point displays a possible soft excess. Spectrum fitted with: (a) ABS model, (b) PC model ($\Gamma = 1.8$, $N_H = 93^{+257}_{-86} \cdot 10^{22}$ cm^{-2}, $1 - f < 0.23$) to take into account the soft excess. The PC model provided a better fit to the soft band.

ID	N_H^{ABS} $\cdot 10^{22}[cm^{-2}]$	N_H^{PC} $\cdot 10^{22}[cm^{-2}]$	f
$cid\,1508$	86^{+203}_{-77}	93^{+257}_{-86}	$0.99^{+0.01}_{-0.22}$
$cid\,1019$	144^{+172}_{-105}	157^{+173}_{-126}	$0.997^{+0.002}_{-0.011}$
$cid\,2454$	18^{+79}_{-16}	22^{+48}_{-16}	$0.95^{+0.05}_{-0.16}$
$cid\,1706$	111^{+105}_{-70}	104^{+154}_{-79}	> 0.92

Table 3.3: Comparison of best-fit parameters between ABS and PC models for sources with a possible soft excess. N_H^{ABS}: absorbing column density at source redshift from *zphabs* model; N_H^{PC}: absorbing column density at the source redshift from *zpcfabs* model; f: fraction of coverage, i.e. fraction of the emission that can be absorbed at the source redshift, from *zpcfabs* model. All the sources have practically only lower limit on their fraction of coverage, as f is always compatible with a values of 1, hence it is not a well constrained parameter.

10^{22} cm^{-2}, redshift in the range $0.4 < z < 2.0$ with steps of 0.05 and $1 - f = (0, 0.1, 0.5, 1, 2, 5, 10, 100)$ %. We chose the redshift closest to the source measured one and, for each value of f, we created interpolation curves of N_H as a function of the HR. Using the HR measured ($HR_{cid\,2454} = 0.60 \pm 0.16$, $HR_{cid\,1019} = 0.75 \pm 0.14$, $HR_{cid\,1706} = 0.99^{+0.01}_{-0.13}$, $HR_{cid\,1508} = -0.14 \pm 0.24$) we obtained an estimate of the N_H for each source for different values of the covering fraction f (Table 3.4). Because there is a degeneracy regarding HR, N_H and f parameters, we cannot find a unique value of N_H. For example: low values of HR can be explained both with little absorption and an high covering factor or with high absorption and low covering factor. Therefore, although we could not rely only on the HR simulation to find the source absorptions, we used these results as comparison with the N_H values obtained from spectral fitting to help us asset the reliability of the fit results.

Results

For sources $cid\,1019$, $cid\,2454$, $cid\,1706$, the PC best-fit values were not significantly different from those obtained with ABS model. Therefore, we continued to use the simpler ABS model. For source cid 1508 the N_H values were similar between the two models. From Figure 3.10b, it is evident that, with the PC models, we had a better fit in the soft band. Moreover, the 2-10 keV rest-frame flux and, consequently, the X/[NeV] ratio, obtained from PC model, were closer to the value obtained by CV+14, as we can see in Table 3.5. Therefore, we chose to use the best-fit values obtained from PC model for the source cid 1508.

	ID	0%	0.1%	1%	5%	10%
				$1-f$		
$N_H \,[\cdot 10^{22}\,cm^{-2}]$	$cid\ 2454$	$15.9^{+34.5}_{-8.2}$	$17.5^{+38.8}_{-9.8}$	$80.8^{+19.2}_{-72.7}$	-	-
	$cid\ 1019$	$48.4^{+30.2}_{-30.1}$	$53.9^{+33.8}_{-33.7}$	> 92.0	-	-
	$cid\ 1706$	> 72.5	> 80.8	-	-	-
	$cid\ 1508$	$1.5^{+1.6}_{-1.2}$	$1.5^{+1.6}_{-1.2}$	$1.5^{+1.7}_{-1.3}$	$1.7^{+98.0}_{-1.4}$	$70.0^{+29.9}_{-69.7}$

Table 3.4: Column density for the four sources ($cid\,2454$, $cid\,1019$, $cid\,1706$ and $cid\,1508$) for which we tested for the presence of soft excess via a partial covering model. N_H values were obtained from HR and simulated spectra with PC model, for different values of $1-f$, where f is the dimensionless covering fraction of the *zpcfabs* component.

	$F^{ABS}_{2-10keV,rest}$ $\cdot 10^{-14}$ $erg/cm^2/s$	$X^{ABS}/[NeV]$	$F^{PC}_{2-10keV,rest}$ $\cdot 10^{-14}$ $erg/cm^2/s$	$X^{PC}/[NeV]$
2019	0.04 ± 0.04	$14.7^{+15.5}_{-14.7}$	$0.12^{+0.07}_{-0.12}$	$45.9^{+43.4}_{-45.9}$
CV+14	0.14	62.2	0.14	62.2

Table 3.5: Comparison of 2-10 keV flux and X/[NeV] ratio between ABS model, PC model and CV+14 for source $cid\,1508$. $F_{2-10keV,rest}$: $2-10$ keV rest-frame flux (not corrected for the absorption); $X/[NeV]$: X/[NeV] ratio. The PC model, used to take into account the soft excess, provided values closer to those from CV+14.

3.3.4 "Peculiar" sources

We will now present a detailed analysis of four sources, which showed peculiar spectral feature: *cid* 339, *lid* 1840, *lid* 279 and *cid* 138. In case of *cid* 339, *lid* 1840 and *lid* 279, we tested for the presence of emission lines, either because of the spectral shape or because it was previously detected in "CV+14". *cid* 138, instead, was investigated because the spectral analysis provided results very different from to those of "CV+14".

cid 339

cid 339 has 380 net counts; its spectrum has been rebinned to have at least 15 counts per bin. The PO model best-fit provided a photon index of $\Gamma = 1.50^{+0.18}_{-0.17}$, while the ABS model gave $N_H = 0.6^{+0.4}_{-0.3} \cdot 10^{22}$ cm^{-2} (Figure 3.11). In CV+14 an emission line at 6.97 keV rest-frame was detected with a significance of $\approx 2.5\sigma$. We added to the ABS model an emission line with fixed energy at 6.97 keV, fixed width=0.01 keV and tested for its significance. However, in our case, adding the 6.97 keV line worsen the fit. The N_H obtained in CV+14 was $N_H = 0.38^{+0.32}_{-0.28} \cdot 10^{22}$ cm^{-2}, compatible with our value.
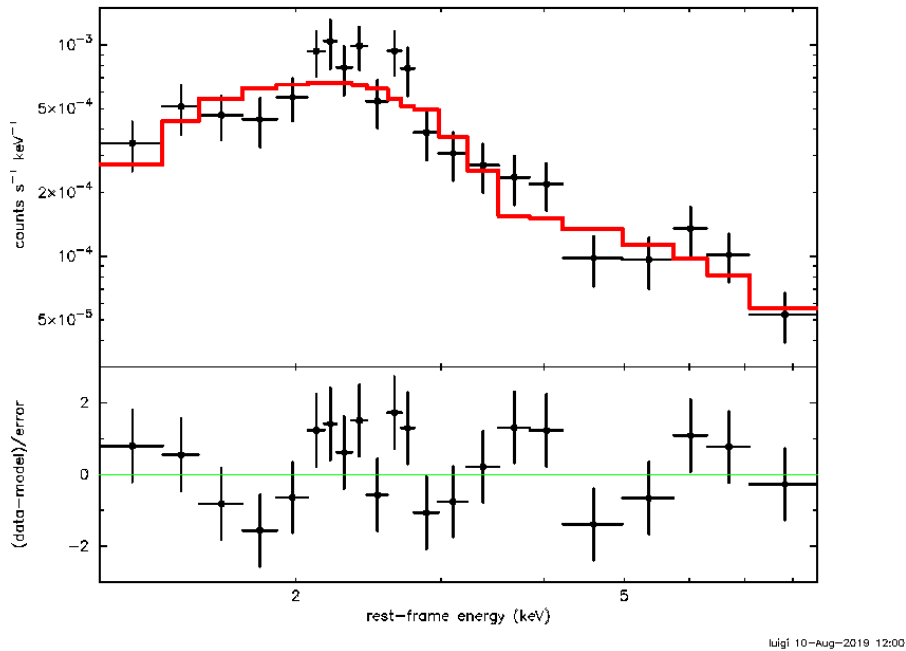

Figure 3.11: *cid* 339 folded spectra and residuals. The spectrum was rebinned to have at least 15 counts per bin and fitted with the ABS model. In "CV+14" an emission line at energy 6.97 keV (rest-frame) was reported with a $\approx 2.5\sigma$ significance; however, in our case, adding the line component to the model worsens the fit.

lid 1840

The source *lid* 1840 has been rebinned to have at least 15 counts per bin, having a total of 238 net-counts. The PO model best-fit provided a photon index of $\Gamma = 1.98^{+0.35}_{-0.32}$, while the ABS model gave an upper limit of $N_H < 0.5 \cdot 10^{22} cm^{-2}$. We found the possible presence of a 6.97 keV line with a significance of $\approx 2.6\,\sigma$ and an equivalent width of $EW_{6.9keV} = 1.54^{+1.46}_{-1.06}$ keV (Figure 3.12). We tested also for the presence of a 6.4 keV line, but its significance resulted only of $\approx 1.6\,\sigma$.
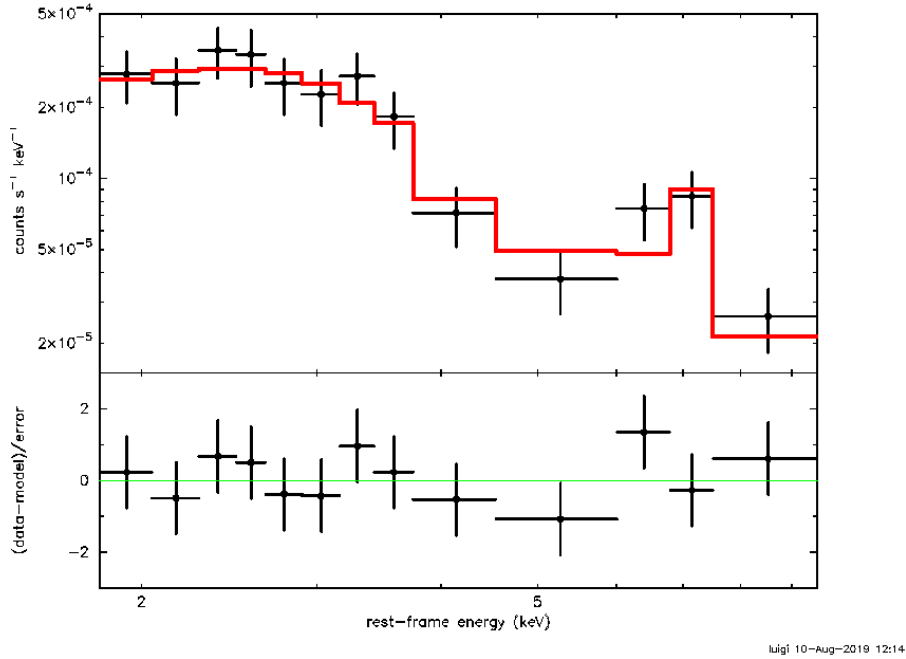

Figure 3.12: *lid* 1840 folded spectra and residuals. The spectrum was rebinned to have at least 15 counts per bin and modeled with a power-law model with a 6.97 keV emission line. The line significance was $\approx 2.6\,\sigma$. We tested also for the presence of 6.4 keV emission line and detected it with a $\approx 1.6\,\sigma$ significance.

To further check for the presence of the line, we rebinned to one count per bin, hence ensuring that the line was not caused by the binning used, and performed spectral fitting using the Cash statistic. We used a PO model with an emission line, leaving the line energy as a free parameter. The model provided the line at $E_{line} = 7.13^{+0.35}_{-0.27}$ keV, compatible at 90% with an energy of 6.97 keV (Fig 3.13). Although the fit procedure found other minima at ≈ 6.4 keV and ≈ 8.5 keV, those were local minima and the 7.1 keV minimum appeared to be the most significant.
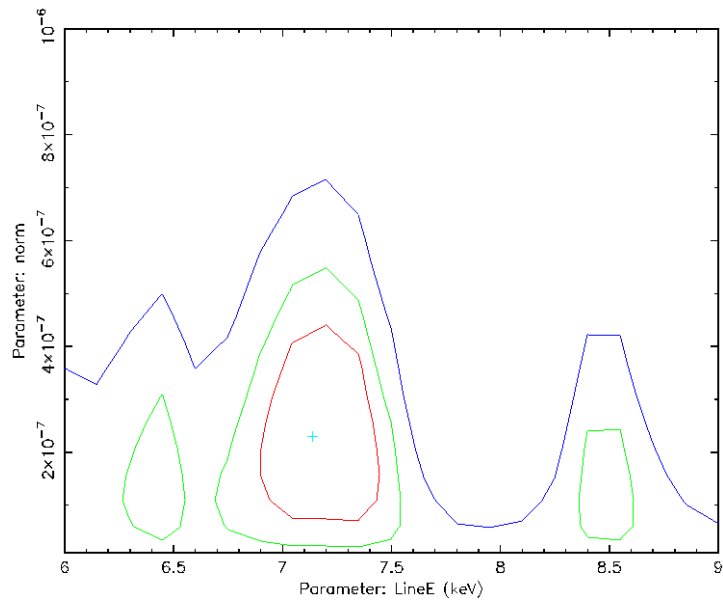
Figure 3.13: Contour plot line normalization vs line energy for *lid* 1840. The spectra was unbinned and modeled with a power-law model with an emission line. The contour confidence levels are 68% (blue), 90% (green) and 99% (red). The most significant minimum (at $\approx$ 7.1 keV) is compatible with the 6.97 keV emission line found, with a confidence of $\approx 2.6\sigma$, analyzing the binned spectrum (Fig 3.12).

lid 279

With 183 net-counts, _lid_ 279 spectrum was rebinned to have at least 10 counts per bin. The PO model best-fit provided a photon index of $\Gamma = 1.88^{+0.36}_{-0.32}$, while the ABS gave an upper limit of $N_H < 0.5 \cdot 10^{22} \text{cm}^{-2}$ (Fig 3.14). We found the possible presence, although at low confidence level, of emission lines at 6.4 keV ($\approx 1.2\sigma$) and 6.97 keV ($\approx 1.3\sigma$). Only loose constraints (of a few keV) on their equivalent width were obtained.
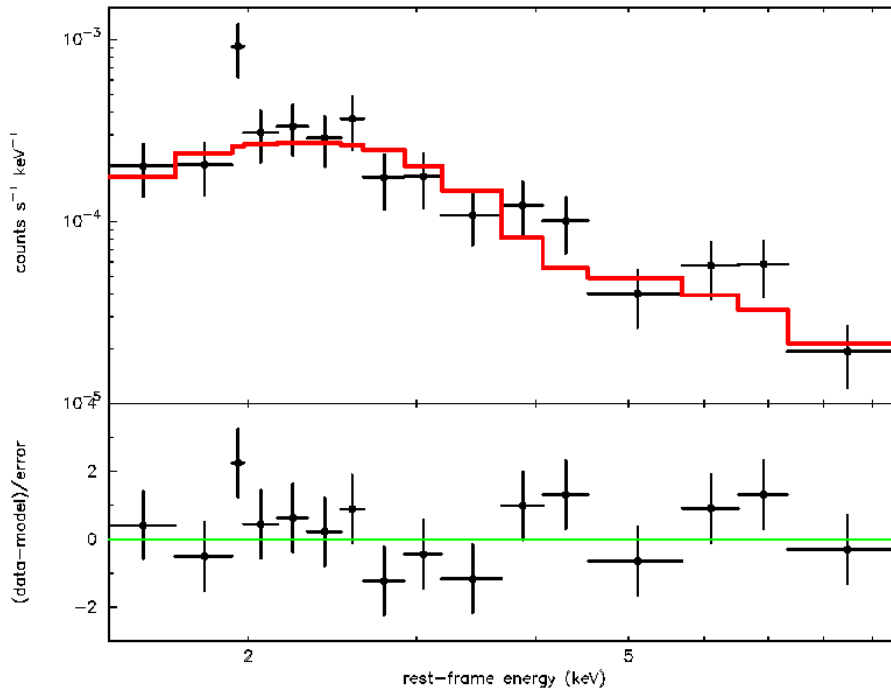

Figure 3.14: Folded spectrum and residuals of source _lid_ 279. It was binned to have at least 10 counts per bin and modeled with a power-law model. 6.4 keV and 6.97 keV emission lines were tentatively detected, at a confidence of $\approx 1.2\sigma$ and $\approx 1.3\sigma$ respectively.

cid 138

The source _cid_ 138 has 99 net counts, we chose to rebin its spectrum to have at least 10 counts per bin. The PO model best-fit provided a photon index of $\Gamma = 1.37^{+0.43}_{-0.39}$, while the ABS gave $N_H = 1.8^{+1.8}_{-1.6} \cdot 10^{22} \text{cm}^{-2}$. Comparing the $2 - 10$ keV rest-frame flux, and consequently the X/[NeV] ratio, obtained from the best-fit with those from CV+14, we noticed significant differences (Figs 3.15 and 3.9). In particular, our flux and the "CV+14" one differ by 4.8 times its error. The $2 - 10$ keV flux from "CV+14" was provided without an associated error.
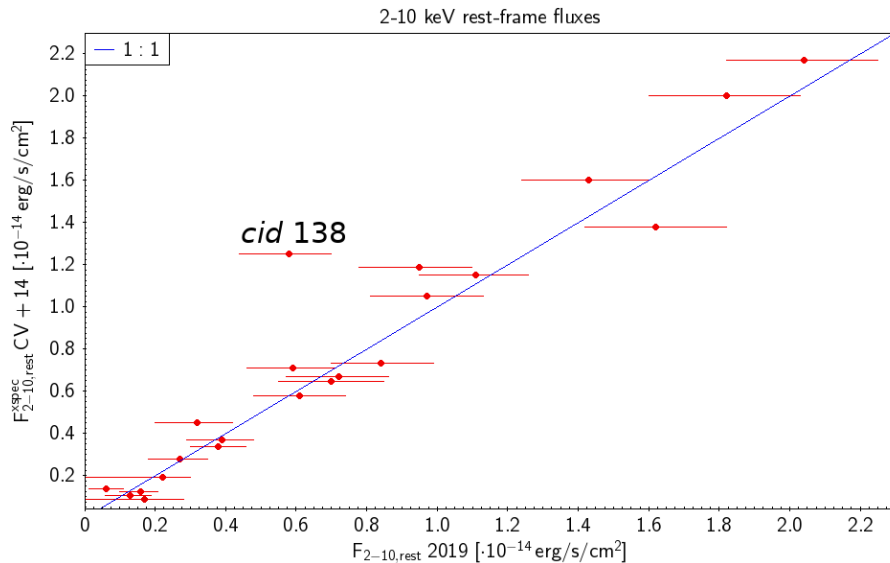
Figure 3.15: Comparison of $2-10$ keV rest-frame flux (not corrected for the absorption) between our values and those obtained from CV+14. Source *cid* 138 flux differs by 4.8 times its error from the "CV+14" value.

Unlike *cid* 1508, we did not notice any sign for a possible soft excess (Fig 3.16). *cid* 138 data came from 3 observations (7997, 8122 and 8494), carried out in 2007 within the C-COSMOS survey, and from 6 observations (15208, 15209, 15210, 15598, 15600 and 15604), carried out in 2014 within the COSMOS Legacy survey. We decided to analyze each observation separately, searching for possible differences (in exposure time, spectral index, absorption, HR, count-rate) between them. In Table 3.6 we report the exposure time, the net (background-subtracted) counts and total, soft and hard net count-rates of each observation.

In Fig 3.17a we show that there is a significant difference in count-rate between 2007 and 2014 observations. This is even sharper when we combined the 2007 and 2014 data into two separate spectra (Fig 3.17b). We used the *CIAO* tool `combine_spectra` to group the data into two sets: the 2007 and 2014, similarly to the way a single spectra was obtained from all the observation of a source (section 3.2). The `combine_spectra` script sums multiple spectra and, also, combines the associated background spectra and source and background ARF and RMF response files.

We both calculated the HR of the two data sets and performed spectral analysis of their spectra, looking for differences between the two sample. In Table 3.7 we report the main results. As we can see, there were no significant differences in photon index, obscuration or HR. However, the net count-rate varied by more than a factor of 6, with a significance of 6.7σ.

We plotted the ARF of each observations to check if this count-rate variability was
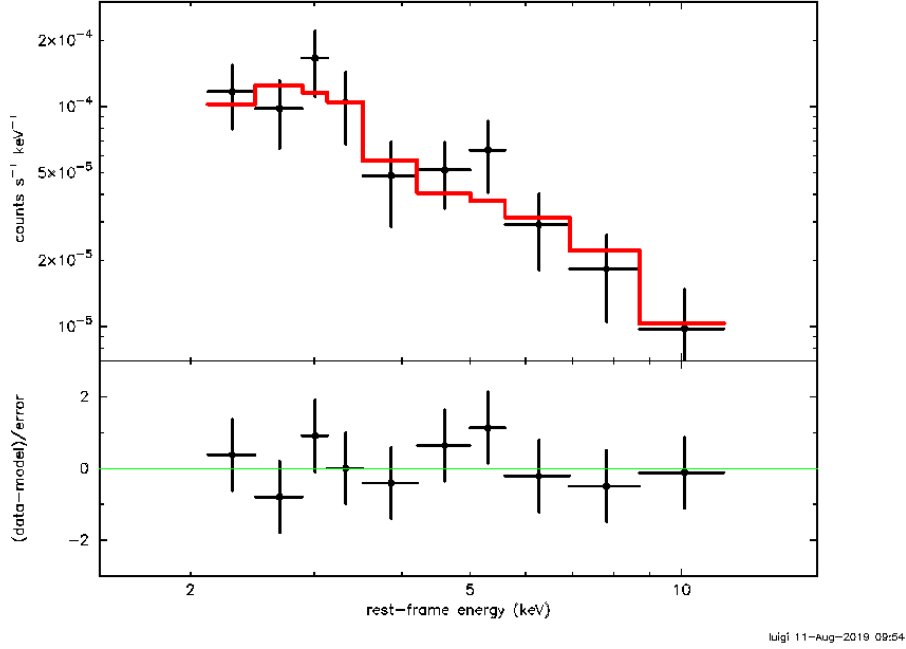
Figure 3.16: Folded spectra and residual of *cid* 138. Its spectrum has been rebinned to have at least 10 counts per bin and fitted with the ABS model. There is no evident hint of soft excess.

Oss	T_{exp} [ks]	Net count	$Nctr_{0.5-7\text{ keV}}$ $\cdot 10^{-4}\,[\text{s}^{-1}]$	$Nctr_{0.5-2\text{ keV}}$ $\cdot 10^{-4}\,[\text{s}^{-1}]$	$Nctr_{2-7\text{ keV}}$ $\cdot 10^{-4}\,[\text{s}^{-1}]$
7997	45.4	42 ± 6	9.20 ± 1.43	4.58 ± 1.01	4.40 ± 0.98
8122	28.8	21 ± 5	7.24 ± 1.72	4.11 ± 1.26	3.13 ± 1.17
8494	20.8	18 ± 4	8.50 ± 2.11	3.21 ± 1.28	5.29 ± 1.68
15208	23.0	4 ± 2	1.68 ± 1.10	0.29 ± 0.45	1.39 ± 1.00
15209	23.8	3 ± 2	1.13 ± 0.73	0.38 ± 0.42	0.76 ± 0.60
15210	23.8	1 ± 1	0.07 ± 0.76	< 0.10	0.20 ± 0.76
15598	22.2	6 ± 2	2.70 ± 1.10	0.45 ± 0.45	2.25 ± 1.01
15600	21.8	5 ± 2	2.20 ± 1.03	2.25 ± 1.03	< 0.05
15604	21.8	4 ± 2	1.84 ± 1.50	1.20 ± 0.98	0.64 ± 1.13

Table 3.6: *cid* 138's observations exposure time, net-counts, 0.5-7 keV net count-rate, soft (0.5-2 keV) net count-rate and hard (2-7 keV) net count-rate.
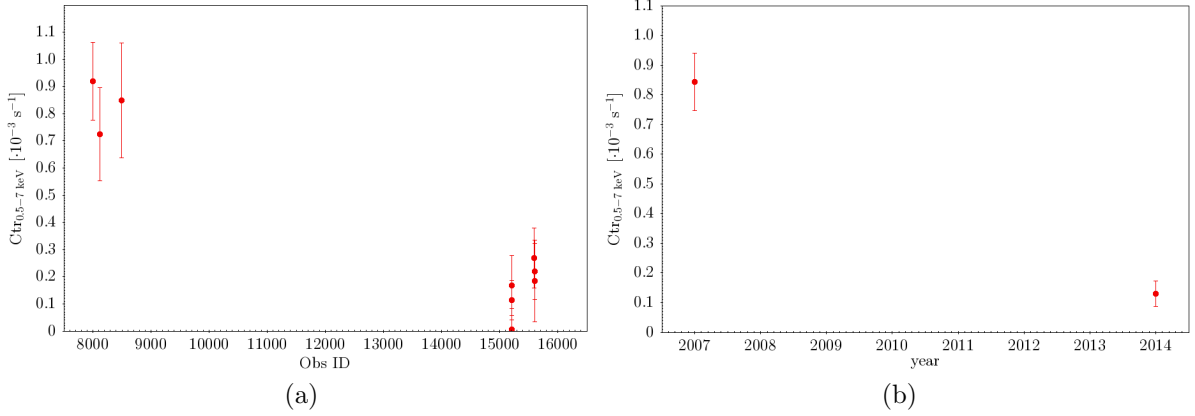
Figure 3.17: $0.5 - 7$ keV count-rate variation of source *cid* 138. a) count-rate of each *cid* 138 observation as a function of their observation ID; b) count-rate of 2007 and 2014 data. 2007 and 2014 data were obtained merging the *cid* 138 observations, on the basis of the year in which they were performed, via the *CIAO* tool `combine_spectra`. Between 2007 and 2014 count-rates there is a 6.7σ variation.

year	T_{exp} ks	$Nctr_{0.5-7 \text{ keV}}$ $\cdot 10^{-4}\,s^{-1}$	HR	Γ (PO)	N_H (ABS) $\cdot 10^{22}\,cm^{-2}$
2009	95.01	8.43 ± 0.97	0.01 ± 0.11	1.00 ± 0.33	$2.1^{+1.1}_{-0.9}$
2016	136.00	1.30 ± 0.42	0.06 ± 0.26	$1.34^{+1.10}_{-0.89}$	< 5.5

Table 3.7: Main results of the spectral analysis of *cid* 138's 2007 and 2014 data. Exposure time, 0.5-7 keV net count-rate, hardness ratio, photon index (PO model) and column density (ABS model). Except for the net count-rate, there is no significant variation between the two sets of data. The count-rate shows a 6.7σ variation.

58

due to a variation of the effective area (Fig 3.18), but we found no variation capable of explaining the observed differences of the count-rate. In fact, a lower effective area can lead to a minor number of photon detected; however, there are 2014 observations with higher effective area with respect to those of the 2007. Moreover, the `combine_spectra` tool takes into account the different ARFs when combining the spectra; hence, ARF variation should not have an effect on the measured count-rate. Therefore, we concluded that the count-rate, and flux, variabilities could be ascribed to a variability of *cid* 138. This variability could be linked to a difference in the number of torus clouds intercepted (in the "clumpy torus" model) or to a variation of the AGN accretion rate. However, if the number of obscuring clouds changed we would expect a variation both on the flux and on the spectra shape (i.e. column density or HR). Therefore, we deduced that *cid* 138 flux variability is probably associated to a variation of the AGN accretion rate.
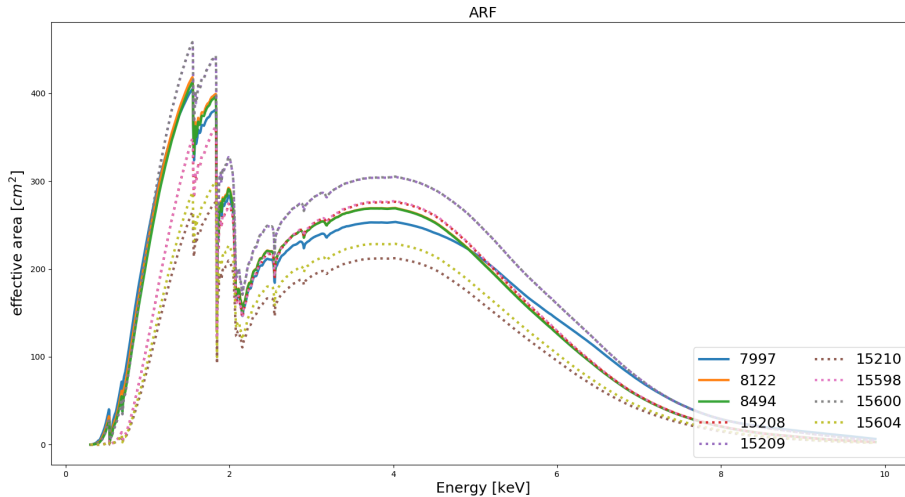

Figure 3.18: Effective area as a function of energy for *cid* 138 observations. Solid lines are ARFs of 2007 observations, while dashed lines are those of 2014 observations.

3.3.5 Results

In Table 3.8 we show the results of the X-ray spectral fitting for the 36 sources with X-ray detection. For all the sources we obtained the best-fit photon index, using the PO model, and the absorption column density, using the ABS model.

The mean photon index is $\Gamma\,(\text{PO}) = 0.83$ with a standard deviation of 0.89. We note that this value is far from $\Gamma \approx 1.6 - 1.9$ typical of unobscured AGN (e.g. Nandra et al. 1994, Piconcelli et al. 2005). For this reason, we fixed the photon index to a value of

$\Gamma = 1.8$ and modeled the obscuration with an absorption component in the ABS model. Ten sources, out of 36, have only an upper limit on their N_H, the other 26 sources have a mean column density (calculated with fixes $\Gamma = 1.8$, as mentioned in Section 3.3.1) of $N_H (ABS) = 20.8 \cdot 10^{22} \, cm^{-2}$, with a standard deviation of $35.9 \cdot 10^{22} \, cm^{-2}$.

The high-count sample has mean $\Gamma (PO) = 1.29 \pm 0.52$. Excluding the five upper limits on the absorption, the high-count sample has a mean $N_H (ABS) = 7.5 \cdot 10^{22} cm^{-2}$ and a standard deviation of $8.5 \cdot 10^{22} cm^{-2}$.

The low-count sample has mean $\Gamma (PO) = 0.42 \pm 0.96$ and five upper limits on the N_H value. When not considering them, the mean absorption is $N_H (ABS) = 32.2 \cdot 10^{22} cm^{-2}$ with a standard deviation of $45.2 \cdot 10^{22} cm^{-2}$. The low-count sample has, on average, flatter photon index and higher value of column density. We interpreted this as consequence of higher obscuration of these sources, that lead to fewer photons escaping the source and reaching us.

Except for three sources, we have only upper limits on the 6.4 keV Kα equivalent width.

N_H

Eight sources (*cid* 717, *lid* 689, *lid* 1856, *cid* 339, *cid* 110, *lid* 1840, *lid* 279 and *cid* 1130) show $N_H < 10^{22} \, cm^{-2}$, for seven of them we obtained only an upper limit. If we add the four other sources with an upper limit on their N_H (*cid* 1230, *cid* 221, *lid* 489 and *lid* 1603), we have twelve sources with very low value of obscuration. Unsurprisingly these sources are those with the highest value of photon index in the PO model. This was expected, because the steep photon indices suggested a low-obscured or unobscured nature of these sources. Two sources can be classified as CT on the basis of a $N_H > 10^{24}$ cm^{-2}, 9 should be highly obscured sources with $N_H > 10^{23} \, cm^{-2}$. In Fig 3.19 we show the distribution of the N_H best-fit values.

0.5-10 keV observed-frame flux

We computed the 0.5 - 10 keV observed-frame flux of all sources for both the PO and ABS model. As we can see in Fig 3.20a, the two models produce compatible flux values. From now on, we will use only fluxes and luminosities computed with ABS models.

For four sources we were able to obtain only an upper limit on the flux; these upper limit sources belong to the low-count sample. Our sample, considering the upper limits, has a mean 0.5-10 keV of $1.66 \cdot 10^{-14}$ erg/s/cm^2, the high-count sample of $2.80 \cdot 10^{-14}$ erg/s/cm^2 and the low-count sample of $0.63 \cdot 10^{-14}$ erg/s/cm^2. Without the upper limits we obtain a mean of $1.78 \cdot 10^{-14}$ erg/s/cm^2. We compared these fluxes with those from "cat16", obtained with a power-law model with a photon index of $\Gamma = 1.6$ (Civano et al. 2016). Within errors, we did not find significant differences (Fig 3.20b).

ID	z	Ncts	Γ (PO)	N_H (ABS) $\cdot 10^{22} \mathrm{cm}^{-2}$	$EW_{6.4\mathrm{keV}}$ (ABS) keV
lid 1856	0.7348	1827	$1.60^{+0.07}_{-0.07}$	$0.4^{+0.2}_{-0.2}$	< 0.21
cid 339	0.6865	373	$1.50^{+0.18}_{-0.17}$	$0.5^{+0.4}_{-0.3}$	< 0.86
cid 522	0.9444	336	$1.08^{+0.18}_{-0.18}$	$3.5^{+1.1}_{-1.0}$	< 0.3
cid 110	0.7295	313	$1.65^{+0.21}_{-0.20}$	< 0.5	< 0.7
cid 173	0.9997	242	$1.55^{+0.26}_{-0.25}$	$1.1^{+1.2}_{-1.0}$	< 0.7
lid 1840	1.0062	216	$1.98^{+0.35}_{-0.32}$	< 0.5	$0.76^{+0.96}_{-0.74}$
cid 381	0.8649	208	$0.90^{+0.24}_{-0.26}$	$6.1^{+2.9}_{-2.3}$	< 0.8
lid 279	0.8819	173	$1.88^{+0.36}_{-0.32}$	< 0.5	< 2.3
lid 1478	0.8326	168	$1.03^{+0.32}_{-0.31}$	$3.8^{+2.2}_{-1.8}$	$0.73^{+0.84}_{-0.68}$
cid 496	0.8993	165	$1.52^{+0.29}_{-0.27}$	$1.3^{+1.4}_{-1.2}$	< 1.5
cid 456	1.023	162	$0.18^{+0.34}_{-0.36}$	$21.5^{+15.2}_{-8.0}$	< 0.7
cid 221	0.7488	142	$1.80^{+0.29}_{-0.27}$	< 1.1	
cid 620	1.1767	126	$0.74^{+0.44}_{-0.45}$	$25.9^{+14.6}_{-11.0}$	$0.52^{+0.54}_{-0.50}$
lid 1826	1.1733	109	$1.16^{+0.35}_{-0.34}$	$7.4^{+4.4}_{-3.7}$	< 1.1
cid 138	0.7034	99	$1.37^{+0.43}_{-0.39}$	$1.8^{+1.8}_{-1.6}$	< 1.4
cid 1126	0.9588	93	$0.24^{+0.51}_{-0.56}$	$17.0^{+10.3}_{-6.8}$	< 0.7
lid 489	0.8499	93	$1.69^{+0.53}_{-0.49}$	< 1.4	< 1.4
cid 717	0.8913	85	$1.51^{+0.35}_{-0.33}$	< 0.7	< 2.2
cid 503	0.9106	80	$0.26^{+0.36}_{-0.37}$	$5.9^{+3.1}_{-2.2}$	
cid 426	0.8643	75	$0.49^{+0.36}_{-0.36}$	$4.8^{+2.0}_{-1.3}$	< 1.2
cid 254	0.7106	60	$1.19^{+0.40}_{-0.38}$	$1.2^{+1.0}_{-0.8}$	< 1.7
lid 689	0.6752	59	$2.06^{+0.44}_{-0.42}$	< 0.4	
lid 3483	0.6606	51	$-0.43^{+0.53}_{-0.58}$	$22.0^{+15.0}_{-8.8}$	
cid 1130	0.7864	48	$1.38^{+0.53}_{-0.50}$	< 0.8	
cid 1019	0.7302	41	$-0.99^{+1.93}_{-1.73}$	144^{+172}_{-105}	
cid 401	0.9707	39	$-0.44^{+0.56}_{-0.63}$	$20.0^{+17.0}_{-7.9}$	< 1.1
lid 1603	0.9653	39	$1.15^{+0.55}_{-0.54}$	< 4.7	< 1.6
lid 1869	1.1684	36	$0.31^{+0.59}_{-0.61}$	$9.4^{+7.4}_{-5.0}$	< 2.4
cid 1230	0.7535	35	$1.39^{+0.61}_{-0.60}$	< 1.0	
cid 1169	0.9591	21	$0.87^{+0.89}_{-0.84}$	$3.9^{+5.7}_{-3.5}$	
lid 2210	0.7353	18	$0.75^{+0.82}_{-0.87}$	$3.9^{+3.6}_{-2.3}$	
lid 1459	1.0001	17	$1.04^{+1.00}_{-0.99}$	$5.9^{+10.8}_{-2.9}$	
cid 1706	0.7642	15	$-1.60^{+1.30}_{-1.00}$	111^{+105}_{-70}	
cid 2454	0.764	15	$-0.05^{+2.20}_{-2.10}$	18^{+79}_{-16}	
lid 3017	0.6793	15	$-0.09^{+0.94}_{-1.16}$	8^{+100}_{-6}	
cid 1508	0.6743	11	$-0.89^{+1.47}_{-0.92}$	93^{+257}_{-86}	

Table 3.8: Main results of the spectral analysis for the 36 X-ray detected sources. Ncts: number of background-subtracted counts Γ (PO): best-fit photon index obtained from the PO power-law model; N_H (ABS): best-fit absorption column density obtained from the ABS model (power-law with fixed $\Gamma = 1.8$ and absorption component to model the source obscuration); $EW_{6.4\mathrm{keV}}$ (ABS): best-fit equivalent width of the 6.4 keV (rest-frame) emission line obtained with the ABS model and a *zgauss* component with line width fixed at 0.01 keV.
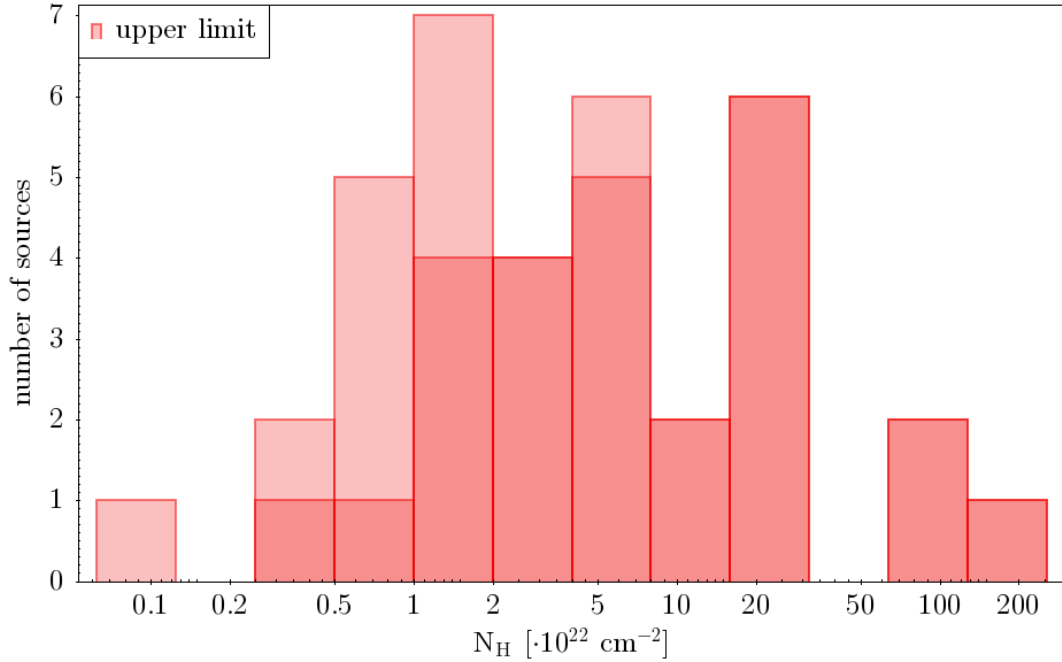
Figure 3.19: Distribution of N_H best-fit values of the 36 X-ray detected sources. In light red the 9 sources with only upper limits on the N_H.

2-10 keV rest-frame flux

We computed the 2-10 keV rest-frame flux (not corrected for the obscuration) of our sample. The mean flux is $0.92 \cdot 10^{-14}$ erg/s/cm^2. We compared the fluxes with those from "CV+14" (Fig 3.21), which were obtained via an *Xspec* spectral fitting with a powerlaw model with $\Gamma = 1.4$. Except for *cid* 138, as previously discussed in section 3.3.4, the values are in agreement. We obtained a 2019 to "CV+14" mean ratio of 1.04, with a standard deviation of 0.34.

Four sources lack detection in the 2-10 keV rest-frame band, hence we were able to obtain only upper limit on the flux in this band, all of them belongs to the low-count sample. Without considering them, the mean flux becomes $1.02 \cdot 10^{-14}$ erg/s/cm^2. The fact that we were able to obtain only an upper limit is due to the few net-counts of these sources.

2-10 keV rest-frame intrinsic luminosity

We computed the 2-10 keV rest-frame intrinsic luminosity of our sample, using the power-law normalization obtained from ABS model, photon index fixed at $\Gamma = 1.8$, and imposing a column density $N_H = 0$. The sample has a mean luminosity of $5.4 \cdot 10^{43}$ erg/s with a standard deviation of $5.7 \cdot 10^{43}$ erg/s, the high-count sample of $8.3 \cdot 10^{43}$ erg/s and
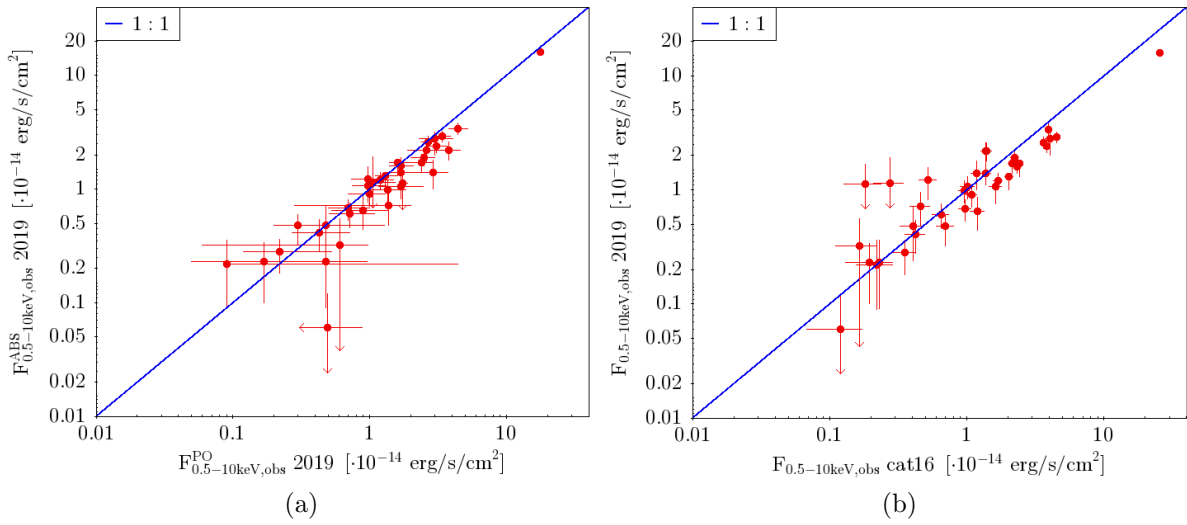
Figure 3.20: Distributions of the 0.5-10 keV observed-frame flux for the 32 X-ray detected sources. (a) Comparison of the computed fluxes between the two models, the $F_{0.5-10 \text{ keV, obs}}^{\text{ABS}}$ is obtained with the ABS model, $F_{0.5-10 \text{ keV, obs}}^{\text{PO}}$ with PO model. The little systematic discrepancy between the two sets of values is caused by the fact that the PO model overestimates the hard band flux, trying to fit the soft band, which is usually more absorbed with respect to the hard band. (b) Comparison of our fluxes with those reported in the COSMOS Legacy catalog. The $F_{0.5-10 \text{ keV, obs}}^{\text{ABS}}$ 2019 is this work flux obtained with ABS model, $F_{0.5-10 \text{ keV, obs}}$ cat16 is the "cat16" flux obtained using a power-law model with photon index $\Gamma = 1.6$ (Civano et al. 2016).
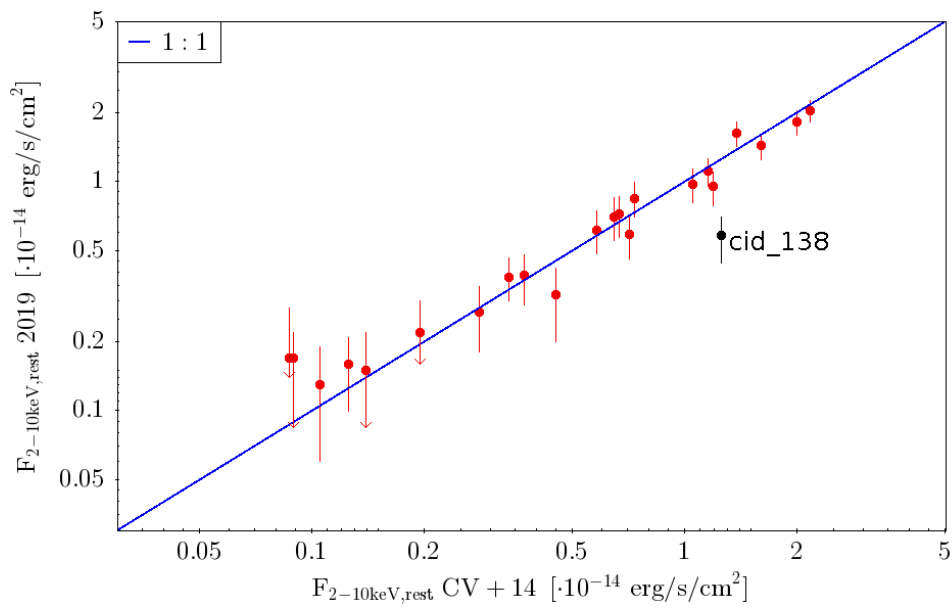
Figure 3.21: Comparison of the 2-10 keV rest-frame fluxes (not corrected for the obscuration) between this work and "CV+14". In black *cid* 138 which exhibits a significant difference between its flux values, caused by a source intrinsic variability. Its case has been deeply analyzed in section 3.3.4. The sources with upper limit are sources not detected in the $2 - 10$ keV rest-frame band.

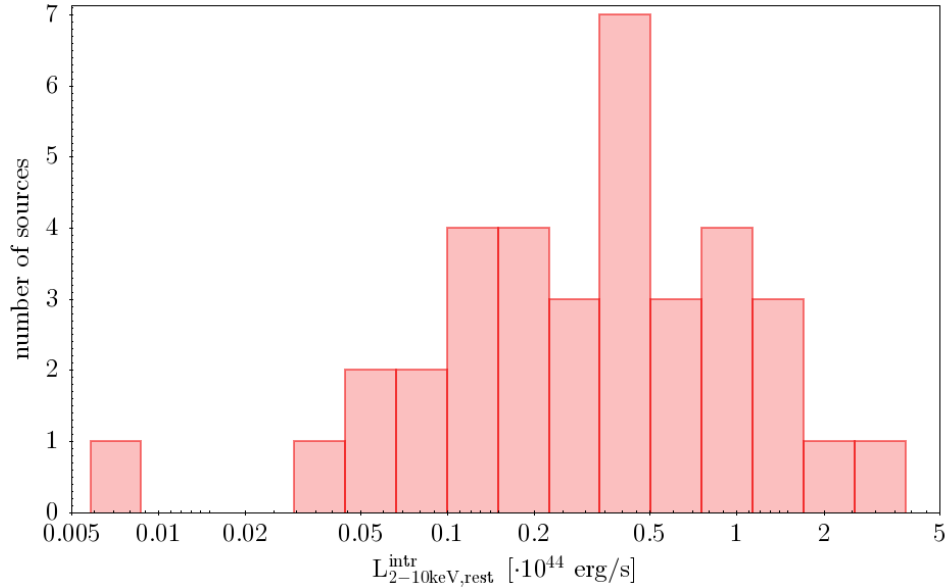the low-count sample of $2.7 \cdot 10^{43}$. We show in Fig 3.22 the intrinsic luminosity value distribution.

Figure 3.22: Distribution of the 2-10 keV rest-frame intrinsic luminosity. It has been obtained from the ABS best-fit model.

X/[NeV]

The ratio between the 2-10 keV rest-frame flux (not corrected for the absorption) and the [NeV] flux can be used as indicator of AGN obscuration (Gilli et al. 2010). In fact, the X-ray flux is correlated with the nuclear emission; because we do not apply any correction for the nuclear absorption, it is also heavily dependent on the obscuration. AGN narrow lines are also closely related to the intrinsic power of the AGN, therefore, the [NeV] can be considered a proxy of the nuclear emission. All of this makes the X/[NeV] ratio a good indicator of the AGN obscuration. As reported by Gilli (2010), unobscured Seyferts have a mean X/[NeV] of ≈ 400, X/[NeV] < 100 identify obscured AGN with $N_H > 10^{23}$ cm^{-2} and X/[NeV] < 15 are specific of CT AGN.

We used the 2-10 keV rest-frame flux (not corrected for the obscuration), previously measured in this work, and the [NeV] flux from Mignoli et al. (2013) to compute the X/[NeV] ratio. The mean X/[NeV] is 313 with a standard deviation of 321. The high-count sample has a mean of 497, while the low-count sample of 148. 10 sources have a X/[NeV] > 400, 10 sources a value < 100. No source has a X/[NeV] less than 15. We have four sources with only an upper limit on the X/[NeV] ratio, this was caused by the

65

fact that we had upper limits on the $2 - 10$ keV flux value. In Fig 3.23a we show the X/[NeV] ratio distribution.
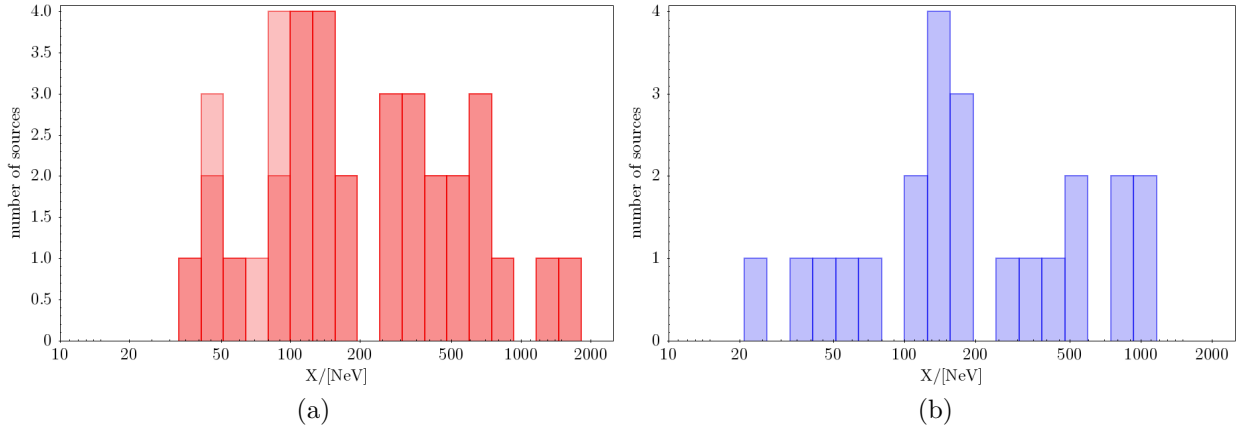

Figure 3.23: X/[NeV] ratio distribution. In the left panel the X/[NeV] ratios from this work are shown for the 36 X-ray detected sources, with the X/[NeV] of source with only upper limit in light red (limits due to the fact that these sources were not detected in the $2 - 10$ keV rest-frame band). In the right panel the X/[NeV] ratios obtained by "CV+14" for C-COSMOS X-ray detected sources (Vignali et al. 2014).

For the source detected both in our work and in "CV+14", we compared their computed X/[NeV] ratio (Figs 3.23b and 3.24). The mean ratio between them is 0.98, with a standard deviation of 0.25, when *cid* 138 is not taken into account. Therefor, our values are in agreement with those of "CV+14".

We show in Fig 3.25 that, although there is not an explicit correlation between N_H and the X/[NeV] ratio, there is no source with both high N_H and high X/[NeV]. Moreover, the sources with the highest values of N_H are those with only upper limit on their X/[NeV] ratio. Our results confirm the reliability of the X/[NeV] ratio as an obscuration tracer.

To have a broader view of the properties of our sources, we compared our data with the X/[NeV] vs N_H diagram as obtained by Gilli et al. (2010). The plot was obtained using the spectral templates of Gilli et al. 2010. These are AGN X-ray spectrum models with a primary power-law with $\Gamma = 1.9$, cut-off energy $E_C = 200$ keV, a variety of absorption $(\log N_h) = 21.5, 22.5, 23.5, 24.5, > 25$, a 6.4 keV emission lines and, in case of obscured spectra, a 3% soft scattered component (e.g. Lanzuisi et al. 2015). The blue solid line was obtained using the mean X/[NeV] ratio of a sample of 74 unobscured Seyfert galaxy in the local Universe and, starting from it, computing the expected X/[NeV] ratio at increasing level of absorption, using the spectral templates. The same computation was carried-out starting from the mean X/[Ne V] ratio $\pm 1\sigma$ and $\pm 90\%$, to produce the 1σ and 90% limits. The procedure is extensively described in Gilli et al. (2010). As we can
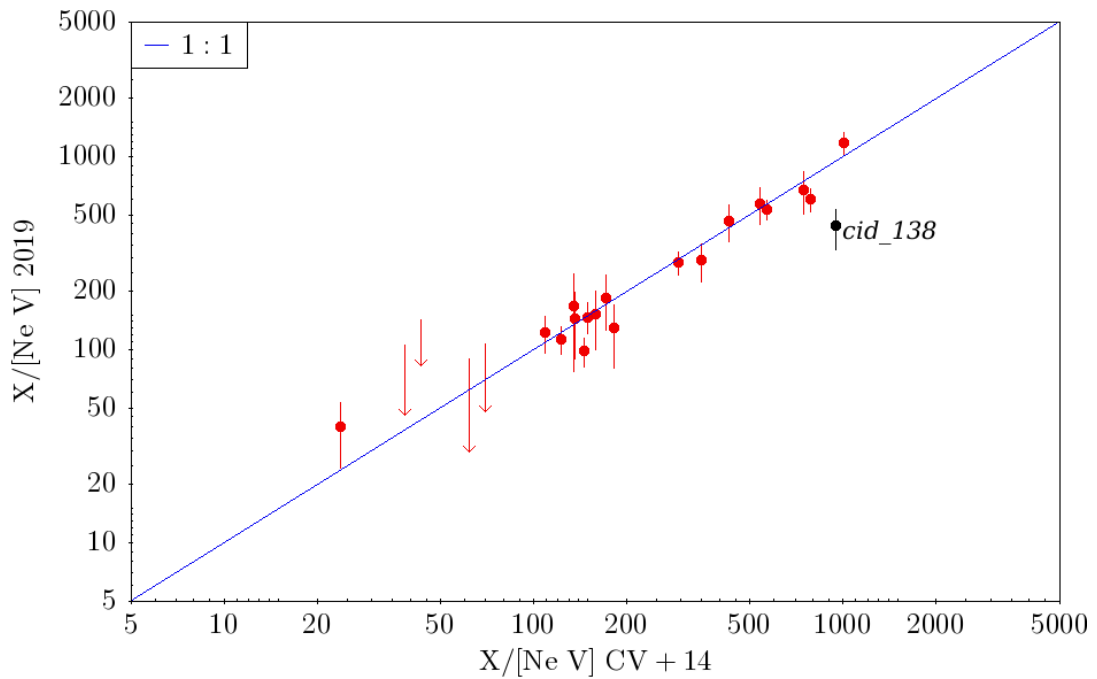
Figure 3.24: Comparison of the X/[NeV] ratios between this work and CV+14 for the 23 sources detected in both works. On our work, four sources had only upper limits on their ratio, due to the fact that are not detected in the $2-10$ keV rest-frame band. In black the X/[NeV] of *cid* 138, which shows a significant difference between its ratios. This was caused by the source intrinsic variability, as explained in details in section 3.3.4.
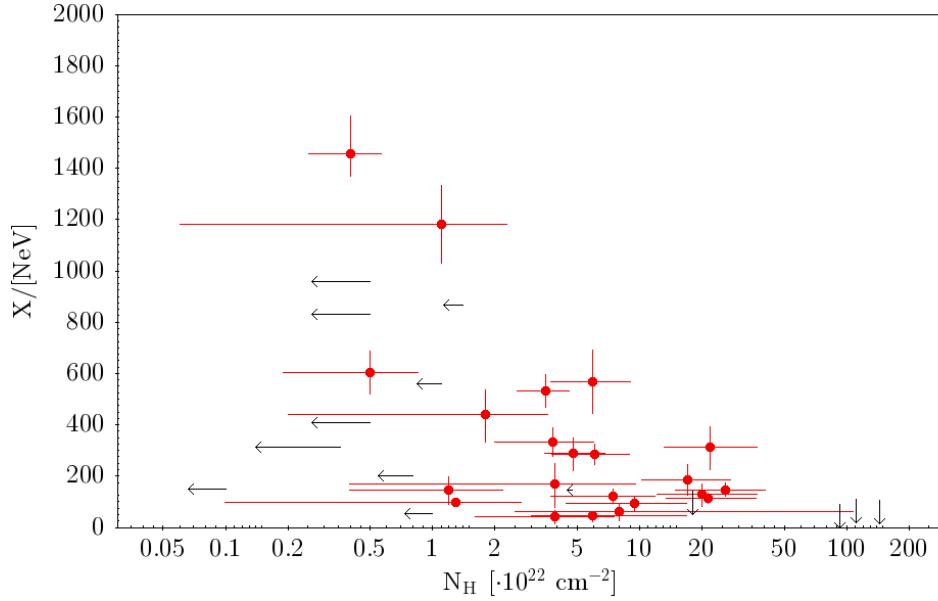
Figure 3.25: Comparison between X/[NeV] ratio and best-fit N_H; black arrows are upper limits.

see from Fig 3.26, our sources populate the obscured quasar region of the diagram, i.e. $10^{21} < N_H < 10^{24}$ cm^{-2}, and the majority of our sample lies within the 1 σ limit.

3.4 X-ray undetected sources

Out of the 94 sources of the [NeV] sample, 58 had no X-ray detection. We decided to measure their $2 - 10$ keV rest-frame flux limit and compute their X/[NeV] upper limit, with the aim of placing constraints on the source obscuration. With the X/[NeV] ratio, we will be able to compare the X-ray undetected sample with the X-ray detected one and, also, with the "CV+14" results.

3.4.1 KS test

In order to investigate if X-ray undetected sources are such because they fall in region with shorter exposure than those of X-ray detected sources, we decided to run a two-samples Kolmogorov–Smirnov (KS) test. The two-sample KS test is a non parametrical test, that checked if the sample S_1, with n elements, and S_2, with m elements, come from the same distribution. The KS statistic is

$$D_{n,m} = \max |C_{1,n} - C_{2,m}| \tag{3.8}$$
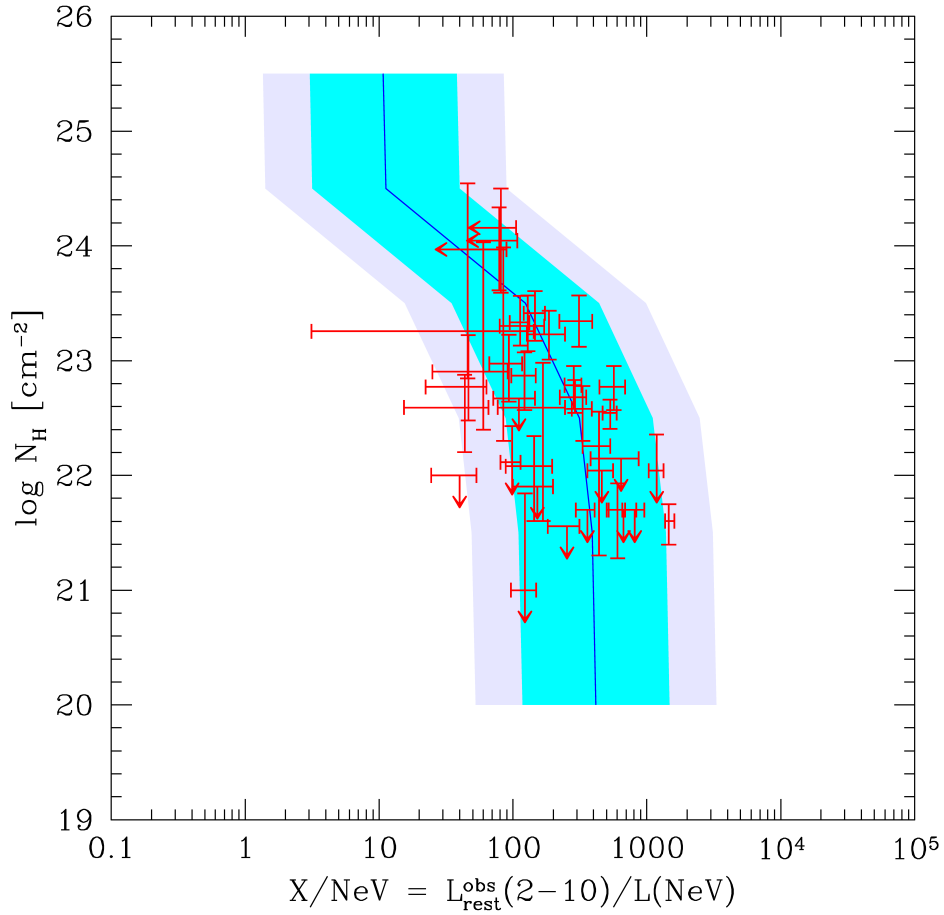
Figure 3.26: X/[NeV] vs N_H diagram. Red dots are data points measured in this work. The solid line shows the expected X/[NeV] values as a function of absorption, as computed by Gilli et al. (2010) using spectral templates with different N_H, starting from the mean X/[NeV] obtained from a sample of unobscured Seyfert galaxy. The light shaded region was computed in the same way, but starting from the mean X/[Ne V]$\pm1\sigma$ and the dark shaded region starting from the mean X/[Ne V]$\pm90\%$.

where C_1 and C_2 are the empirical cumulative distribution of the sample S_1 and S_2. The integral of the Kolmogorov distribution in the range D to infinity gives the null hypothesis probability.

In our case, if we get a KS test probability sufficiently high, we can say that, in our samples, being detected or undetected is not linked to the exposure time. We build two empirical distribution functions of the exposure time for the X-ray detected sources and for the X-ray undetected (Fig 3.27). We obtained a KS statistic of $D = 0.1197$ and a probability $P = 0.89$. This means that, with a confidence of 89%, the undetected sources were undetected because of photon statistics and not because of a lower exposure time.
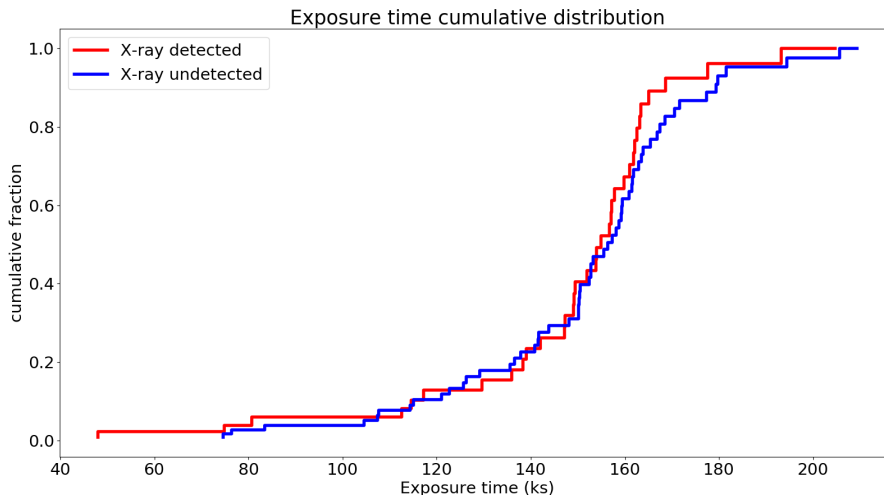
Figure 3.27: Exposure time cumulative distribution of X-ray detected sources (red) and X-ray undetected (blue). We performed a KS test to check if the X-ray undetected sources were undetected because they have shorter exposures than those of the X-ray detected sources. With a confidence of 89%, we excluded that there were a different coverage between the two sample.

3.4.2   Method

We used the *CIAO* (*Chandra Interactive Analysis of Observations*) (version 4.10.) tool `scrflux` to calculate the net count-rate limit for each source and the tool `modelflux` to calculate the flux upper limit.

For each source we checked the observations in which the source fall in. Then, we choose the observations with the highest exposure time on the source position (i.e. considering the decreasing of the effective exposure time caused by the off-axis position of the source). We used `scrflux` to calculate the $0.5 - 7$ keV (observed-frame) net count-rate

in a circular region centered on the source position, that contained the 90% of the PSF at 1 keV. We chose the $0.5 - 7$ keV band to be sure to extract all the counts that the *Chandra ACIS* can detect. The tool measured the counts within the region, and subtracted the background counts to compute the net count value. The background counts were extracted by an annular region centered in the source position, using as inner and outer radii one time and 5 times the radius of the source region. The `psfmethod='quick'` of `scrflux` scaled the net counts according to the fraction of the PSF contained in the extraction region. Finally, the tool computed the net count-rate by dividing the net-counts by the effective (i.e. taking in account the off-axis position) exposure time at the source position. Because these sources were not detected in the X-ray band, these count-rate values can be considered as upper limits.

We used the *CIAO* tool `modelflux` to calculate the upper limit for the flux in the $1 - 5$ keV observed-frame band from the net count-rates. We decided to calculate the flux in the $1 - 5$ keV observed-frame range, because this range matches the $2 - 10$ keV rest-frame if a redshift $z \approx 1$ is assumed. We provided `modelflux` with the ARF and the RMF of each observation and used a power-law model with spectral index $\Gamma = 0.41$, modified by Galactic absorption. The chosen model is the same PO model used for the X-ray detected sources, but with a Galactic absorption fixed at $N_{H,gal} = 1.7 \cdot 10^{20}$ cm^{-2} (it can be considered a mean Galactic absorption value across the COSMOS field) and a fixed $\Gamma = 0.41$.

This model takes into account the source absorption via a flatter photon index than the intrinsic one $\Gamma = 1.8 - 1.9$. In fact, when an obscured AGN spectrum is modeled with a power-law, the absorption has the effect of making the power-law flatter than its intrinsic slope. As the absorption increases, the photon index becomes lower. We assumed that the X-ray undetected sources were obscured at least as the low-count sample; hence, we modeled them with the mean photon index of the low-count sample.

With the aim of checking for the consistency of this procedure, we used it to compute the $2 - 10$ keV rest-frame flux of the X-ray detected sources and compared the values with those obtained from spectral analysis (section 3.3.5). As we can see from Fig 3.28, the two fluxes are not perfectly the same. However, the linear-fit gave us a slope of $m = 1.16$ and a $c = 0.12 \cdot 10^{-14}$ erg/s/cm^2 (y $= m$ x $+ c$), and considering that they are computed using different models and that the "srcflux" fluxes were obtained from only one of the available observation for each source, we considered the results satisfactory.

Upper limits on the intrinsic luminosities

We will see in section 4.3.2 that we will need upper limits on the rest-frame $2 - 10$ keV intrinsic luminosity for the X-ray undetected sources, with the aim of comparing with those obtained from the AGN $12\,\mu$m luminosity using the Gandhi et al. (2009) $L_{12\mu m}$-$L_{2-10keV, \text{intr}}$ relation.

To compute the upper limits on the rest-frame $2 - 10$ keV intrinsic luminosities we
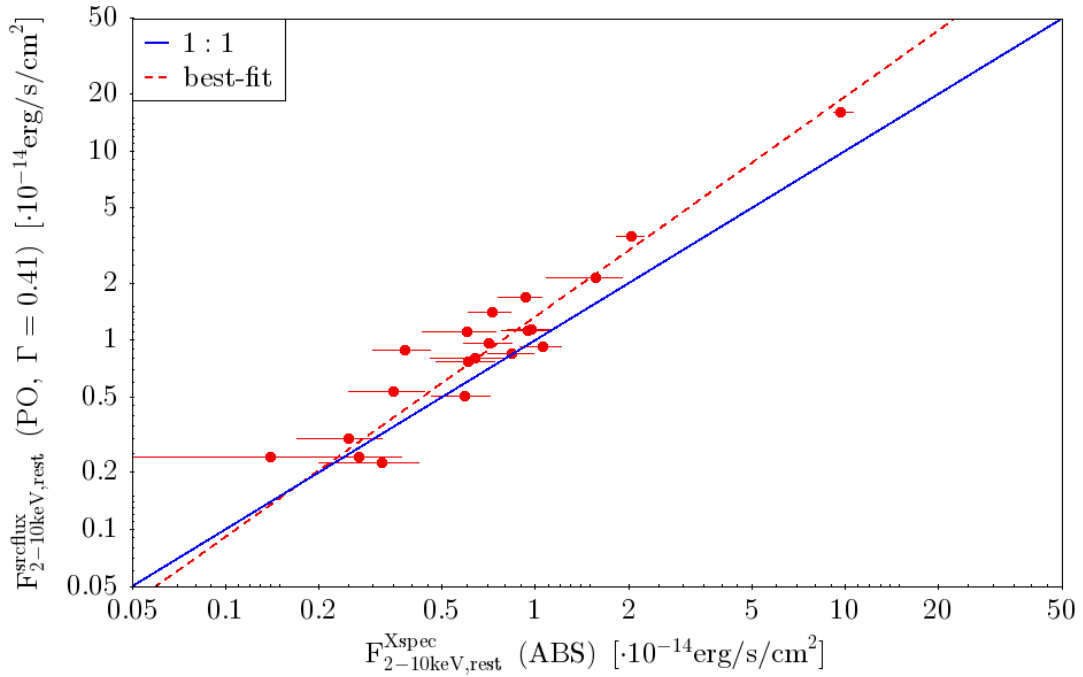
Figure 3.28: Comparison of the $2 - 10$ keV rest-frame flux between the values obtained from spectral analysis (F^{Xspec}) and those from "srcflux". "srcflux" fluxes were obtained with `modelflux` using a power-law model with $\Gamma = 0.41$ and $N_{H,gal} = 1.7 \cdot 10^{20}$ cm^{-2} from the net count-rate computed via `srcflux` tool. The red line is the linear fit, $m = 1.16$ and a $c = 0.12 \cdot 10^{-14}$ erg/s/cm^2 with $F^{srcflux}_{2-10keV,rest} = m\, F^{Xspec}_{2-10keV,rest} + c$.

used the same flux upper limits obtained in the previous section. To justify this choice, we compared, for sources with X-ray detection, the true intrinsic luminosity with that obtained from the count-rate with a power-law of slope $\Gamma = 0.41$. As we can see in figure 3.29, for the low-counts sources (net-counts < 90) the two are in agreement. As we expect the X-ray undetected sources to be similar to the low-counts sources, we can use these luminosity upper limits as intrinsic luminosity upper limits.
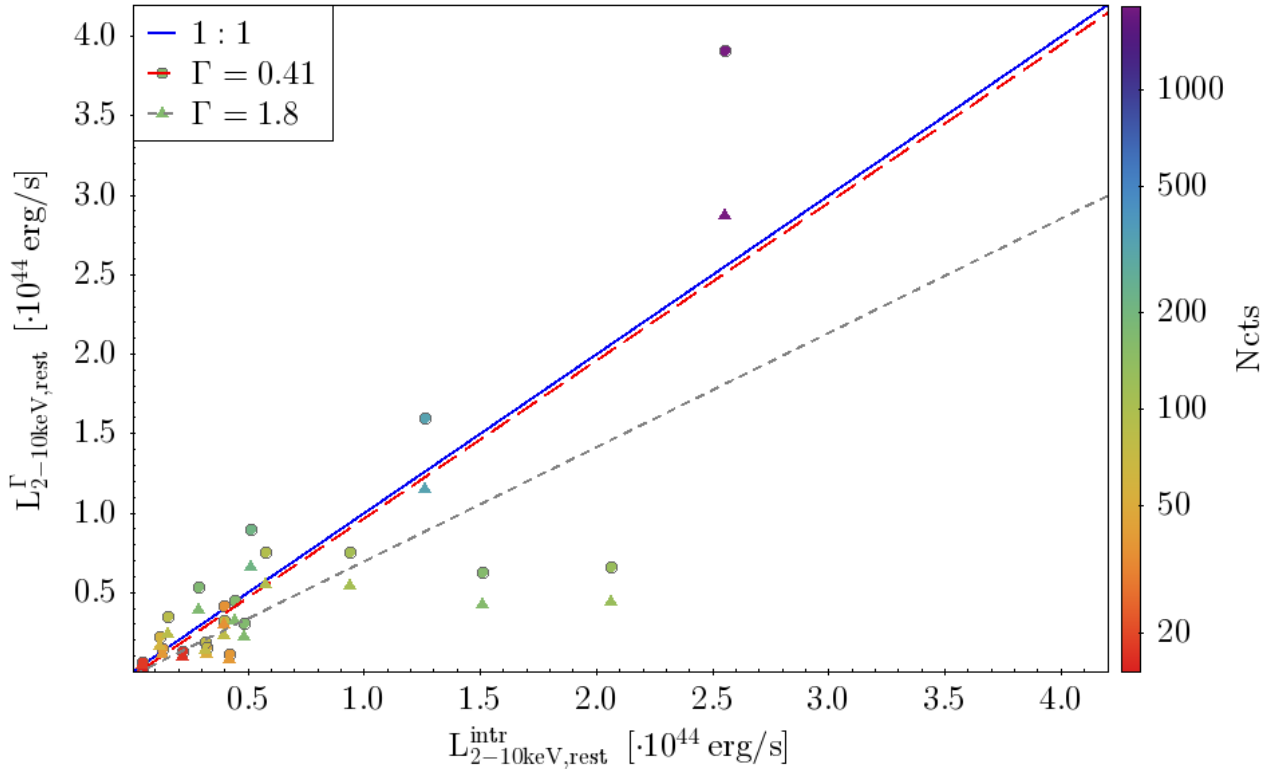
Figure 3.29: Comparison between the $2-10$ keV rest-frame luminosities obtained from X-ray spectral analysis ($L_{2-10\text{keV,rest}}^{\text{intr}}$) and those computed from the count-rate with a power-law model with $\Gamma = 0.41$ (circles) or with $\Gamma = 1.8$ (triangles). The color code indicates the number of net-counts. The red line is the linear-fit of the $\Gamma = 0.41$ luminosities, while the grey line of those computed with $\Gamma = 1.8$. We can see that, for the low-count sources (net-counts < 90), there is little difference between the true intrinsic luminosities and those computed with the $\Gamma = 0.41$, hence justifying the use of the $L_{2-10\text{keV,rest}}^{\Gamma=0.41}$ as intrinsic luminosity for the X-ray undetected sources. The $\Gamma = 1.8$ luminosities are better suited to represent the high-counts sample.

3.4.3 Properties

The mean upper limit on the $2-10$ keV flux for the X-ray undetected sources is $0.45 \cdot 10^{-14}$ erg/s/cm^2, with a standard deviation of $2.2 \cdot 10^{-14}$ erg/s/cm^2.

X/[NeV]

We used the upper limit of the $2-10$ keV rest-frame flux and the [NeV] flux from Mignoli et al. (2013) to compute the X/[NeV] ratio upper limit. The mean X/[NeV] was 87 with a standard deviation of 61 and a median of 69. Thirty-nine sources had an upper limit < 100, and two sources had X/[NeV] ratios < 15. This means that 67% of the X-ray undetected sources are candidate to be AGN with $N_H > 10^{23}$ cm^{-2}, and 3% to be CT AGN. In Fig 3.30 we show the X/[NeV] ratio upper limit distribution. In Fig 3.31 we
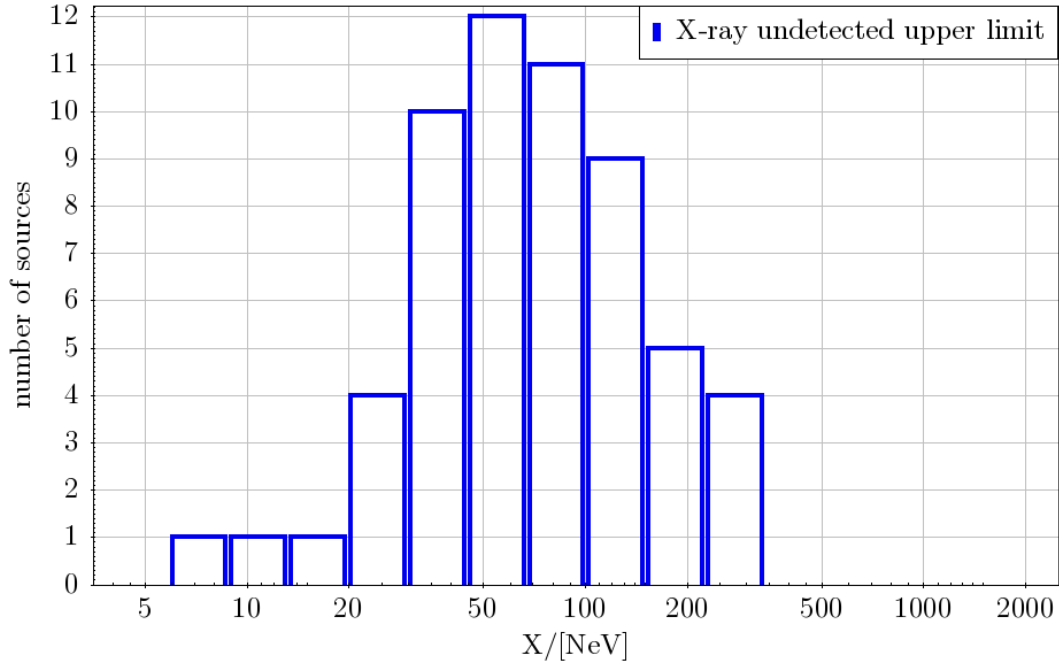
Figure 3.30: Distribution of the upper limits on the X/[NeV] ratio for the 58 X-ray undetected sources. The X/[NeV] upper limits are computed from the [NeV] fluxes obtained by Mignoli et al. (2013) and the $2-10$ keV rest-frame upper limits.

compared the X/[NeV] ratio distribution between the X-ray detected sources and the X-ray undetected. X-ray undetected sources had, on average, lower X/[NeV] ratios. Moreover, X-ray undetected sample had sources with X/[NeV] < 40 and no source with an upper limit on the X/[NeV] ratio above 300.

In Fig 3.32, we compared the distribution of our X/[NeV] ratios with those of the CV+14 X-ray detected sources.
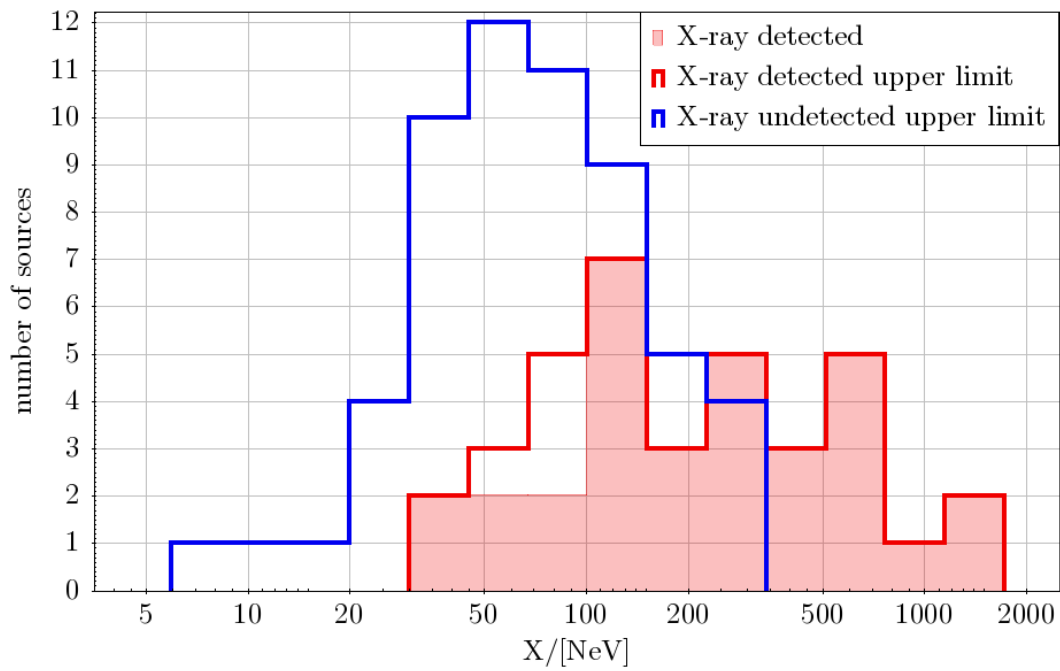
Figure 3.31: Distribution of the X/[NeV] ratio. In red the X/[NeV] ratios of the X-ray detected sources, in blue the X/[NeV] upper limits of the X-ray undetected sources. The fact that four detected sources have a upper limits on their ratio is caused by these sources being undetected in the $2 - 10$ keV rest-frame band.
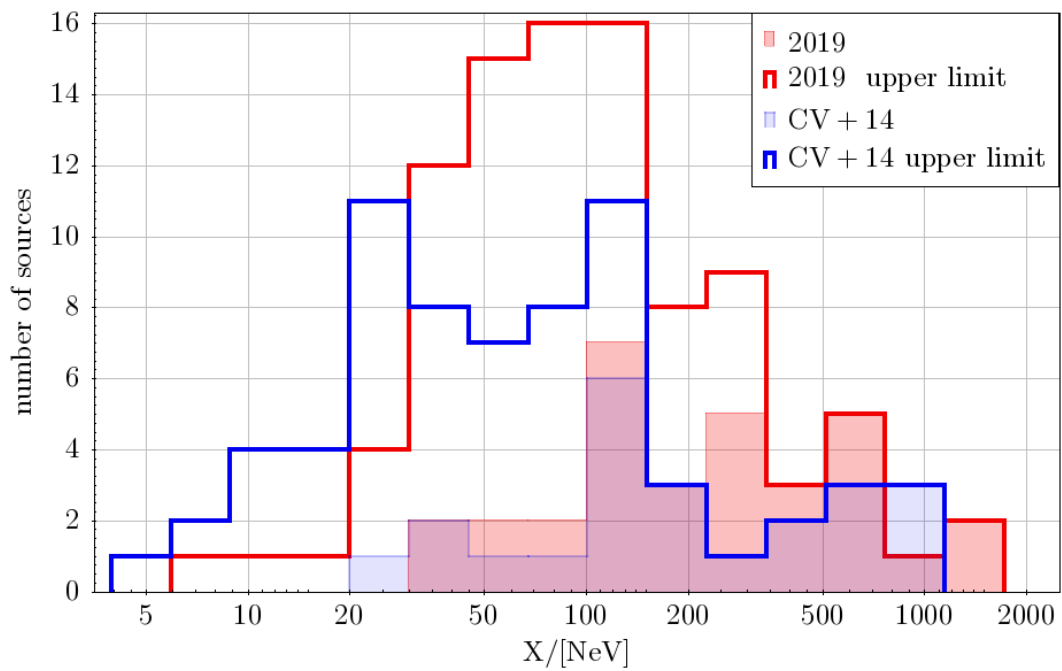
Figure 3.32: Comparison of the X/[NeV] ratios between the results of this work (red) and those from "CV+14" (blue). Filled and empty histograms refer to X-ray detections and upper limits, respectively.

3.5 X-ray analysis results

At energies between 20 and 40 keV, where the X-ray background peaks, only a fraction of its emission has been resolved into individual sources ($\approx 30 - 40\%$). X-ray background synthesis models predict that the density of the XRB missing sources with luminosity between $10^{43} - 10^{44}$ erg/s should peak at $z \approx 1$ and that a non-negligible fraction of these sources should be CT AGN. With the aim of investigating these sources, and in particular their obscuration, we studied a sample of [NeV] selected type 2 AGN. The use of the presence of narrow [NeV] emission lines in the spectra as selection method, assured as that our sample is composed only of type 2 AGN in the $0.65 < z < 1.20$ redshift range.

94 AGN belong to our sample, we obtained their X-ray characteristics via spectral analysis for the 36 sources with X-ray detection and using flux upper limits for the 58 X-ray undetected sources. In Tables 3.9 and 3.10 we report the main properties of the [NeV] sample.

Thirty-six of the 94 [NeV] selected AGN were detected in X-ray Cosmos Legacy survey, 13 sources more than in the CV+14. The larger number of X-ray detections is due to the fact that COSMOS Legacy has a wider coverage and also deeper observations on the outer area of the C-COSMOS survey.

The sample showed a wide range of absorption, with eleven sources with low value of obscuration, nine with high obscuration ($N_H > 10^{23}$ cm^{-2}) and two that can be classified as CT AGN. The use of X/[NeV] ratio confirmed the absorption values found via spectral analysis. Using the X/[NeV] ratio, ten sources resulted to be unobscured (X/[NeV]> 400) and ten with a $N_H > 10^{23}$ cm^{-2} (X/[NeV]< 100), although no one resulted CT (X/[NeV]< 15). One source show a 6.97 keV emission line with a ≈ 2.6 significance; in another source 6.4 keV and 6.97 keV emission line were scarcely detected. Source *cid* 1508 showed a spectrum with soft excess and was fitted with a partial covering model. We computed a fraction of coverage $> 78\%$. Source *cid* 138 showed significant flux variability between 2009 and 2014 observations. The flux variability was not coupled with a similar variability of photon index, absorption or HR. We deduced that there was a variation of the AGN intrinsic luminosity, maybe linked to a variation of the accretion rate.

58 sources have no X-ray detection. We computed their $2 - 10$ keV (rest-frame) flux upper limits and, with those, their X/[NeV] upper limits. Thirty-nine sources ($\approx 67\%$) had X/[NeV] ratios compatible with $N_H > 10^{23}$ cm^{-2}, two can be classified as CT AGN. Compared to the X-ray detected ratios, they were compatible with sources, on average, more absorbed and, also, with higher values of obscuration.

Considering the whole [NeV] sample, at least 50% of the sources have X/[Ne V] ratios compatible with absorption $N_H > 10^{23}$ cm^{-2}, and at least 4% of the sources could be CT AGN.

zID	xID	z	N_H	F_{2-10}	X/NeV	L_{intr}
841281	*lid* 1856	0.7348	$0.4^{+0.2}_{-0.2}$	$9.69^{+0.93}_{-0.49}$	1457^{+147}_{-87}	$2.56^{+0.15}_{-0.14}$
819469	*cid* 339	0.6865	$0.5^{+0.4}_{-0.3}$	$1.82^{+0.21}_{-0.22}$	604^{+82}_{-85}	$0.41^{+0.06}_{-0.05}$
833510	*cid* 522	0.9444	$3.5^{+1.1}_{-1.0}$	$2.04^{+0.21}_{-0.22}$	531^{+63}_{-65}	$1.26^{+0.19}_{-0.13}$
831966	*cid* 110	0.7295	< 0.5	$1.43^{+0.17}_{-0.19}$	668^{+163}_{-168}	$0.36^{+0.05}_{-0.05}$
820742	*cid* 173	0.9997	$1.1^{+1.2}_{-1.0}$	$1.62^{+0.20}_{-0.20}$	1182^{+151}_{-151}	$0.97^{+0.18}_{-0.17}$
841734	*lid* 1840	1.0062	< 0.5	$0.93^{+0.12}_{-0.17}$	361^{+47}_{-66}	$0.52^{+0.07}_{-0.06}$
817002	*cid* 381	0.8649	$6.1^{+2.9}_{-2.3}$	$1.11^{+0.15}_{-0.16}$	285^{+39}_{-41}	$0.64^{+0.16}_{-0.14}$
836036	*lid* 279	0.8819	< 0.5	$0.73^{+0.11}_{-0.12}$	810^{+148}_{-157}	$0.29^{+0.04}_{-0.04}$
803996	*lid* 1478	0.8326	$3.8^{+2.2}_{-1.8}$	$1.06^{+0.16}_{-0.17}$	332^{+55}_{-58}	$0.48^{+0.12}_{-0.10}$
816439	*cid* 496	0.8993	$1.3^{+1.4}_{-1.2}$	$0.95^{+0.15}_{-0.17}$	98^{+16}_{-18}	$0.45^{+0.11}_{-0.10}$
832900	*cid* 456	1.023	$21.5^{+15.2}_{-8.0}$	$0.97^{+0.16}_{-0.16}$	113^{+19}_{-19}	$1.51^{+0.74}_{-0.43}$
813287	*cid* 221	0.7488	< 1.1	$0.72^{+0.14}_{-0.15}$	462^{+96}_{-102}	$0.20^{+0.05}_{-0.04}$
846478	*cid* 620	1.1767	$25.9^{+14.6}_{-11.0}$	$0.84^{+0.15}_{-0.14}$	146^{+27}_{-26}	$2.06^{+0.79}_{-0.60}$
841340	*lid* 1826	1.1733	$7.4^{+4.4}_{-3.7}$	$0.71^{+0.13}_{-0.12}$	122^{+26}_{-25}	$0.94^{+0.25}_{-0.23}$
837988	*cid* 138	0.7034	$1.8^{+1.8}_{-1.6}$	$0.58^{+0.12}_{-0.14}$	440^{+94}_{-109}	$0.15^{+0.05}_{-0.05}$
843107	*lid* 489	0.8499	< 1.4	$1.57^{+0.34}_{-0.48}$	643^{+225}_{-264}	$0.58^{+0.18}_{-0.12}$
825282	*cid* 1126	0.9588	$17.0^{+10.3}_{-6.8}$	$0.70^{+0.15}_{-0.15}$	186^{+59}_{-59}	$0.80^{+0.34}_{-0.26}$
829955	*cid* 717	0.8913	$0.1^{+0.6}_{-0.1}$	$0.38^{+0.08}_{-0.08}$	123^{+26}_{-26}	$0.15^{+0.04}_{-0.03}$
833208	*cid* 503	0.9106	$5.9^{+3.1}_{-2.2}$	$0.61^{+0.13}_{-0.13}$	566^{+123}_{-123}	$0.40^{+0.14}_{-0.10}$
833904	*cid* 426	0.8643	$4.8^{+2.0}_{-1.3}$	$0.59^{+0.12}_{-0.13}$	290^{+62}_{-66}	$0.32^{+0.10}_{-0.08}$
812111	*cid* 254	0.7106	$1.2^{+1.0}_{-0.8}$	$0.39^{+0.09}_{-0.10}$	144^{+53}_{-55}	$0.10^{+0.04}_{-0.03}$
820983	*lid* 689	0.6752	< 0.4	$0.60^{+0.14}_{-0.17}$	253^{+59}_{-72}	$0.12^{+0.03}_{-0.03}$
813850	*lid* 3483	0.6606	$22.0^{+15.0}_{-8.8}$	$0.64^{+0.16}_{-0.18}$	311^{+80}_{-90}	$0.33^{+0.13}_{-0.09}$
825838	*cid* 1130	0.7864	< 0.8	$0.27^{+0.08}_{-0.09}$	153^{+47}_{-52}	$0.08^{+0.02}_{-0.02}$
813250	*cid* 1019	0.7302	$144.0^{+172.0}_{-105.0}$	< 0.17	< 81	$1.29^{+15.84}_{-1.17}$
809597	*lid* 1603	0.9653	< 4.7	$0.25^{+0.07}_{-0.08}$	111^{+35}_{-39}	$0.13^{+0.07}_{-0.05}$
810378	*cid* 401	0.9707	$20.0^{+17.0}_{-7.9}$	$0.32^{+0.10}_{-0.12}$	129^{+41}_{-49}	$0.42^{+0.26}_{-0.16}$
900121	*lid* 1869	1.1684	$9.4^{+7.4}_{-5.0}$	$0.35^{+0.09}_{-0.10}$	93^{+24}_{-27}	$0.40^{+0.21}_{-0.14}$
840085	*cid* 1230	0.7535	< 1.0	$0.16^{+0.05}_{-0.06}$	40^{+13}_{-16}	$0.04^{+0.02}_{-0.01}$
817977	*cid* 1169	0.9591	$3.9^{+5.7}_{-3.5}$	$0.13^{+0.06}_{-0.07}$	167^{+78}_{-91}	$0.09^{+0.07}_{-0.05}$
840744	*lid* 2210	0.7353	$3.9^{+3.6}_{-2.3}$	$0.14^{+0.07}_{-0.09}$	44^{+22}_{-28}	$0.05^{+0.04}_{-0.02}$
804237	*lid* 1459	1.0001	$5.9^{+10.8}_{-2.9}$	$0.27^{+0.10}_{-0.14}$	46^{+17}_{-24}	$0.22^{+0.19}_{-0.11}$
826095	*cid* 2454	0.764	$18.0^{+79.0}_{-16.0}$	< 0.17	< 85	$0.15^{+0.16}_{-0.09}$
836868	*lid* 3017	0.6793	$8.0^{+99.9}_{-5.5}$	$0.14^{+0.07}_{-0.08}$	60^{+31}_{-35}	$0.05^{+0.48}_{-0.03}$
820695	*cid* 1706	0.7642	111^{+105}_{-70}	< 0.22	< 79	$0.85^{+2.63}_{-0.62}$
817871	*cid* 1508	0.6743	93^{+257}_{-86}	< 0.15	< 46	< 0.03

Table 3.9: X-ray detected sources. zID: zCOSMOS source ID; xID: COSMOS Legacy source ID; z: redshift; N_H: best-fit column density from ABS model, in units of 10^{22} cm^{-2}; F_{2-10}: $2-10$ keV rest-frame (not corrected for the absorption) flux in units of 10^{-14} erg/s/cm^2; X/NeV: ratio between $2-10$ keV rest-frame (not corrected for the absorption) flux and [NeV] flux from Mignoli et al. 2013; L_{intr}: $2-10$ keV rest-frame intrinsic luminosity, obtained from spectral fitting with ABS model with $N_H = 0$, in units of 10^{44} erg/s.

zID	z	F_{2-10}	X/NeV	zID	z	F_{2-10}	X/NeV
803886	0.8962	< 0.18	< 59	824736	1.1427	< 0.22	< 32
804431	0.702	< 0.06	< 45	825958	0.7026	< 0.11	< 47
805117	0.9999	< 0.16	< 133	826023	0.9508	< 0.11	< 59
807963	0.9198	< 0.27	< 107	826693	0.6994	< 0.06	< 58
809056	1.0705	< 0.12	< 106	826908	1.0246	< 1.24	< 193
809579	0.9195	< 0.11	< 152	829551	0.8927	< 0.13	< 74
811284	0.9558	< 0.12	< 37	829938	0.8821	< 0.06	< 39
811645	0.8092	< 0.06	< 67	830027	0.9307	< 0.13	< 38
811887	0.7297	< 0.10	< 20	831655	0.7567	< 0.15	< 138
812193	0.898	< 0.17	< 139	832252	0.7878	< 0.19	< 233
812432	0.6611	< 0.06	< 6	832576	0.7331	< 0.11	< 100
812665	0.7301	< 0.24	< 149	832803	0.9274	< 0.25	< 108
812953	0.7742	< 0.11	< 44	832907	0.9608	< 0.13	< 64
813366	0.6685	< 0.06	< 12	834572	0.8475	< 0.15	< 93
813460	0.6646	< 0.06	< 69	837072	1.1475	< 0.15	< 21
814229	0.7618	< 0.14	< 36	837402	0.8835	< 0.31	< 76
817886	0.9603	< 0.12	< 162	837589	0.9214	< 0.30	< 242
818408	0.6689	< 0.13	< 34	839683	0.8887	< 0.16	< 151
818478	0.8946	< 0.06	< 35	839719	0.8916	< 0.18	< 89
819116	0.715	< 0.09	< 81	844011	0.8626	< 0.17	< 232
819306	0.9394	< 0.16	< 84	845677	0.7264	< 0.06	< 41
819927	0.6973	< 0.07	< 29	846342	0.7353	< 0.18	< 29
820589	0.8796	< 0.07	< 30	846722	0.7681	< 0.11	< 101
822904	0.8357	< 0.17	< 161	846946	0.7379	< 0.12	< 115
823097	0.8044	< 0.08	< 24	847446	1.0273	< 0.10	< 48
823162	0.8489	< 0.15	< 53	847932	0.6789	< 0.20	< 92
823537	0.9225	< 0.32	< 177	850792	1.0151	< 0.33	< 255
824025	0.8503	< 0.17	< 47	851740	1.0245	< 0.21	< 62
824548	0.748	< 0.09	< 86	910023	0.9802	< 0.07	< 53

.

Table 3.10: X-ray undetected sources. zID: zCOSMOS source ID; z: redshift; F_{2-10}: $2-10$ keV rest-frame flux in units of 10^{-14} erg/s/cm^2, obtained with `modelflux` using a power-law model with $\Gamma = 0.4$ and $N_{H,gal} = 1.7 \cdot 10^{20}$ cm^{-2} from the net count-rate computed via `srcflux` tool; X/NeV: ratio between $2-10$ keV rest-frame flux and [NeV] flux from Mignoli et al. 2013.

Chapter 4

SED analysis

In this chapter I present the results obtained through an analysis of the far-IR-to-optical SED of our sample with the aim of characterizing both the AGN and the host galaxies. The use of a SED-fitting algorithm allows us to separate the galaxy emission from the AGN emission. We used the latter, along with scaling relations, to obtain the AGN bolometric and $2 - 10$ keV luminosities, which were then compared to the results of the X-ray spectral analysis. This procedure allows us to compare the AGN properties obtained via X-ray analysis with those from SED-fitting, showing the power of the multi-wavelength approach to the study of AGN. As we will see, this type of approach is fundamental in AGN studies; in fact, some AGN of our sample did not show significant indications of AGN emission in the SED and would not be classified as AGN only on the basis of their optical-IR SED. The other way around is also true, as obscured AGN not detected in the X-ray bands can be identified on the basis of their mid-IR SED.

Moreover, the SED-fitting algorithm provided us the properties of the host-galaxies. In particular, we derived the stellar mass of the galaxies and their star formation rates.

In section 4.1 and 4.2 we present the data and the adopted SED-fitting algorithm. In section 4.3 we discuss the torus templates used to model the AGN emission. The SED-fitting results are presented in section 4.3.2, along with the comparison with the X-ray analysis results. In section 4.4 we estimate the significance of the AGN emission in the SED-fitting. Section 4.5 contains the comparison with the results obtained imposing only *edge-on* torus models. Finally, in section 4.6 we present an overview of the SED analysis results.

All the values are reported with the associated $1\,\sigma$ uncertainties; all the mean values are computed without considering the sources with upper limits and are given with their standard deviation of the mean.

4.1 Sample

The optical and IR data used in this work come from the COSMOS 2015 catalog (Laigle et al. 2016). This catalog contains photometry in 30 bands for more than half a billion objects in the COSMOS field, along with matches with X-ray, near ultraviolet, and Far-IR data. The properties of this catalog are presented in section 2.3.3.

We used data from 27 photometric bands, excluding the two narrow bands NB711 and NB816 and the GALEX data, of the COSMOS2015 catalog (see table 2.1). We also used the COSMOS2015 matches with the $24\mu m$ band from the MIPS (Multi-Band Imaging Photometer) detector on-board *Spitzer* and with the $100\mu m$ and $160\mu m$ bands and the $250\mu m$, $350\mu m$ and $500\mu m$ bands from the PACS and SPIRE detectors of *Herschel*. In total we have 33 filters at our disposal: 15 optical, 10 near-IR, 3 mid-IR and 5 submillimetric; their wavelength distribution is shown in fig 4.1.

It is important to note that not all the sources were detected in all the 33 filters.
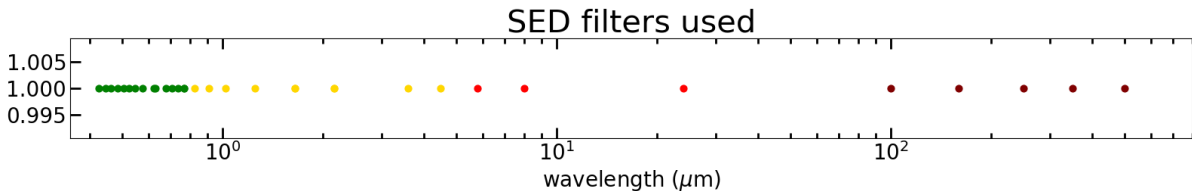

Figure 4.1: Distribution of the centroid of the photometric bands used for the SED-fitting. Green points are optical wavelengths, yellow near-IR, red mid-IR and brown far-IR and sub-millimetric.

In the COSMOS2015 catalog the photometry was provided, for each band, using the $2''$ and $3''$ aperture magnitudes and the $2''$ and $3''$ aperture fluxes. We used the $3''$ aperture fluxes, with related 1σ errors.

4.2 Sed-fitting algorithm code

We used the algorithm *SED3FIT* (Berta et al. 2013 and da Cunha et al. 2008) that performed SED-fitting with a combination of three components: stellar emission, dust emission from star formation and a possible dusty torus/AGN. The stellar and dust emission are linked by energy balance arguments: the amount of energy absorbed by dust at UV-optical wavelength is re-emitted at infrared wavelengths. Torus emission is independently included.

SED3FIT is based on the *MAGPHYS* code (da Cunha et al. 2008), that models the galactic emission, with the addition of the possibility to include the AGN/torus emission. We will briefly introduce the *MAGPHYS* code and then the peculiar characteristic of the *SED3FIT* algorithm.

4.2.1 MAGPHYS

MAGPHYS (Multi-wavelength Analysis of Galaxy Physical Properties) is a model package to interpret observed SEDs of galaxies (at rest wavelengths in the range 912Å $< \lambda <$ 1mm) in terms of galaxy-wide physical parameters pertaining to the stars and the interstellar medium, following the approach described in da Cunha et al. (2008).

The analysis of the SED of an observed galaxy with MAGPHYS is carried out in two steps:

1. The creation of a library of model spectral energy distributions at the same redshift and in the same photometric bands as the observed galaxy, for wide ranges of plausible physical parameters.

2. The build-up of the marginalized likelihood distribution of each physical parameter of the observed galaxy, through the comparison of the observed spectral energy distribution with all the models in the library.

The code uses two libraries of models: one that takes into account the stellar emission and the effects of dust attenuation (we will refer to these models as "optical models"), the other that include the IR emission of the dust (we will refer to them as "IR models"). The optical and infrared libraries are linked together to provide the full SED of model galaxies from the far ultraviolet to the far-infrared wavelengths.

The optical models

The optical models store 50 000 stellar population spectra, with both the dust-free spectrum and the dust-attenuated spectrum for each galaxy template. These spectra were generated using the Bruzual (2007) stellar population synthesis code.

The SED at time t of a stellar population characterized by a star formation rate $\psi(t)$ is given by:

$$L_\lambda(t) = \int_0^t dt' \, \psi(t - t') \, S_\lambda(t', Z) e^{-\tau_\lambda(t')} \tag{4.1}$$

where $S_\lambda(t', Z)$ is the power radiated per unit wavelength and per unit initial mass by a simple stellar population (SSP) of age t' and metallicity Z, and $\tau_\lambda(t')$ is the 'effective' absorption optical depth of the dust seen by stars of age t'.

The main adjustable parameters of these models are:

- **Star formation history:** the star formation rate as a function of time $\psi(t)$. It is build as a continuous star-formation (characterized by an age t_{form} and a star formation timescale parameter γ, with $\psi(t) \propto e^{-\gamma t}$) and random bursts superimposed to this continuous model.

- **Metallicity:** uniformly distributed between 0.02 and 2 times solar metallicity.

- **Dust attenuation:** computed using the simple, angle-averaged model of Charlot et al. (2000). This accounts for the fact that stars are born in dense molecular clouds, which dissipate typically on a timescale of 10^7 yr.

The IR models

The IR models store 50 000 dust emission spectra. The mid- and far-infrared emission from dust in galaxies is computed using the model of da Cunha et al. (2008). The total dust emission from a galaxy is the sum of the dust emission originating from the stellar birth clouds and the dust emission originating from the ISM (Inter Stellar Medium).

- **Birth clouds:** The SED of the power re-radiated by dust in the stellar birth clouds is computed as the sum of three components: a component of polycylic aromatic hydrocarbons (PAHs); a mid-infrared continuum characterizing the emission from hot grains at temperatures in the range 130-250 K; and a component of grains in thermal equilibrium with adjustable temperature in the range 30-60 K.

- **Ambient ISM:** In the ambient ISM, the relative proportions of the three components are fixed, for simplicity, to reproduce the spectral shape of diffuse cirrus emission in the Milky Way, and a fourth component of cold grains in thermal equilibrium with adjustable temperature in the range 15–25 K is included.

Combined ultraviolet-to-infrared spectra

MAGPHYS code provides a consistent interpretation of ultraviolet, optical and infrared SEDs of galaxies. This is achieved by accounting consistently for the total energy absorbed by dust in stellar birth clouds and in the ambient ISM, and for the re-distribution of this energy at far-infrared wavelengths. The main underlying assumptions are that the energy re-radiated by dust is equal to that absorbed (i.e. the energy is conserved), and that starlight is the only significant source of dust heating in the galaxies under study.

Different combinations of star formation histories, metallicities and dust content can lead to similar amounts of energy absorbed by dust in the stellar birth clouds, and these energies can be distributed in wavelength using different combinations of dust parameters. Consequently, in the process of fitting, a wide range of optical models is associated with a wide range of infrared spectra and compared to observed photometry, seeking for χ^2 minimization.

4.2.2 SED3FIT

As mentioned above, one of the main assumptions of the *MAGPHIS* code is that the only significant source of dust heating is the starlight. This means that any possible

contribution of the AGN to the SED is ignored. The *SED3FIT* code solves this problem by adding a warm dust component to the modeled SED emission. This represents dust surrounding the active nucleus, assumed to be distributed in a toroidal region, hence referred as "torus" for simplicity.

For finding the best-fit model the code uses χ^2 minimization, via several steps:

1. the *MAGPHYS* star and dust model is freely normalized and subtracted from the observed photometry.

2. The torus emission is added to reproduce what is left out from this subtraction.

3. The dust emission, as in the *MAGPHYS* code, is linked to the stellar optical components

Allowing the normalization of stars+dust to be free, i.e. not strictly anchored to the observed photometry but simply randomly picked from a grid of values, the torus is effectively fit to the data in a simultaneous 3-component mode.

The code can be fed with any AGN/torus model, providing a list of luminosities (in erg/s/μm) associated to a list of wavelengths. We used a sub-sample of the torus library produced by Fritz et al. (2006) and Feltre et al. (2012), described in the following section.

The AGN/torus models

The torus library we used to model the AGN contributions to the SED assumes that the AGN dust and gas are distributed in a toroidal shape, the so-called "smooth-torus" model. It was developed to study the SED of 58 extra-galactic (both type-1 and type-2) sources using archival optical and IR data (Fritz et al. 2006) and updated by Feltre (2012) to make comparisons with the SED produced using a "clumpy torus" model.

The geometry of the torus is the *flared disc*, that can be represented as two concentric spheres, delimiting respectively the inner and the outer torus radius, having the polar cones removed. The size of the torus is defined by the outer radius R_{max} - the inner radius being defined by the sublimation temperature of dust grains under the influence of the strong nuclear radiation field - and by the angular opening angle Θ of the torus itself.

The main dust components are silicate and graphite grains, in almost equal percentages. The former are responsible for the observed absorption feature at $\sim 9.7\mu$m in type-2 objects, while the latter are responsible for the rapid decline of the emission at wavelength less than a few μm, corresponding to a black body emission of about 1500 K, the sublimation temperature for these particular grains. Different grain sizes, providing different scattering and absorption coefficients, were taken into account.

The torus density law adopted was:

$$\rho(r, \theta) = \alpha \cdot r^\beta \cdot e^{-\gamma \, |\cos \theta|} \tag{4.2}$$

where α is a normalization constant and the parameters β and γ allow to create density gradients both in radial (r) and in polar (θ) directions.

The models assume that the torus is illuminated by a central point-like energy source with isotropic emission. Its spectrum is described as a composition of power-laws with variable indices.

$$L(\lambda) \propto \begin{cases} \lambda^1 & \text{if} \quad 0.001 < \lambda < 0.05 \quad [\mu\text{m}] \\ \lambda^{-0.2} & \text{if} \quad 0.05 < \lambda < 0.125 \quad [\mu\text{m}] \\ \lambda^{-1.5} & \text{if} \quad 0.125 < \lambda < 10 \quad [\mu\text{m}] \\ \lambda^{-4} & \text{if} \quad \lambda > 10 \quad [\mu\text{m}] \end{cases} \qquad (4.3)$$

The radiation emitted by the above described physical configuration is given by the sum of the primary source located in the torus center and a secondary contribution given by thermal and scattering dust emission. Therefore dust plays a double role, first absorbing the radiant energy emitted by the primary source, partially or totally obscuring it, then re-emitting it at longer wavelengths, typically in the spectral range $1 - 1000 \, \mu\text{m}$. A complication arises from the fact that dust can be optically thick to its own radiation. This required the solution of the radiative transfer equation (see Fritz et al. 2006).

In figure 4.2 we show a schematic lateral view of the torus geometry used.
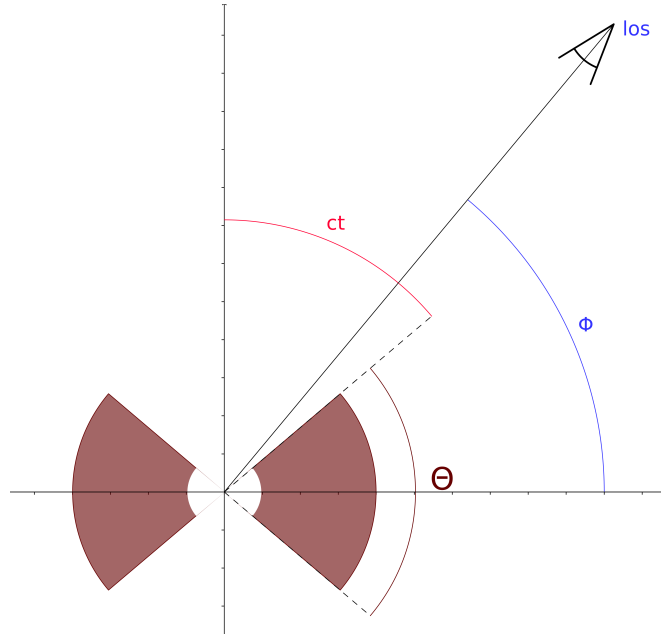

Figure 4.2: Schematic lateral view of the torus geometry used to model the AGN contributions to the SED in case of a flared disc.

Adding the emission from all torus elements to that of the central source, attenuated by the correct value of optical depth when needed, yields the total emitted spectrum. It

was computed for 10 different inclination values of the line-of-sight Φ and for different torus parameters.

- **Φ**: is the angle between the line of sight and the equatorial plane. It spans from $0°$ to $90°$ in steps of $10°$.

- **R**: is the outer to inner ratio of the torus, $R = R_{\max}/R_{\min}$. It can have values of $R =10$, 30, 60, 100 and 150.

- **ct**: is the half width of the torus aperture. It is $ct = 90° - \Theta/2$, where Θ is the amplitude of the torus. It can have values of $ct = 20°$, $40°$ and $60°$, corresponding to torus apertures of $\Theta = 140°$, $100°$ and $60°$.

- **β**: is the slope of the torus radial density profile (eq 4.2). Its values can be $\beta = 0.00$, -0.25, -0.50, -0.75 and -1.0.

- **γ**: is the slope of the torus polar density profile (eq 4.2). It can have values of $\gamma = 0.0$, 2.0, 4.0 and 6.0.

- **τ_{eq}**: is the torus equatorial optical depth at $9.7\,\mu$m. Its values can be $\tau_{\mathrm{eq}}(9.7) = 0.1$, 0.3, 0.6, 1.0, 2.0, 3.0, 6.0 and 10.0.

In figure 4.3 we show the spectra of a torus model for different values of Φ. Since in this example we have chosen a value of $ct = 40°$, the lines of sight with $\Phi < 50°$ intercept the torus, hence their spectrum is that of a *type 2* object. Most notably, these spectra show the $\sim 9.7\,\mu$m silicate absorption feature, usually found in type 2 of objects. Values of $\Phi > 50°$ provide type 1 spectra.

4.3 Analysis

To characterize both the AGN and the host-galaxy we performed the SED-fitting of our sample.

It is worth noting that the SED-fitting results suffer from degeneracies and some parameters have very large uncertainties. The most important degeneracy is between the contributions of the star formation and of the AGN. With our number of photometric points, and the fact that we have at most five far-IR datapoints, it is difficult for the code to distinguish one contribution from the other. In particular, a typical emission from the AGN in the $10-20\,\mu$m range can be interpreted as due to a high contribution of the PAHs, hence, the AGN component might be underestimated and the SFR overestimated. This degeneracy can translate in large uncertainties on the relative contribution of the two components in some specific cases. It is primarily due to the photometric points we have at our disposal and could be overcome with higher resolution spectra (e.g. *Spitzer*/IRS).
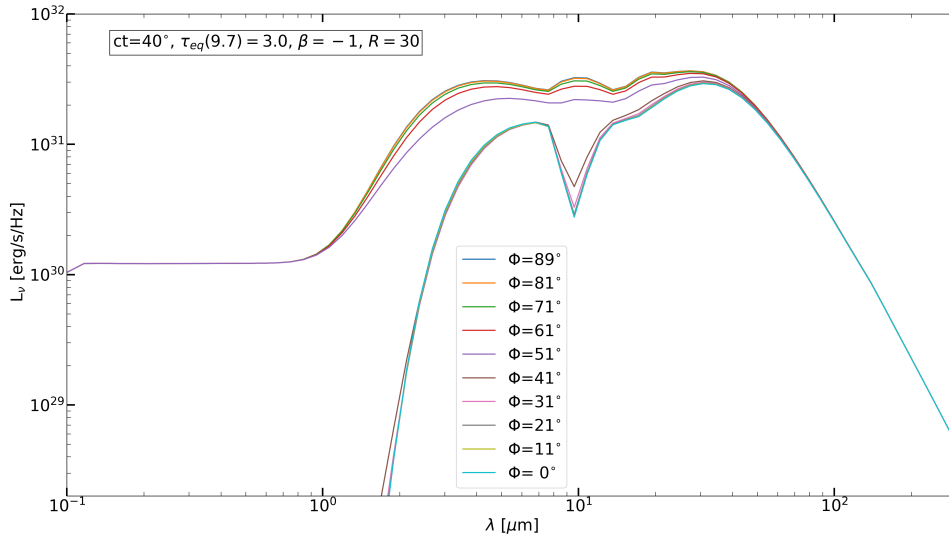
Figure 4.3: Spectra of a AGN/torus model for different inclination angles along the line of sight Φ. Torus parameter are: $R = 30$, $ct = 40°$, $\beta = -1$, $\gamma = 0$, $\tau_{\mathrm{eq}}(9.7) = 3.0$; see section 4.2.2 for their description. The models are normalized to have an accretion luminosity of the AGN of 10^{46} erg/s. It is easy to distinguish the models for which the line of sight intercepts the torus (the lower spectra) from those for which the nucleus is directly visible (the upper spectra). The former show the $\sim 9.7\,\mu$m silicate absorption feature, usually found in type 2 objects.

Another important degeneracy is that characterizing the torus parameters. Ad example, the same SED can be equally well fitted with a low optical depth torus seen *edge-on* (i.e. with the line of sight that intercepts the torus) or with higher optical depth and line of sight that does not intercept the torus (*face-on*). However, as showed by Pozzi et al. (2012), even with very different torus parameters, the best-fit AGN luminosity, and the other values derived from it, did not differ significantly.

The AGN properties we were interested in are: the mid-IR and accretion luminosity, the AGN fraction in the far-IR and the torus properties, like opening angle, inclination along the line of sight and optical depth. In particular, the accretion luminosity will also be used to allow a comparison with the intrinsic luminosity obtained from X-ray spectral analysis, with the aim of both testing the goodness of the X-ray analysis results and providing an estimate of the AGN bolometric power for the sources without X-ray detections. Moreover, from the $12\,\mu$m luminosity we will compute the $2-10$ keV luminosity, using the Gandhi et al. (2009) relation, and compare it with that obtained from the X-ray spectral analysis.

The SED-fitting procedure allows us to obtain the host-galaxy properties as well. We will compare the SFR provided by the SED-fitting code using the optical and NIR part of the SED with the one computed using the $8-1000\,\mu$m galaxy luminosity and provide clues on the BH-galaxy co-evolution scenario.

In section 4.3.1 we explain the torus library models used in the SED-fitting procedure. Then we present the SED-fitting results (sec 4.3.2). In section 4.4 we introduce and present the results of the AGN significance test.

4.3.1 The torus models

The complete library of Fritz and Feltre torus models is composed of $24\,000$ entries and for each of them a certain number of spectra are generated varying the model normalization, on the basis of the `n_ran_norm` parameter. To reduce the calculation time to an acceptable value, we decided to use only a subsample of the library, selecting only some models on the basis of physical reasons and simplicity.

From all the torus parameters presented in section 4.2.2 we choose:

- $\mathbf{\Phi = 1, 21, 41, 61, 89}$: to be able to model different inclination angles between the line of sight and the torus equatorial plane (i.e. to model both type 1 and type 2 objects).

- $\mathbf{R = 30}$: this value limits the models to compact tori of a few parsec (given that $R_{\min}$ is directly connected to the sublimation temperature and to the accretion luminosity of the central BH), as done in Pozzi et al. 2010. In fact, high-resolution IR and recent ALMA observations support a compact dust distribution in nearby luminous AGN (i.e. Jaffe et al. 2004, Elitzur 2008, Combes et al. 2019).

- **ct** $= 20°, 40°, 60°$: all the possible values of the half-width of the torus apertures.

- $\beta = \mathbf{0}, -\mathbf{1}$: the first is linked to an homogeneous density distribution, the second to a density decreasing exponentially with the distance from the nucleus.

- $\gamma = \mathbf{0}$: we consider only torus with an homogeneous distribution of density in polar direction.

- $\tau_{\mathrm{eq}} = \mathbf{0.1}, \mathbf{0.3}, \mathbf{0.6}, \mathbf{1}, \mathbf{3}, \mathbf{6}$: as suggested by Feltre (2012), we avoid extreme optical depths.

We instructed the SED-fitting code to run 100 different normalizations of the chosen 180 torus models, for a total of 18 000 AGN spectra used in the SED-fitting procedure.

4.3.2 SED-fitting results

As described in section 4.2.2, we used Bruzual (2007) and da Cunha et al. (2008) models to reproduce the galaxy emission and Fritz et al. (2006) and Feltre et al. (2012) models to take into account the AGN contributions. We report the main properties of the host-galaxies, as stellar mass and SFR, and of the AGN, as bolometric and $2 - 10$ keV rest-frame luminosities, with the aim of comparing them with the result of the X-ray spectral analysis.

The main results of the SED-fitting are reported in Table 4.1; in figures 4.4 and 4.5 we show two examples of SED. The SED-fitting decompositions of all the sources are shown in Appendix A and Appendix B.

AGN parameters

The best-fit torus model for 55% of the sources is an *edge-on* model, i.e. a model in which the line of sight intercepts the torus. The remaining 45% are best-fitted with a *face-on* model. However, the Probability Distribution Function (PDF) of the line-of-sight inclination angle Φ shows that Φ is never a well constrained parameter and usually the $1\,\sigma$ range contains numerous possible solutions. The point that some torus parameters are poorly constrained is related to the degeneracies among them, as explained in the beginning of section 4.3. However, these variations in the torus parameter do not affect significantly the luminosities obtained from the SED-fitting and we will rely on those to draw conclusions on the AGN properties.

The fact that nearly half of our sample was fitted with a *face-on* model is not a problem in the light of what discussed about the degeneracies and of the fact that the best-fit AGN luminosities are not highly influenced; nevertheless we made a SED-fitting run using only *edge-on* models, the results of which are reported in section 4.5.

78% of the sources have best-fit equatorial optical depth at $9.7\,\mu$m $\tau_{eq}(9.7) \le 0.6$, in particular 47% with $\tau_{eq}(9.7) = 0.6$. The other torus parameters have homogeneous value distributions, spanning all the available range of possibilities.

In figure 4.6 we show the PDF of four SED parameters for source 813850; as we can see, the torus ct and Φ are not well constrained. On the contrary, the SFR is well constrained.
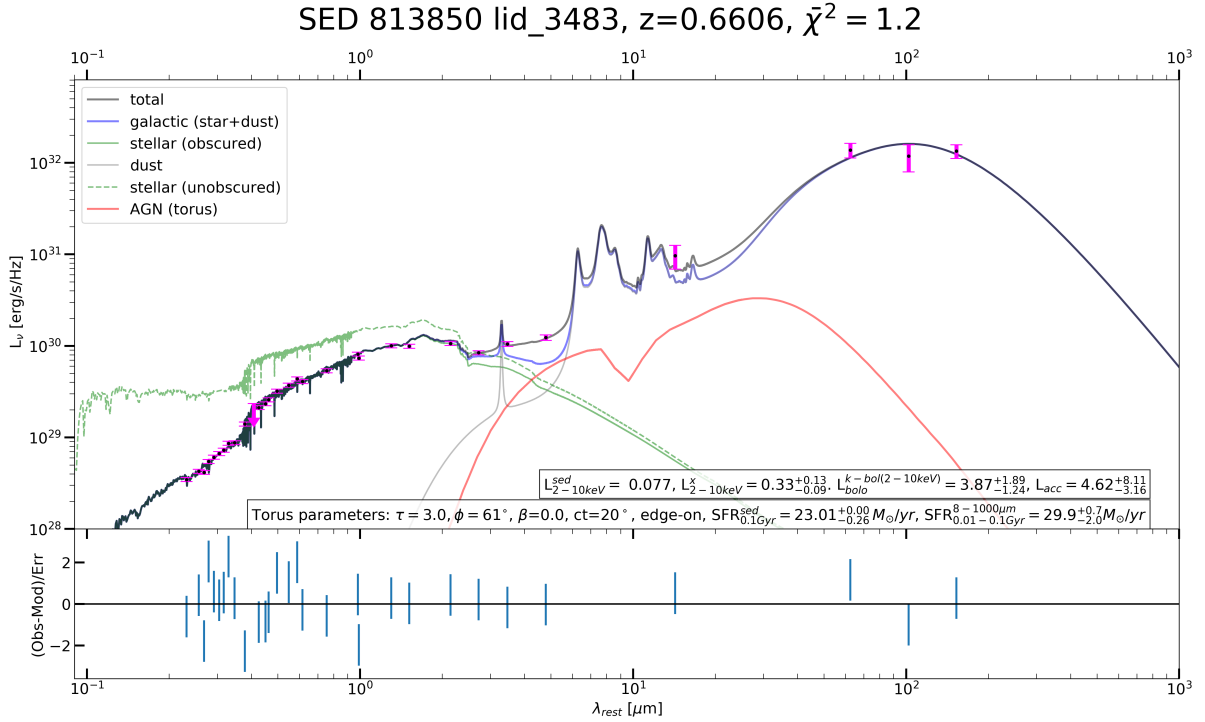

Figure 4.4: SED decomposition of source 813850 and residuals to the best-fitting solution. Data with $1\,\sigma$ confidence error are from the COSMOS2015 catalog (Laigle et al. 2016). The black line is the best-fit SED, the blue is the galactic contribution, which is composed of heated-dust emission (grey) and stellar emission (green). The green dashed line is the stellar contribution accounting for the dust extinction. The red line is the torus (AGN) emission. The reported $\bar{\chi}^2$ is the χ^2 divided by the number of photometric points (see section 4.4).

Stellar masses

The mean stellar mass of the sample is $M_* = (\,7.8 \pm 0.5\,) \cdot 10^{10}\,M_\odot$, with a median value of $7.6 \cdot 10^{10}\,M_\odot$. The stellar masses are well constrained by the SED-fitting procedure and the median of the relative errors is $\Delta M_*/M_* \approx 2\%$.

zID	M_* $\cdot 10^{10}\,M_\odot$	SFR $M_\odot/\mathrm{yr}$	f^{AGN} %	$L_{\mathrm{IR,AGN}}$ $\cdot 10^9\,L_\odot$	L_{bol} $\cdot 10^{44}\,\mathrm{erg/s}$	s_{AGN} σ
803886	$10.7^{+0.2}_{-4.5}$	$46.5^{+6.9}_{-6.0}$	$2.2^{+3.1}_{-1.4}$	$11.9^{+19.4}_{-7.8}$	$2.4^{+10.7}_{-1.5}$	2.7
803996	$9.5^{+0.2}_{-1.0}$	$38.2^{+3.2}_{-0.4}$	$14.96^{+0.71}_{-0.34}$	$78.5^{+5.6}_{-1.8}$	$24.3^{+1.7}_{-10.3}$	6.0
804237	$2.88^{+0.43}_{-0.19}$	$7.6^{+0.5}_{-5.8}$	$51.9^{+34.2}_{-1.2}$	$94.4^{+0.0}_{-6.3}$	$9.23^{+6.44}_{-0.62}$	7.6
804431	$1.51^{+0.26}_{-0.10}$	$3.2^{+3.1}_{-0.9}$	< 1.7	< 0.4	$0.04^{+0.12}_{-0.04}$	1.0
805117	$0.78^{+0.02}_{-0.12}$	$10.5^{+38.1}_{-0.2}$	$0.35^{+0.59}_{-0.26}$	$0.47^{+0.83}_{-0.25}$	$0.21^{+0.21}_{-0.12}$	0.7
807963	$8.91^{+0.01}_{-0.01}$	$58.48^{+0.10}_{-0.10}$	$0.19^{+0.12}_{-0.08}$	$1.36^{+0.90}_{-0.56}$	$0.43^{+0.01}_{-0.05}$	3.1
809056	$6.17^{+0.29}_{-0.54}$	$47.0^{+0.5}_{-1.1}$	< 0.2	< 1.0	< 0.4	1.9
809579	$7.59^{+0.18}_{-0.01}$	$18.07^{+0.42}_{-0.01}$	< 0.1	< 0.3	< 0.8	1.5
809597	$19.05^{+0.01}_{-0.01}$	$38.64^{+0.10}_{-0.01}$	$5.96^{+0.88}_{-0.65}$	$63.8^{+11.2}_{-6.9}$	$35.9^{+32.5}_{-19.9}$	8.4
810378	$20.0^{+0.9}_{-4.5}$	$55.8^{+16.1}_{-15.4}$	$8.8^{+5.8}_{-2.3}$	$78.5^{+35.0}_{-6.9}$	$10.6^{+0.8}_{-1.4}$	5.2
811284	$2.63^{+0.06}_{-0.44}$	$66.4^{+1.5}_{-52.5}$	$0.88^{+0.80}_{-0.39}$	$2.5^{+2.1}_{-1.1}$	$0.64^{+0.08}_{-0.08}$	2.6
811645	$3.39^{+0.33}_{-0.08}$	$4.75^{+0.28}_{-0.11}$	$0.33^{+0.36}_{-0.22}$	$0.19^{+0.19}_{-0.12}$	$0.11^{+0.04}_{-0.08}$	1.6
811887	$2.14^{+0.95}_{-0.10}$	$3.7^{+1.2}_{-0.1}$	$0.18^{+0.39}_{-0.15}$	$0.11^{+0.22}_{-0.09}$	$0.04^{+0.04}_{-0.03}$	2.5
812111	$2.57^{+0.82}_{-0.10}$	$29.3^{+0.1}_{-19.9}$	$0.70^{+0.80}_{-0.34}$	$1.68^{+1.24}_{-0.49}$	$1.50^{+0.18}_{-0.13}$	1.4
812193	$1.66^{+0.16}_{-0.07}$	$3.4^{+16.2}_{-0.1}$	$1.22^{+0.95}_{-0.94}$	$1.14^{+0.62}_{-0.45}$	$0.77^{+0.07}_{-0.60}$	1.1
812432	$3.89^{+0.18}_{-0.09}$	$23.3^{+8.5}_{-0.8}$	$42.2^{+1.0}_{-7.9}$	$192.8^{+0.1}_{-8.7}$	$17.58^{+0.41}_{-0.79}$	8.4
812665	$7.59^{+0.18}_{-0.01}$	$0.12^{+0.10}_{-0.01}$	$12.4^{+8.7}_{-6.1}$	$0.31^{+0.30}_{-0.16}$	$0.13^{+0.01}_{-0.01}$	–
812953	$5.25^{+0.51}_{-0.12}$	$3.52^{+0.10}_{-0.12}$	$38.5^{+1.8}_{-7.9}$	$44.2^{+2.1}_{-6.6}$	$8.8^{+1.3}_{-1.3}$	4.8
813250	$9.5^{+2.5}_{-1.4}$	$9.4^{+0.1}_{-3.3}$	$14.0^{+20.3}_{-6.6}$	$26.0^{+25.9}_{-13.8}$	$9.4^{+8.1}_{-6.9}$	2.9
813287	$7.9^{+3.0}_{-1.0}$	$24.7^{+3.0}_{-4.1}$	$1.08^{+0.63}_{-0.54}$	$2.6^{+1.8}_{-1.0}$	$1.50^{+0.11}_{-0.41}$	2.9
813366	$10.72^{+0.25}_{-0.01}$	$1.39^{+0.01}_{-0.01}$	< 0.1	< 0.7	< 0.1	–
813460	$1.26^{+0.65}_{-0.11}$	$4.7^{+5.8}_{-0.7}$	$1.33^{+0.68}_{-0.57}$	$0.77^{+0.34}_{-0.16}$	$0.64^{+0.08}_{-0.06}$	2.1
813850	$6.76^{+0.01}_{-0.15}$	$23.01^{+0.01}_{-0.26}$	$3.6^{+2.2}_{-1.2}$	$9.4^{+5.9}_{-3.3}$	$4.6^{+8.1}_{-3.2}$	3.7
814229	$1.55^{+0.23}_{-0.20}$	$3.78^{+0.41}_{-0.71}$	$2.1^{+1.8}_{-0.9}$	$0.79^{+1.01}_{-0.31}$	$0.46^{+0.15}_{-0.24}$	–
816439	$9.33^{+0.44}_{-0.01}$	$71.9^{+2.5}_{-0.1}$	$1.57^{+0.60}_{-0.71}$	$14.6^{+5.1}_{-6.9}$	$3.05^{+2.50}_{-1.38}$	1.7
817002	$7.76^{+0.01}_{-0.35}$	$61.2^{+0.7}_{-2.1}$	$12.7^{+0.3}_{-1.1}$	$92.3^{+8.9}_{-10.0}$	$15.3^{+10.7}_{-6.3}$	7.1
817871	$10.2^{+1.5}_{-0.7}$	$38.6^{+1.8}_{-11.3}$	$0.23^{+0.41}_{-0.13}$	$0.99^{+1.86}_{-0.60}$	$0.34^{+0.31}_{-0.02}$	–
817886	$7.59^{+0.93}_{-0.01}$	$34.4^{+1.2}_{-12.5}$	$0.18^{+0.14}_{-0.07}$	$0.75^{+0.58}_{-0.24}$	$0.61^{+0.03}_{-0.30}$	0.8
817977	$20.0^{+0.0}_{-1.3}$	$0.8^{+13.2}_{-0.1}$	$19.3^{+0.4}_{-10.9}$	$53.1^{+1.2}_{-16.4}$	$9.02^{+7.02}_{-0.60}$	5.3
818408	$7.59^{+0.36}_{-0.17}$	$48.6^{+1.7}_{-1.1}$	$0.37^{+0.13}_{-0.15}$	$2.54^{+0.89}_{-0.97}$	$0.82^{+1.20}_{-0.46}$	1.8
818478	$2.63^{+0.06}_{-0.23}$	$20.0^{+9.3}_{-0.5}$	< 0.1	< 0.2	< 0.1	1.1
819116	$3.39^{+0.16}_{-0.57}$	$3.48^{+0.25}_{-0.78}$	$1.5^{+2.0}_{-1.3}$	$0.54^{+0.57}_{-0.46}$	$0.17^{+0.20}_{-0.13}$	0.3
819306	$11.2^{+3.2}_{-0.1}$	$3.07^{+0.66}_{-0.10}$	< 0.5	< 0.4	< 0.2	1.3
819469	$4.68^{+0.11}_{-0.01}$	$27.99^{+0.32}_{-0.32}$	$0.4^{+0.2}_{-0.2}$	$1.43^{+0.78}_{-0.78}$	$0.26^{+0.02}_{-0.02}$	2.1
819927	$10.47^{+0.24}_{-0.24}$	$3.61^{+0.63}_{-0.08}$	$0.3^{+0.3}_{-0.1}$	$0.24^{+0.17}_{-0.09}$	$0.16^{+0.03}_{-0.03}$	–
820589	$12.88^{+0.01}_{-0.29}$	$38.19^{+0.44}_{-0.44}$	< 0.1	< 0.5	< 0.2	1.1

zID	M_* $\cdot 10^{10}\,M_\odot$	SFR $M_\odot/\mathrm{yr}$	f^{AGN} %	$L_{\mathrm{IR,AGN}}$ $\cdot 10^9\,L_\odot$	L_{bol} $\cdot 10^{44}\,\mathrm{erg/s}$	s_{AGN} σ
820695	$4.47^{+0.10}_{-0.49}$	$14.0^{+3.8}_{-2.6}$	< 0.4	< 0.6	< 0.1	0.7
820742	$12.6^{+1.5}_{-0.3}$	$9.0^{+4.0}_{-0.2}$	$46.2^{+1.1}_{-7.8}$	$171.8^{+4.0}_{-7.7}$	$15.67^{+0.36}_{-0.71}$	7.2
820983	$10.23^{+0.73}_{-0.68}$	$3.8^{+1.0}_{-1.9}$	$2.9^{+4.0}_{-1.4}$	$1.97^{+2.44}_{-0.94}$	$0.86^{+0.27}_{-0.16}$	1.5
822904	$15.85^{+0.01}_{-0.01}$	$0.91^{+0.01}_{-0.01}$	< 0.1	< 0.1	< 0.1	$-$
823097	$6.0^{+0.6}_{-1.2}$	$0.41^{+0.87}_{-0.01}$	$13.0^{+3.8}_{-5.4}$	$5.8^{+0.6}_{-1.9}$	$0.68^{+0.03}_{-0.02}$	1.5
823162	$4.07^{+0.01}_{-0.01}$	$10.05^{+0.01}_{-0.23}$	< 0.5	< 0.5	< 0.3	1.1
823537	$11.75^{+0.01}_{-0.01}$	$63.39^{+0.01}_{-0.01}$	< 0.1	< 0.1	< 0.1	$-$
824025	$4.68^{+0.01}_{-0.01}$	$5.09^{+0.06}_{-0.01}$	$29.2^{+0.1}_{-1.9}$	$37.6^{+0.0}_{-3.3}$	$3.43^{+2.39}_{-0.01}$	4.6
824548	$1.95^{+0.01}_{-0.01}$	$1.85^{+0.02}_{-0.01}$	$2.2^{+2.3}_{-1.5}$	$0.25^{+0.35}_{-0.17}$	$0.06^{+0.10}_{-0.03}$	1.2
824736	$6.31^{+0.15}_{-0.14}$	$37.76^{+18.09}_{-0.86}$	$6.7^{+4.2}_{-1.5}$	$29.9^{+41.8}_{-4.4}$	$9.0^{+7.8}_{-3.7}$	5.4
825282	$10.7^{+1.0}_{-0.2}$	$36.48^{+3.98}_{-0.83}$	$1.57^{+0.70}_{-0.43}$	$6.7^{+3.2}_{-1.7}$	$2.16^{+2.05}_{-0.86}$	1.8
825838	$7.8^{+1.2}_{-1.2}$	$19.6^{+2.9}_{-1.7}$	$0.18^{+0.22}_{-0.09}$	$0.45^{+0.45}_{-0.23}$	$0.23^{+0.14}_{-0.09}$	0.5
825958	$3.55^{+0.25}_{-0.16}$	$13.6^{+0.8}_{-3.6}$	$1.3^{+1.3}_{-0.5}$	$1.64^{+1.08}_{-0.61}$	$0.57^{+0.29}_{-0.10}$	3.1
826023	$23.44^{+0.01}_{-0.53}$	$65.61^{+0.76}_{-0.75}$	< 0.3	< 3.0	< 1.1	0.5
826095	$11.22^{+0.26}_{-0.01}$	$9.82^{+0.11}_{-0.22}$	$0.5^{+0.7}_{-0.3}$	$0.61^{+0.85}_{-0.42}$	$0.14^{+0.38}_{-0.03}$	1.8
826693	$1.45^{+0.03}_{-0.01}$	$6.95^{+0.50}_{-0.68}$	< 0.7	< 0.5	< 0.2	1.2
826908	$13.2^{+0.1}_{-2.7}$	$25.82^{+23.38}_{-0.30}$	$44.2^{+1.0}_{-33.1}$	$319.9^{+15.1}_{-201.0}$	$56.9^{+1.3}_{-46.0}$	4.9
829551	$15.5^{+0.1}_{-3.5}$	$5.3^{+8.7}_{-0.1}$	$0.05^{+0.06}_{-0.01}$	$0.19^{+0.23}_{-0.10}$	$0.09^{+0.06}_{-0.01}$	1.1
829938	$9.77^{+0.01}_{-0.22}$	$55.21^{+0.64}_{-0.63}$	$4.6^{+3.4}_{-2.4}$	$34.3^{+29.5}_{-18.2}$	$37.6^{+52.6}_{-28.4}$	1.4
829955	$8.51^{+0.01}_{-0.01}$	$89.54^{+0.01}_{-0.01}$	$0.57^{+0.01}_{-0.10}$	$9.44^{+0.01}_{-0.01}$	$2.99^{+0.14}_{-0.01}$	3.5
830027	$4.37^{+0.01}_{-0.10}$	$38.64^{+0.45}_{-0.88}$	$22.1^{+0.5}_{-6.8}$	$121.6^{+2.8}_{-46.6}$	$22.6^{+29.2}_{-1.5}$	5.0
831655	$3.89^{+0.58}_{-0.18}$	$26.4^{+7.2}_{-0.9}$	< 0.2	< 0.8	< 0.3	1.9
831966	$5.0^{+1.4}_{-0.8}$	$8.5^{+3.6}_{-3.4}$	$10.6^{+4.4}_{-3.1}$	$13.65^{+2.76}_{-0.61}$	$8.04^{+0.19}_{-0.36}$	3.5
832252	$0.70^{+0.01}_{-0.01}$	$6.95^{+0.08}_{-0.24}$	< 1.2	< 0.3	< 0.2	$-$
832576	$2.34^{+0.23}_{-0.11}$	$10.5^{+4.5}_{-4.0}$	< 0.3	< 0.3	< 0.1	$-$
832803	$18.62^{+0.01}_{-0.01}$	$33.27^{+0.39}_{-0.10}$	$24.27^{+0.57}_{-0.10}$	$192.8^{+4.5}_{-0.1}$	$23.17^{+1.09}_{-0.00}$	8.2
832900	$3.98^{+0.09}_{-0.18}$	$31.0^{+1.1}_{-3.7}$	$3.1^{+1.7}_{-0.9}$	$12.7^{+4.4}_{-4.1}$	$1.88^{+0.38}_{-0.17}$	3.5
832907	$10.72^{+0.25}_{-0.01}$	$19.82^{+0.23}_{-0.01}$	$3.7^{+2.3}_{-1.2}$	$12.4^{+8.7}_{-4.4}$	$2.26^{+4.57}_{-0.90}$	2.0
833208	$7.6^{+0.9}_{-1.3}$	$7.5^{+0.9}_{-3.9}$	$10.6^{+15.4}_{-4.5}$	$11.6^{+10.5}_{-3.8}$	$3.8^{+3.5}_{-1.7}$	6.2
833510	$19.50^{+0.10}_{-0.44}$	$31.41^{+0.36}_{-0.36}$	$4.3^{+0.3}_{-1.1}$	$22.6^{+1.6}_{-5.9}$	$6.4^{+5.5}_{-2.4}$	4.2
833904	$7.2^{+1.1}_{-0.2}$	$3.56^{+1.41}_{-0.73}$	$18.4^{+12.9}_{-8.1}$	$16.0^{+6.6}_{-5.7}$	$2.60^{+2.71}_{-0.63}$	4.3
834572	$17.4^{+0.1}_{-2.6}$	$11.53^{+10.96}_{-0.13}$	< 6.1	< 24.8	< 8.6	1.7
836036	$0.99^{+0.24}_{-0.01}$	$9.8^{+0.2}_{-7.0}$	$2.9^{+23.2}_{-0.2}$	$3.13^{+0.99}_{-0.01}$	$4.32^{+0.20}_{-0.10}$	2.0
836868	$5.25^{+0.12}_{-0.01}$	$13.87^{+0.16}_{-0.16}$	$7.9^{+2.5}_{-3.1}$	$18.0^{+5.7}_{-6.9}$	$4.2^{+21.2}_{-1.9}$	4.2
837072	$2.88^{+0.01}_{-0.07}$	$58.5^{+0.7}_{-5.1}$	$4.7^{+1.4}_{-1.5}$	$25.4^{+10.5}_{-8.2}$	$5.6^{+5.5}_{-2.1}$	2.9
837402	$9.55^{+0.01}_{-0.01}$	$11.14^{+0.10}_{-0.10}$	$1.0^{+0.1}_{-0.1}$	$9.66^{+0.69}_{-0.22}$	$6.0^{+0.0}_{-2.5}$	3.6
837589	$9.5^{+1.2}_{-1.2}$	$14.9^{+5.7}_{-3.1}$	< 0.1	< 0.1	< 0.1	$-$

zID	M_* $\cdot 10^{10}\,M_\odot$	SFR $M_\odot/\mathrm{yr}$	f^{AGN} %	$L_{\mathrm{IR,AGN}}$ $\cdot 10^9\,L_\odot$	L_{bol} $\cdot 10^{44}\,\mathrm{erg/s}$	s_{AGN} σ
837988	$15.14^{+0.71}_{-0.68}$	$5.6^{+0.1}_{-3.8}$	$4.4^{+5.2}_{-1.1}$	$7.5^{+1.3}_{-1.8}$	$2.99^{+1.9}_{-1.5}$	2.2
839683	$9.77^{+0.01}_{-0.01}$	$11.53^{+0.13}_{-0.01}$	$0.56^{+0.41}_{-0.23}$	$1.11^{+0.86}_{-0.46}$	$0.7^{+0.03}_{-0.04}$	2.1
839719	$7.9^{+1.6}_{-0.2}$	$5.8^{+4.8}_{-0.2}$	$0.31^{+1.37}_{-0.28}$	$0.29^{+0.96}_{-0.26}$	$0.1^{+0.39}_{-0.07}$	−
840085	$10.5^{+0.1}_{-2.3}$	$41.9^{+1.5}_{-0.5}$	$3.27^{+0.32}_{-0.79}$	$16.41^{+2.00}_{-3.96}$	$3.51^{+6.15}_{-0.59}$	4.0
840744	$3.98^{+0.19}_{-0.18}$	$24.7^{+7.8}_{-1.4}$	$2.7^{+1.4}_{-1.6}$	$7.7^{+3.7}_{-4.5}$	$3.35^{+0.32}_{-0.29}$	3.7
841281	$11.2^{+0.3}_{-5.5}$	$10.3^{+0.2}_{-6.4}$	$43.2^{+2.0}_{-18.9}$	$96.6^{+4.6}_{-53.5}$	$16.79^{+9.82}_{-0.76}$	7.5
841340	$6.03^{+0.14}_{-0.14}$	$42.9^{+16.3}_{-6.4}$	$16.0^{+3.2}_{-4.4}$	$88.1^{+6.3}_{-4.0}$	$27.2^{+1.9}_{-10.0}$	4.1
841734	$7.24^{+0.10}_{-0.33}$	$67.1^{+0.1}_{-3.0}$	$10.12^{+0.72}_{-0.10}$	$110.92^{+5.23}_{-0.00}$	$18.41^{+0.87}_{-0.01}$	8.4
843107	$8.5^{+2.0}_{-2.9}$	$1.5^{+4.2}_{-1.0}$	$39.4^{+6.9}_{-16.7}$	$32.0^{+0.7}_{-10.4}$	$9.66^{+0.23}_{-0.64}$	3.0
844011	$2.19^{+0.05}_{-0.10}$	$1.31^{+0.10}_{-0.10}$	$0.92^{+0.88}_{-0.44}$	$0.24^{+0.22}_{-0.12}$	$0.13^{+0.02}_{-0.02}$	1.2
845677	$3.39^{+0.00}_{-0.10}$	$4.44^{+0.01}_{-0.10}$	< 0.1	< 0.1	< 0.1	−
846342	$15.14^{+1.85}_{-0.34}$	$5.5^{+0.1}_{-1.6}$	$21.6^{+10.4}_{-6.7}$	$51.9^{+7.7}_{-20.6}$	$11.4^{+2.0}_{-1.9}$	4.2
846478	$17.4^{+4.5}_{-1.9}$	$18.1^{+7.5}_{-9.1}$	$17.6^{+21.8}_{-5.4}$	$70.0^{+6.8}_{-16.9}$	$12.4^{+8.7}_{-5.1}$	5.2
846722	$5.62^{+0.13}_{-0.25}$	$4.65^{+0.11}_{-1.78}$	$1.16^{+1.96}_{-0.46}$	$1.01^{+0.71}_{-0.39}$	$0.62^{+0.09}_{-0.08}$	1.0
846946	$8.13^{+0.19}_{-0.01}$	$1.15^{+0.48}_{-0.01}$	$47.3^{+4.6}_{-15.3}$	$22.1^{+5.7}_{-7.5}$	$4.8^{+1.1}_{-2.7}$	1.5
847446	$4.47^{+0.01}_{-0.01}$	$32.9^{+0.1}_{-1.1}$	< 0.4	$0.33^{+1.06}_{-0.28}$	$0.08^{+0.30}_{-0.03}$	1.5
847932	$0.61^{+0.01}_{-0.01}$	$2.47^{+0.90}_{-0.16}$	$0.70^{+0.80}_{-0.48}$	$0.14^{+0.19}_{-0.09}$	$0.07^{+0.07}_{-0.05}$	−
850792	$2.00^{+0.01}_{-0.01}$	$3.33^{+0.12}_{-0.11}$	$2.2^{+1.0}_{-0.7}$	$1.76^{+0.96}_{-0.57}$	$0.72^{+0.07}_{-0.05}$	2.1
851740	$9.5^{+3.6}_{-0.2}$	$39.5^{+0.5}_{-7.8}$	$0.18^{+0.21}_{-0.10}$	$0.90^{+1.12}_{-0.52}$	$0.39^{+0.53}_{-0.07}$	−
900121	$4.90^{+0.11}_{-0.33}$	$58.5^{+11.8}_{-9.3}$	$2.1^{+1.3}_{-0.2}$	$16.4^{+10.8}_{-2.4}$	$1.88^{+2.05}_{-0.20}$	2.9
910023	$8.5^{+1.0}_{-0.1}$	$27.7^{+1.6}_{-0.1}$	$0.46^{+0.30}_{-0.11}$	$1.76^{+1.09}_{-0.45}$	$0.52^{+0.62}_{-0.15}$	−

Table 4.1: Main results of the optical-IR SED-fitting. zID: zCOSMOS source ID; M_*: best-fit stellar mass of the galaxy in unit of $10^{10}\,M_\odot$; SFR: best-fit star formation rate mediated in the last 0.01 - 0.1 Gyr in $M_\odot/\mathrm{yr}$ (derived through the modeling of the stellar emission in the UV-to-NIR regime with a Chabrier IMF); f^{AGN}: ratio between the $8 - 1000\,\mu\mathrm{m}$ IR luminosities of the galaxy and that of the AGN; $L_{\mathrm{IR,AGN}}$: best-fit $8-1000\,\mu\mathrm{m}$ AGN luminosity, in units of $10^9\,L_\odot$; L_{bol}: best-fit AGN bolometric luminosity, in units of $10^{44}\,\mathrm{erg/s}$; s_{AGN}: AGN significance, in units of σ, computed via an F-test of the best-fit models with and without the AGN component; if a value is not reported, the model without AGN provides a better solution than the model including the AGN component (see section 4.4).
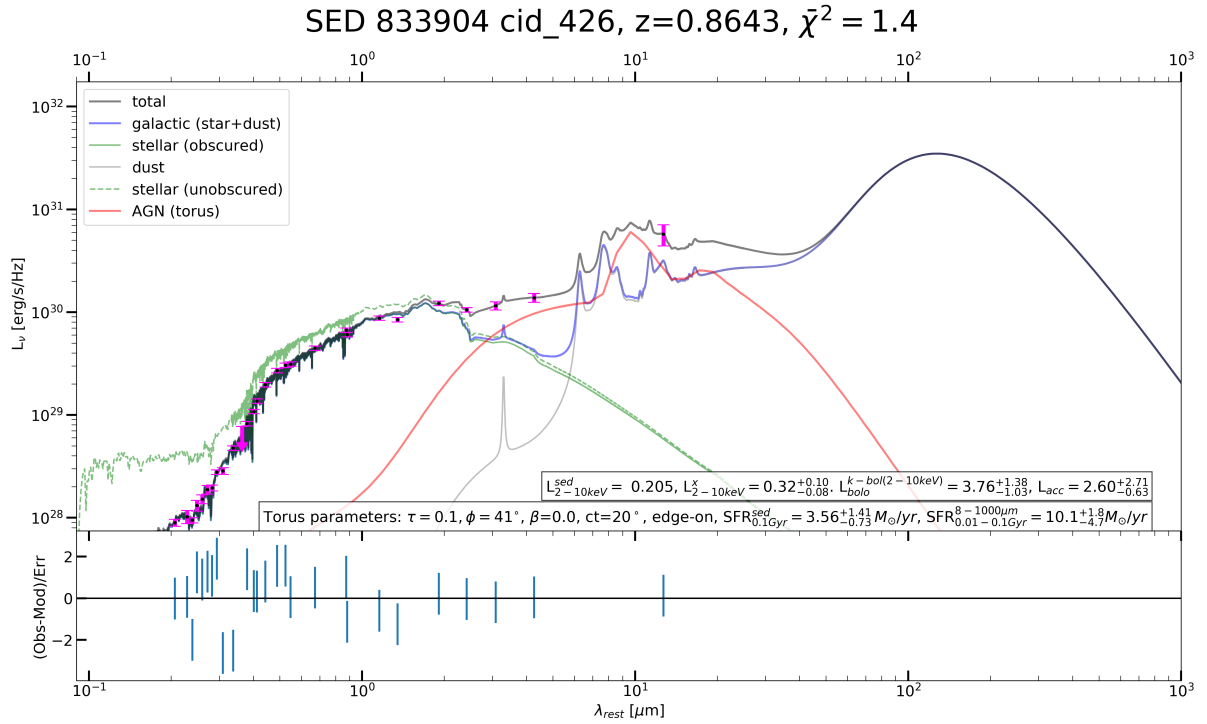
Figure 4.5: SED decomposition of source 833904 and residuals to the best-fitting solution. Data with 1σ confidence error are from the COSMOS2015 catalog (Laigle et al. 2016). The black line is the best-fit SED, the blue is the galactic contribution, which is composed of heated-dust emission (grey) and stellar emission (green). The green dashed line is the stellar contribution accounting for the dust extinction. The red line is the torus (AGN) emission. The reported $\bar{\chi}^2$ is the χ^2 divided by the number of photometric points (see section 4.4).
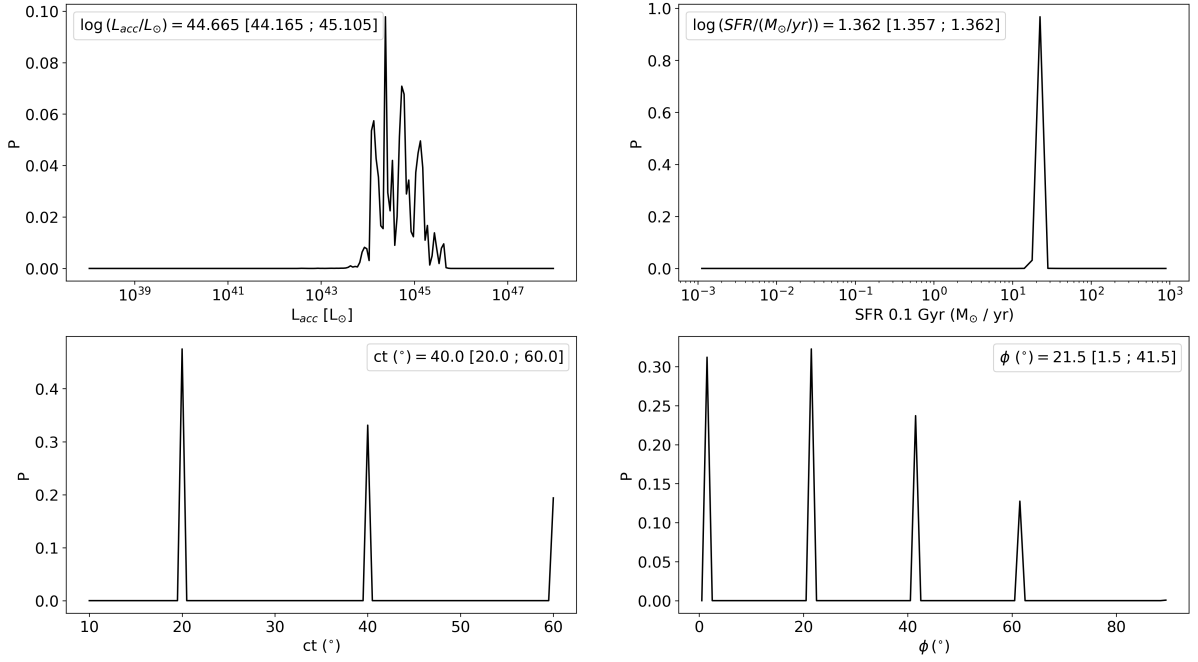
Figure 4.6: Probability distribution functions of the best-fit solution for source 813850. Top left: PDF of the AGN bolometric luminosity; top right: PDF of the SFR, obtained from the optical-NIR emission; bottom left: PDF of the torus ct parameter, the half width of the torus "hole"; bottom right: PDF related to the angle of the line of sight with respect to the torus equatorial plane. All values are reported with the associated $1\,\sigma$ confidence limit. As we can see, the SFR is a well-constrained parameter, while the AGN ct and Φ are not and span with equal probability a large range of their possible values.

The X-ray detected sources tend to be restricted to higher stellar masses: only 10% of the X-ray detected has $M_* < 3.5 \cdot 10^{10}\,M_\odot$, while 33% for the X-ray undetected.

Star formation rates

The SFR of our sample was obtained in two different ways: using the best-fit model (we will refer to it as SFR^{sed}) and using the $8 - 1000\,\mu m$ SF luminosity, which will be referred as $SFR^{8-1000\mu m}$.

The SFR^{sed} is the mean SFR of the last 0.01 - 0.1 Gyr as obtained from the modeling of the stellar component in the UV-to-NIR regime with *sed3fit*. As discussed in section 4.2.2 the code uses the UV-optical-NIR library of Bruzual (2007), that produced the optical-to-NIR spectra, by considering the spectral evolution of stellar populations at ages between 10^5 and $2 \cdot 10^{10}$ years, for different metallicities and star formation histories and assuming a Chabrier IMF (Chabrier 2003). We obtained a mean $SFR^{sed} = (22.3 \pm 2.2)\,M_\odot/yr$, with a median relative error of $\Delta SFR/SFR \approx 4\%$.

The $SFR^{8-1000\mu m}$ is the SFR averaged over the last 100 Myr computed by the emission of dust heated by young stars as well as of evolved stellar populations. It was derived from the IR luminosity, once the AGN contribution is removed, integrated in the rest-frame wavelength range $8 - 1000\,\mu m$, assuming the Kennicutt (1998b) relation:

$$SFR^{8-1000\mu m}\,(M_\odot/yr) = 4.5 \cdot 10^{44}\,L_{8-1000\mu m}\,(erg/s) \qquad (4.4)$$

We used the relation

$$SFR_{Chabrier} = 0.67 \cdot SFR_{Salpeter} \qquad (4.5)$$

to convert the Kennicutt (1998b) relation, which was computed with a Salpeter IMF, to a Chabrier IMF. This allowed us to compare the $SFR^{8-1000\mu m}$ with the SFR^{sed}. The mean SFR is $SFR^{8-1000\mu m} = (\,37.1 \pm 3.6\,)\,M_\odot/yr$.

In figure 4.7 we compare the two SFR values for each source. Because the $SFR^{8-1000\mu m}$ is heavily dependent on the fitting of the FIR band, the reliability of this value is linked to the accuracy at which the far-IR is reproduced. Unfortunately, nearly half of our sample has no FIR detection. As we can see from figure 4.7, the sources for which the two values are very similar are those with more FIR photometric points.

On average, the SFR^{sed} is 65% of the $SFR^{8-1000\mu m}$; this difference can have a double explanation. On the one hand, the SFR^{sed} can be underestimate due to a not-well-modeled dust extinction in the optical-NIR band of the SED; on the other hand, the $SFR^{8-1000\mu m}$ can be overestimated due to the contribution of old populations to the SED FIR (Lo Faro et al. 2013).

Only one source ($\approx 3\%$) of the X-ray detected sample has a $SFR^{8-1000\mu m} < 5\,M_\odot/yr$, in contrast with the nine sources ($\approx 15\%$) of the X-ray undetected sample; however, we cannot draw any conclusion on the issue on the basis of the available data.
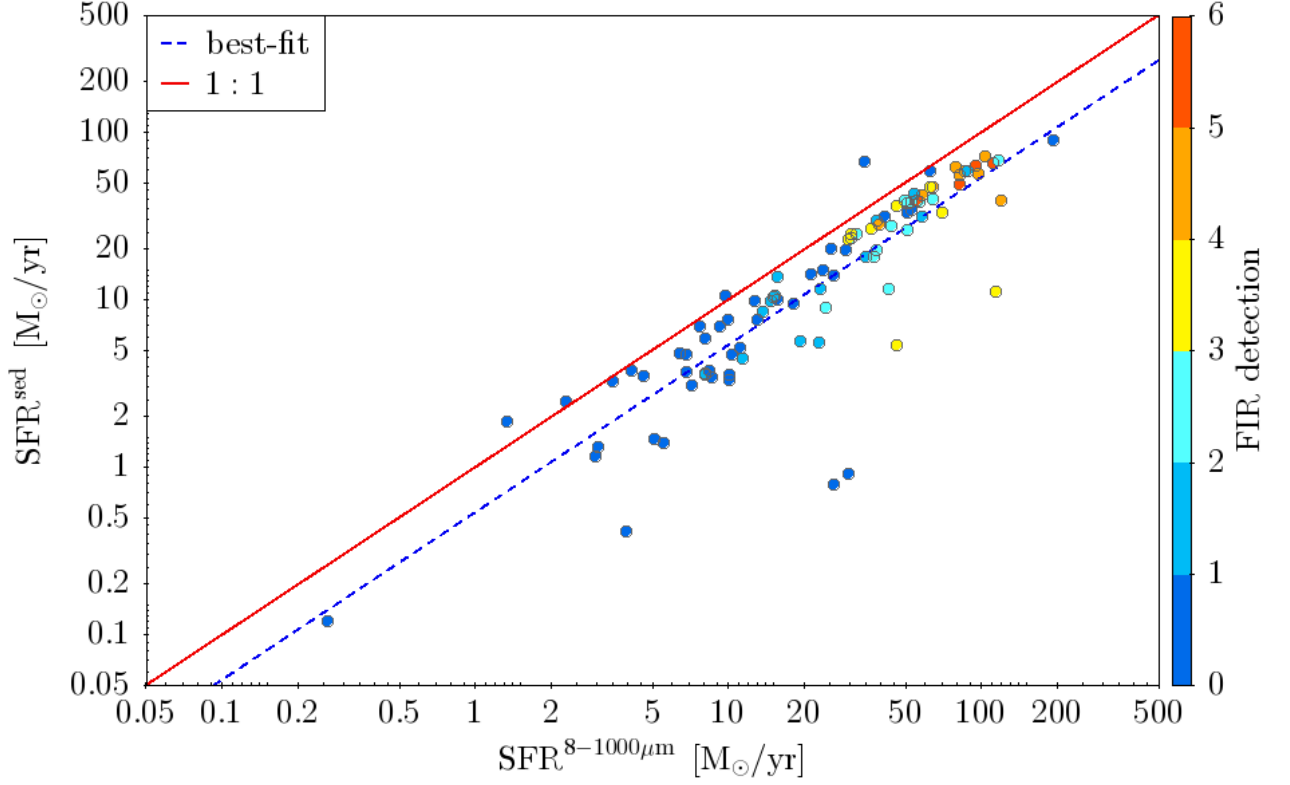
Figure 4.7: Comparison between the SFR obtained from the optical-NIR bands with those from FIR. SFR^{sed} are derived through the modeling of the stellar emission in the UV-to-NIR; $SFR^{8-1000\mu m}$ from the IR emission integrated in the rest-frame wavelength range $8 - 1000\,\mu m$ assuming the Kennicutt (1998b) SFR calibration converted to a Chabrier (2003) IMF. The color code indicates the number of photometric points available for each source in the FIR band. A low number of FIR detections may influence the goodness of the FIR SED-fitting, hence the $SFR^{8-1000\mu m}$. The red line is a 1:1 line; the blue line is the best-fit line with a slope of $m = 0.53$ and $c = 2.6\,M_\odot/yr$, in the $SFR^{sed} = c + m\,SFR^{8-1000\mu m}$ notation.

SFR-M$_*$ relation

Once stellar masses and SFRs were estimated, we have investigated whether our sources lie within the SFR-M$_*$ correlation called "main sequence" (Noeske et al. 2007). In fact, for the majority of the "normal" galaxies the SFR is tightly related to the stellar mass. Only outliers above the SFR–M$_*$ correlation are the "starburst" galaxies.

We used the Schreiber et al. (2015) correlation, with the aim of investigating whether our AGN are in different galaxies with respect to the "normal" galaxies. The Schreiber et al. main sequence SFR (SFR$_{\mathrm{MS}}$) is a function of both the stellar mass and the redshift:

$$\log\left(\mathrm{SFR}_{\mathrm{MS}}\,[\mathrm{M}_\odot/\mathrm{yr}]\right) = m - m_0 + a_0 r - a_1[\max\left(0, m - m_1 - a_2 r\right)]^2 \qquad (4.6)$$

where $r \equiv \log\left(1+z\right)$, $m \equiv \log\left(\mathrm{M}_*/10^9\mathrm{M}_\odot\right)$, $m_0 = 0.5 \pm 0.07$, $a_0 = 1.5 \pm 0.15$, $a_1 = 0.3 \pm 0.08$, $m_1 = 0.36 \pm 0.3$ and $a_2 = 2.5 \pm 0.6$.

We obtained a mean SFR$_{\mathrm{MS}} = (\,34.2 \pm 1.6\,)\,\mathrm{M}_\odot/\mathrm{yr}$ and a median of $33.5\,\mathrm{M}_\odot/\mathrm{yr}$.

We compared the main sequence SFR with both the SFR from the UV-optical-NIR (SFR$^{\mathrm{sed}}$) and from the FIR (SFR$^{8-1000\mu\mathrm{m}}$). The mean ratios between the three values of SFR are: SFR$^{\mathrm{sed}}$/SFR$_{\mathrm{MS}} = 0.68 \pm 0.06$ and SFR$^{8-1000\mu\mathrm{m}}$/SFR$_{\mathrm{MS}} = 1.04 \pm 0.08$. As we noted in the previous section, the SFR from the optical-NIR are a bit lower than those from the FIR, and in this case, also with respect to the main sequence SFR.

In addition, as we can see from figure 4.8, the number of FIR photometric point plays a significant role in the fitting of the SED, hence in the estimate of the SFR. In the figure we display the SFR-M$_*$ correlation as computed by Schreiber et al. (2015) for $z \approx 1$ and the SFR we obtained via the IR luminosity. All the 35 sources (except one) with ≥ 2 photometric detections in the FIR lies within the $1\,\sigma$ limit of the SFR-M$_*$ correlation. Moreover, these sources tend to have SFR slightly higher than the main sequence SFR, as their mean ratio is SFR$^{8-1000\mu\mathrm{m}}$/SFR$_{\mathrm{MS}} = 1.5 \pm 0.1$.

IR8 relation

To confirm the goodness of the galaxy SED-fitting, we investigated if the best-fit galaxy SED is able to reproduced the "IR8" relation (Elbaz et al. 2011). This is a scaling relation between the $8 - 1000\,\mu\mathrm{m}$ galaxy luminosity and the $8\,\mu\mathrm{m}$ galaxy luminosity, which is defined as $\mathrm{L}_8 = \nu\mathrm{L}_\nu\,(8\,\mu\mathrm{m})$. The IR8 ratio is

$$\mathrm{IR8} = \frac{\mathrm{L}_{\mathrm{IR}}^{\mathrm{gal}}}{\mathrm{L}_8^{\mathrm{gal}}} \qquad (4.7)$$

and for star forming galaxies its mean value is IR8 $= 4.9\,[-2.2, +2.9]$, with $1\,\sigma$ confidence (Elbaz et al. 2011). This correlation is based on the SF origin of both the $8\,\mu\mathrm{m}$ and the $8 - 1000\,\mu\mathrm{m}$ luminosities. In fact, the first is linked to PAH emission, the second to the UV radiation absorbed and re-emitted by the dust in the far-IR bands. Both can be used as SFR tracers.
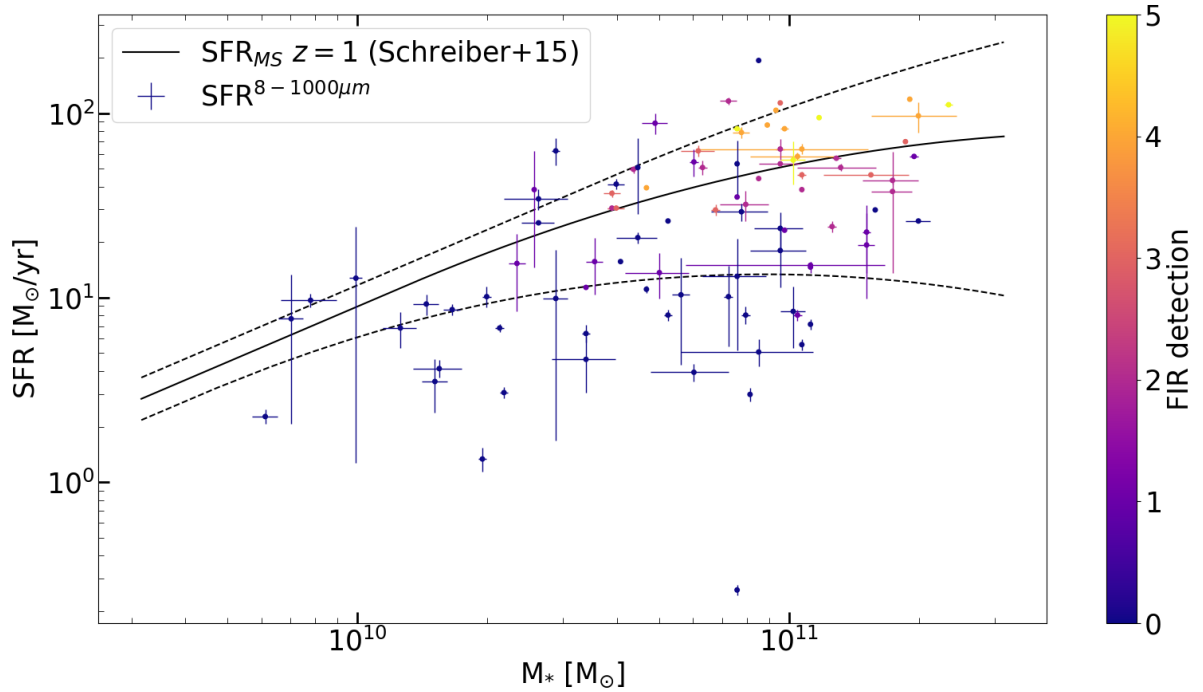
Figure 4.8: Comparison of our SFR, obtained through the galaxy IR luminosity, with the SFR-M$_*$ relation of Schreiber et al. (2015) at $z \approx 1$. SFR$^{8-1000\mu\mathrm{m}}$ is the SFR obtained from the $8-1000\,\mu m$ luminosity assuming the Kennicutt (1998b) SFR calibration converted to a Chabrier (2003) IMF. The color code indicates the number of far-IR detections. Black lines indicate the SFR expected for the SFR-M$_*$ relation of Schreiber et al. (solid) and its $1\,\sigma$ confidence limit (dashed). With the exception of one source, all those having at least two FIR detections lie within $1\,\sigma$ of the "main sequence". The majority of them are in the upper envelope of the Schreiber et al. nominal best solution.

In figure 4.9 we show that the majority of our sample lies within the $1\,\sigma$ limit. Moreover, the most distant sources are those with few FIR datapoints.

These results confirm the goodness of the galaxy SED-fitting and underline the importance of FIR detections in constraining the IR SED and thus in separating the AGN emission from that of the galaxy.
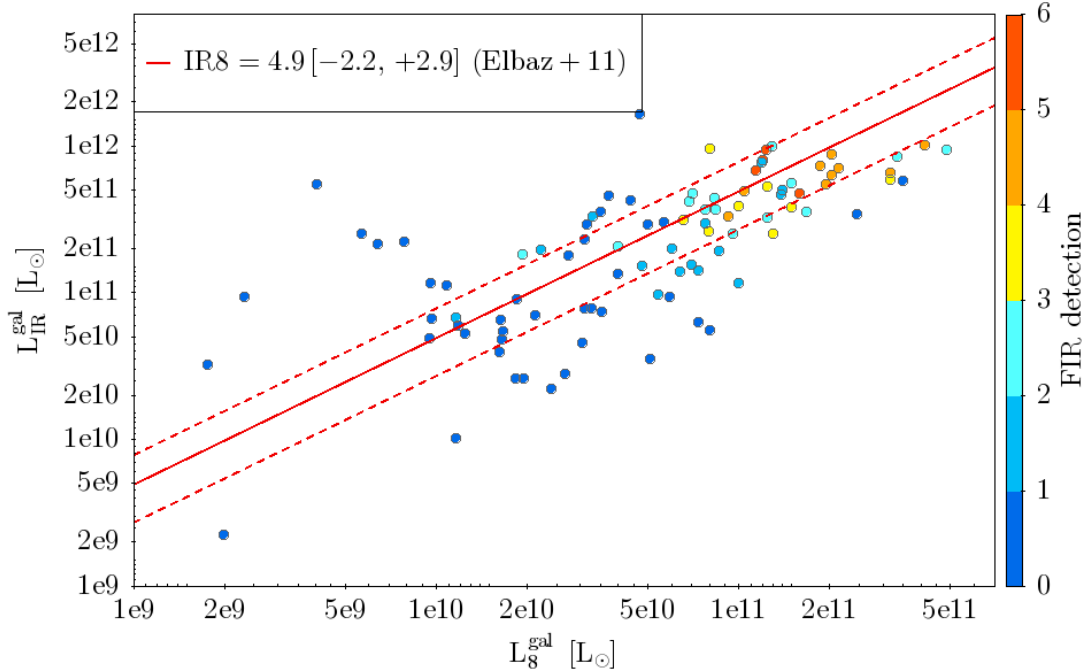

Figure 4.9: Comparison between the galaxy $8-1000\,\mu$m luminosity and the L_8 luminosity. L_8 is the galaxy $8\,\mu$m luminosity $L_8 = \nu L_\nu\,(8\,\mu m)$. The color code indicates the number of photometric points available for each source in the FIR band. The solid red line is the mean IR8 (IR8= L_{IR}^{gal}/L_8^{gal}) for star-forming galaxy (Elbaz et al. 2011); the dashed red lines are its $1\,\sigma$ limit.

AGN IR luminosities and AGN IR fractions

One of the output of the SED-fitting code is the $8 - 1000\,\mu$m AGN luminosity. For eight sources we obtained only an upper limit on this value, because their best-fit SED does not need any contribution from the AGN. Except for source 823537, they have few FIR detections: two sources (832576 and 845677) have only one FIR detection each, five sources (818478, 837589, 823162, 822904 and 813366) have no FIR detection. Moreover, all the sources are not detected in the X-ray band. We explained this apparent lack of AGN component (apparent because we know that these sources do have an AGN, being the selection method based on the presence of AGN spectral features) as related

to the fact that these source may have AGN with lower luminosity and their emission is overwhelmed by the galaxy radiation. Surely, the few photometric points we have available in the mid-IR, where the obscured AGN emission peaks, play a significant role in constraining the AGN component.

Without considering these sources, the mean $8-1000\,\mu m$ AGN luminosity is $L_{8-1000\mu m} = (\,2.8\pm0.6\,)\cdot10^{10}\,L_{\odot}$ and a median of $3.1\cdot10^{9}\,L_{\odot}$. The mean AGN fraction, obtained from the ratio between the AGN and the total luminosity (both in the $8-1000\,\mu m$ wavelength range) is $f_{8-1000\mu m}^{AGN} = 0.08 \pm 0.01$.

Without considering the upper limits, twenty-four sources ($\approx 48\%$) of the X-ray undetected sample have AGN IR luminosity $< 10^{9}\,L_{\odot}$. As comparison, only three sources ($\approx 9\%$) among the X-ray detected sample has similar luminosities. This supports the fact that the X-ray undetected sources are AGN with lower luminosities, as mentioned in section 3.4.

Bolometric luminosities

Unlike type 1 objects, for obscured AGN it is not possible to obtain the AGN bolometric luminosity from the optical emission. However, the integration of the whole AGN SED, in particular the IR emission, let us obtain the AGN bolometric luminosity. In fact, one of the direct outputs of the fitting algorithm is the AGN bolometric luminosity, derived via the integration of the spectrum of the central source that illuminates the torus (see section 4.2.2), once the best-fit torus components and its normalization are found.

The SEDs of eight sources are best-fitted without any contribution from the AGN, hence these sources have only upper-limits on their AGN bolometric luminosities. In addition, 10 sources have their AGN bolometric lower limits compatible with zero, hence we reported their AGN bolometric luminosities as upper limit. The remaining 76 sources have a mean $L_{bol}^{sed} = (\,6.5 \pm 1.2\,)\cdot10^{44}$ erg/s.

To further support these values, we compared them with the bolometric luminosities obtained from the X-ray spectral analysis. We will refer to the bolometric luminosities computed from the SED-fitting as L_{bol}^{sed} and to those obtained from X-ray analysis as L_{bol}^{x}.

For the sources with X-ray detection we were able to compute the intrinsic $2-10$ keV rest-frame luminosity, as reported in section 3.3.5. Using the bolometric correction K_{bol} from Lusso et al. (2012), we obtained the AGN bolometric luminosities L_{bol}^{x}. In Lusso et al. (2012) the $K_{bol} - L_{bol}$ relation was derived using a sample of 929 X-ray selected AGN in the COSMOS field, using UV-to-FIR data to obtain the bolometric luminosities and XMM-*Newton* observations to compute the $2-10$ keV intrinsic luminosities. The K_{bol} is:

$$log(K_{bol}) = 0.230x + 0.050x^2 + 0.001x^3 + 1.256 \qquad (4.8)$$

where $x = \log{(L_{bol}/L_\odot)} - 12$. We obtained the bolometric luminosity from

$$L^x_{bol} = K_{bol} \cdot \left(\frac{L_{2-10keV}}{L_\odot} \right) \, L_\odot \qquad (4.9)$$

The mean AGN bolometric luminosity obtained from the $2-10$ keV intrinsic luminosity is $L^x_{bol} = (\,7.9 \pm 1.7\,) \cdot 10^{44}$ erg/s and the median $4.9 \cdot 10^{44}$ erg/s. The mean ratio between L^{sed}_{bol} and L^x_{bol} is 2.8 ± 0.8. The correlation is sufficiently good, considering the uncertainties both in the data and in the $K_{bol} - L_{bol}$ relation.

In figure 4.10 we show the comparison of the bolometric luminosities. Except for four sources, the two bolometric luminosities are compatible within 2 times their errors. This correlation is extremely important, because allows to obtain an estimate of the AGN bolometric luminosities using only optical-to-FIR photometric data.
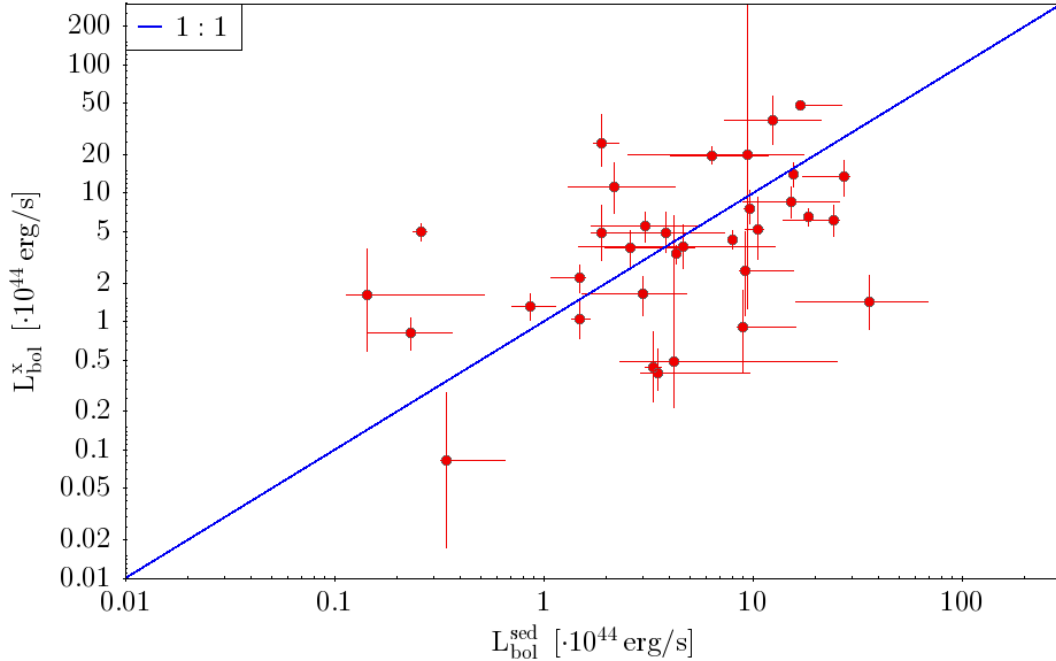

Figure 4.10: Comparison of the AGN bolometric luminosities obtained from the SED-fitting (L^{sed}_{bol}) and from X-ray spectral analysis (L^x_{bol}). The L^x_{bol} were computed from the $2-10$ keV rest-frame intrinsic luminosities using the Lusso et al. (2012) bolometric correction.

Estimate of the $2-10$ keV intrinsic luminosities

We obtained an independent estimate of the AGN $2-10$ keV rest-frame intrinsic luminosity from the AGN $12\,\mu$m luminosity using the Gandhi et al. (2009) relation:

$$\log\left(\frac{\mathrm{L}^{sed}_{2-10\text{ keV}}}{10^{43}\text{ erg/s}}\right) = \frac{1}{0.97}\left(\log\left(\frac{\mathrm{L}^{sed}_{12\mu m}}{10^{43}\text{ erg/s}}\right) - 0.33\right) \qquad (4.10)$$

This relation was found via a sample of 42 Seyfert, including both type 1 and type 2 AGN, observed with the *VLT*/VISIR with sufficient angular resolution to isolate the AGN $12\,\mu$m emission from that of the galaxy. This correlation is due to the fact that the AGN intrinsic emission is absorbed and re-emitted by the obscuring torus in the mid-IR bands.

For three sources the best-fit model has AGN contributions so low that we were not able to compute their AGN $12\,\mu$m luminosity. Without these sources, the mean $2-10$ keV intrinsic luminosity is $\mathrm{L}^{sed}_{2-10\text{keV}} = (\,1.9 \pm 0.4\,) \cdot 10^{43}$ erg/s and the median $0.4 \cdot 10^{43}$ erg/s.

We compared these luminosities with those from the X-ray spectral analysis. For the X-ray detected sources we obtain a mean of $\mathrm{L}^{x}_{2-10\text{keV}} = (\,5.4 \pm 1.0\,) \cdot 10^{43}$ erg/s.

For the X-ray undetected sources we did not have their intrinsic luminosity from X-ray spectral analysis. However, we used the rest-frame $2-10$ keV flux upper limits. To compute those we assumed a power-law model with $\Gamma = 0.41$ (section 3.4.2) and derived upper limits on the $2-10$ keV intrinsic luminosity, as showed in section 3.4.2. In figure 4.11 we show the comparison between the AGN rest-frame $2-100$ keV intrinsic luminosities obtained from the AGN $12\,\mu$m luminosities with those from the X-ray spectral analysis (including also the intrinsic luminosity upper limits, computed as stated above). For the data derived from X-ray analysis there is a clear separation between the detections and the upper limits, with the former populating an area with $\mathrm{L}^{x}_{2-10\text{keV}} > 10^{43}$ erg/s and the latter restricted to $\mathrm{L}^{x}_{2-10\text{keV}} < 10^{43}$ erg/s. A similar separation is not present in the intrinsic luminosities derived from the SED-fitting.

The mean ratio between the $\mathrm{L}^{sed}_{2-10\text{keV}}$ and the $\mathrm{L}^{x}_{2-10\text{keV}}$, without considering the upper limits, is $\approx 1.0 \pm 0.2$ and its median is ≈ 0.3. Similar to the correlation between the bolometric luminosities, this one allows to estimate the AGN power, using only optical-to-FIR photometric data. The use of both the correlations can be an extremely valuable aid in computing AGN luminosities when X-ray observations are not available.

4.3.3 "Peculiar" sources

A visual inspection of the SED-fitting results indicates that for three sources (809597, 910023 and 845677) the FIR SEDs are not well fitted. We ascribed this to the fact that *sed3fit* weight the optical/NIR data points more than the far-IR given the higher number
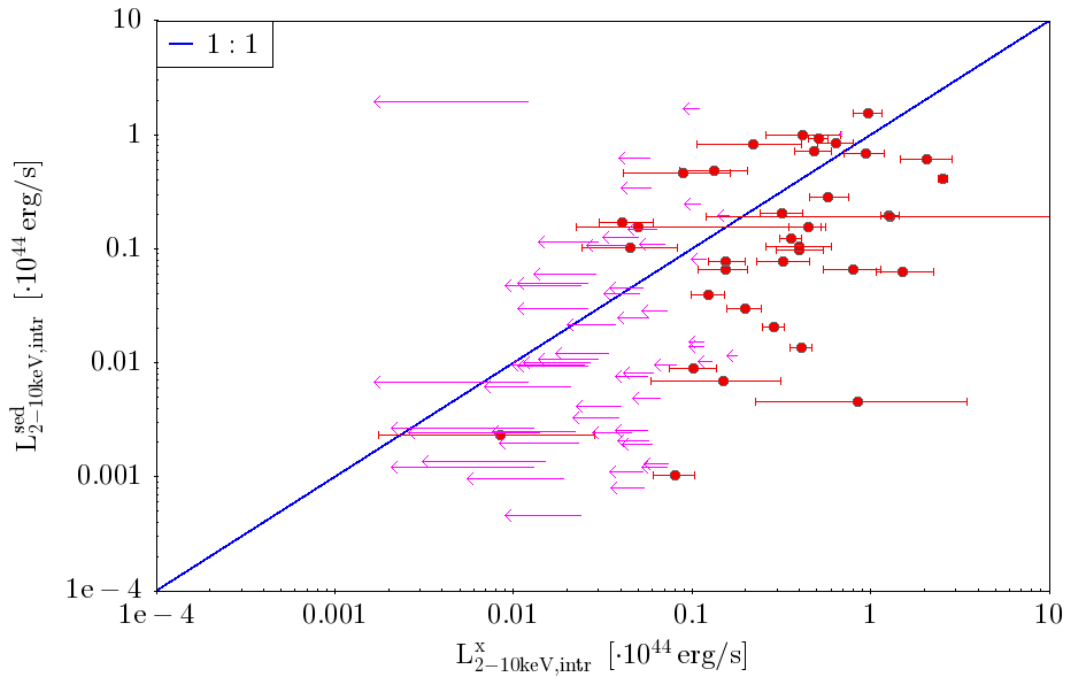
Figure 4.11: Comparison of the rest-frame $2 - 10$ keV intrinsic luminosities between those obtained from the AGN $12\,\mu$m luminosity ($\mathrm{L}^{\mathrm{sed}}_{2-10\mathrm{keV}}$) and those from the X-ray spectral analysis ($\mathrm{L}^{\mathrm{x}}_{2-10\mathrm{keV}}$). The $\mathrm{L}^{\mathrm{x}}_{2-10\mathrm{keV}}$ upper limits are those of the X-ray undetected sources and were obtained from the count-rate upper limits with a power-law model with $\Gamma = 0.41$.

of photometric points in the optical/NIR regime and their smaller errors. To improve the FIR SED-fitting for these sources, we chose to lower the number of optical bands used in the SED-fitting, excluding 10 of the 21 filters at wavelength $\lambda < 2\,\mu$m.

The new results, labeled as "FIR enhanced", show a visible improvement in the FIR SED-fitting. In figure 4.12 we show, as example, the comparison between the "all filters" and "FIR enhanced" SED-fitting results for source 9100023.
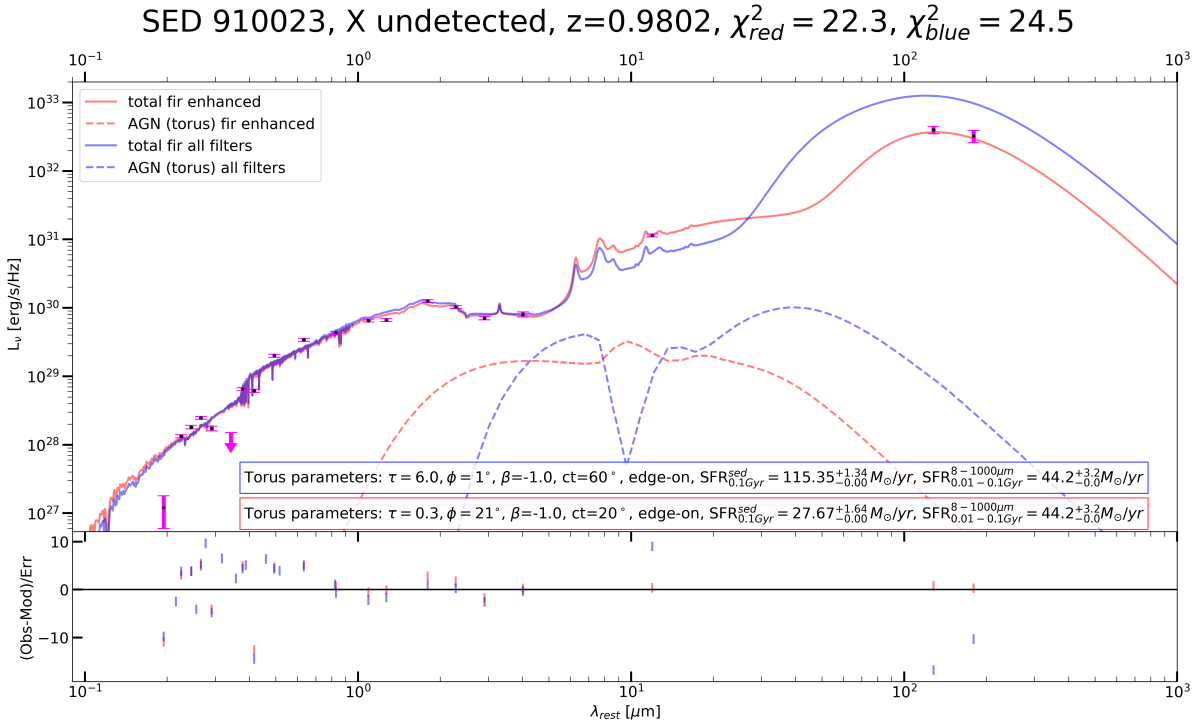

Figure 4.12: Comparison of SED fitting for source 9100023 between that performed using all the available filters (blue) and that performed excluding 10 (out of 21) filters at $\lambda < 2\,\mu$m to improve the fitting of FIR bands (red). The dashed lines are the respective AGN contributions to the total SED. The reported χ^2_{blue} is the best-fit χ^2 obtained with the model without AGN divided for the number of photometric points; the χ^2_{red} is the best-fit χ^2 obtained with the model with AGN divided for the number of photometric points minus one to take into account the additional component (see section 4.4).

4.4 AGN significance

The SED-fitting procedure allowed us to separate the contribution of the AGN from that of the galaxy, in particular from the SF contribution. However, this process is subject to a certain intrinsic degeneracy: an over-estimation of the AGN fraction will result in

an under-estimation of the IR emission from the galaxy and thus of the SFR and vice versa.

To assess the reliability of the AGN luminosity derived parameter (i.e. bolometric luminosity, AGN fraction, $2 - 10$ keV luminosity), we estimated the AGN significance using an F-test between the best-fit χ^2 with and without AGN component.

To do this, we carried out a second run of *sed3fit*, using the same optical and IR models, without any torus model. We compared the $\chi^2_{\text{NO-AGN}}$ obtained with the χ^2_{AGN} obtained using the torus models. The F-value was computed as

$$F_{\text{test}} = \frac{\chi^2_{\text{NO-AGN}} - \chi^2_{\text{AGN}}}{\bar{\chi}^2_{\text{AGN}}} \tag{4.11}$$

where $\bar{\chi}^2 = \chi^2/dof$ and dof is the number of degrees of freedom. As dof we considered the number of photometric points, in case of the model without AGN, and the number of photometric points minus one, to take into account the additional parameter (the torus), for the model with AGN. We are aware that the $\bar{\chi}^2$ we used is not a truly reduced χ^2, as in the dof we should consider all the free parameters of the model. However, as in Delvecchio et al. 2014, for the goals of our work (to find the AGN significance) we consider this "approximation" acceptable. We obtained seventy-four sources (79%) with an AGN significance $\geq 1\,\sigma$, forty-eight sources (51%) with $\geq 2\,\sigma$, thirty-three (35%) with $\geq 3\,\sigma$ and twenty-four (26%) with $\geq 4\,\sigma$. Considering only the best value of the chi squared, thirteen sources (14%) are better fitted with a model without AGN component; seven of them are sources for which we have only upper limits on their AGN IR luminosity, due to the low contribution of the AGN to the total SED.

The fact that nearly half of the sample has an AGN significance $< 2\,\sigma$ can be attributed both to an observational limit (i.e. few mid-IR data points) and to intrinsic low torus luminosities, with the torus emission which are completely diluted in the host-galaxy emission. In this regard, all the fourteen sources better fitted without the AGN component are not detected in the X-ray. Moreover, all the objects with AGN significance $\leq 1\,\sigma$ are not X-ray detected, except for three sources. Two of these, however, have luminosity in the lower end of our distribution ($L_{2-10\text{keV,intr}} < 10^{43}$ erg/s). The third source with $L_{2-10\text{keV,intr}} > 10^{43}$ erg/s and AGN significance $\leq 1\,\sigma$ has no far-IR detection, hence, we attribute the low AGN significance to the lack of FIR photometric points.

We studied the distributions of the [NeV] luminosities for the sources with AGN significance $< 2\,\sigma$ and those with AGN significance $\geq 2\,\sigma$. We found a segregation of the sources with low AGN significance at low [NeV] luminosities. In fact, while 44% of the sources with $\geq 2\,\sigma$ has $L_{[\text{NeV}]} < 10^{41}$ erg/s, this percentage goes up to 85% for the sources with AGN significance $< 2\,\sigma$. This segregation is in support of the fact that low AGN luminosities (the [NeV] emission is a proxy of the nuclear intrinsic emission) give trouble in separating the AGN component from the galaxy emission.

As our sample was selected on the basis of AGN spectral features (narrow [Ne V] emission lines), the fact that some sources are better fitted without the AGN component is a clear evidence that obscured AGN have to be studied via a multi-wavelength approach.

4.5 Comparison with results from only "type 2" torus model

As shown in section 4.3.2, nearly half of our sample has *face-on* torii as best-fit models. This may seem in contradiction with the fact that our sample is composed only of "type 2" AGN, selected on the basis of optical spectra.

As previously reported, the PDFs of the Φ (the angles between the line of sight and the torus equatorial plane) indicate that this is not a well-constrained parameter and many *face-on* sources have Φ compatible with values of *edge-on* AGN. As explained in section 4.3, the large uncertainties in the angle of sight are due to the fact that the torus parameters suffer from degeneracies, that are not possible to overcome with our photometric data. However, these degeneracies typically do not have a huge impact on the best-fit AGN luminosities (e.g. Pozzi et al. 2012) and we relied on these to draw conclusion on the AGN properties.

Nevertheless, we performed a SED-fitting run using only *edge-on* models, to which we will refer as "type 2 only", to check whether these new results would differ significantly from those obtained with the previous torus models ("type 1 & 2").

"Type 2" models

For the new SED-fitting run, we used the same torus parameters of the "type 1 & 2" run, with the only difference in the allowed values of Φ. In fact, we choose only values compatible with a *edge-on* model. The possible values of Φ are $1, 11, 21, 31, 41, 51, 61, 71$, but among these, only those with $\Phi < 90° − ct$.

"Type 2" results

Except for few sources, as we can see from figures 4.13, we do not find any particular improvement or worsening in the χ^2 of our sources between the two models. The few sources with significant differences show a worsening of the χ^2 with respect to the "type 1 & 2" model. These are sources for which the imposing of *edge-on* models has meant that the code had more difficulties in identifying the AGN emission and, probably, a part of it has been wrongly attributed to the SF component, as we can see from the higher number of upper limits on the AGN IR luminosity (fig 4.16).
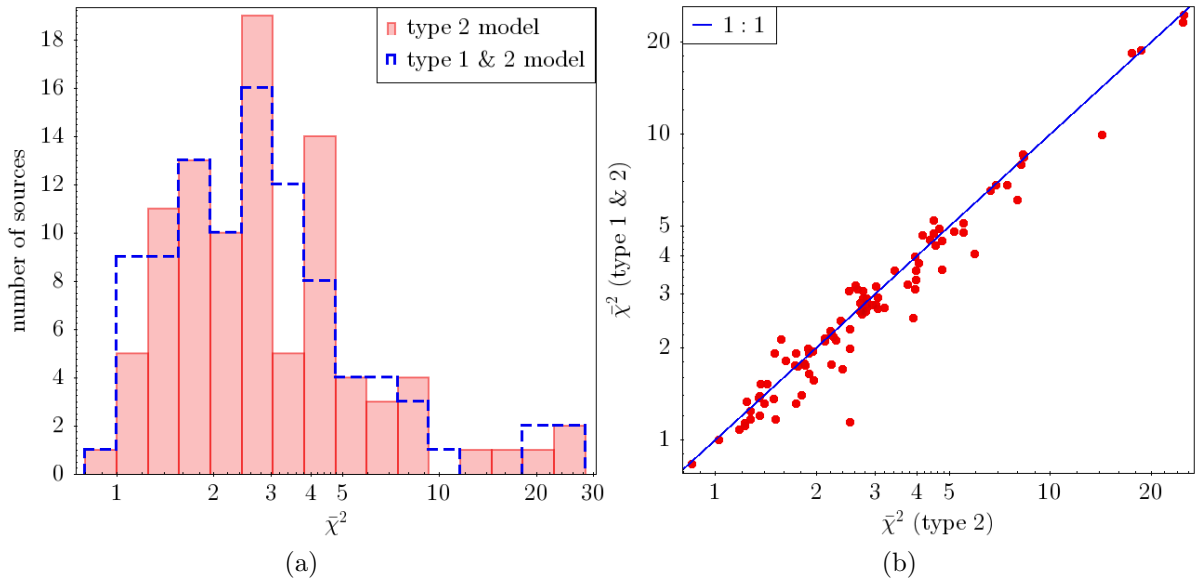
Figure 4.13: Comparisons of the best-fit reduced χ^2 between those obtained imposing *edge-on* models ("type 2" model) and those with both *face-on* and *edge-on* models ("type 1 &2"). We do not note significant difference between the χ^2 from the two models, with the exception of three sources.

Torus parameters

The best-fit parameters that show the largest differences between the two runs of SED-fitting are Φ and $\tau_{\mathrm{eq}}(9.7)$, as we can see from figure 4.14. Obviously, there are no sources with high values of Φ and the number of sources seen at $\Phi = 20°$ are more than tripled. Importantly, we note that there are ≈ 15 sources less with $\tau_{\mathrm{eq}}(9.7) = 0.5$ and ≈ 15 sources more with $\tau_{\mathrm{eq}}(9.7) = 0.1$, the minimum value possible in our models. This indicates that several of the sources that were seen *face-on*, are now found as *edge-on* but with lower values of optical depths.
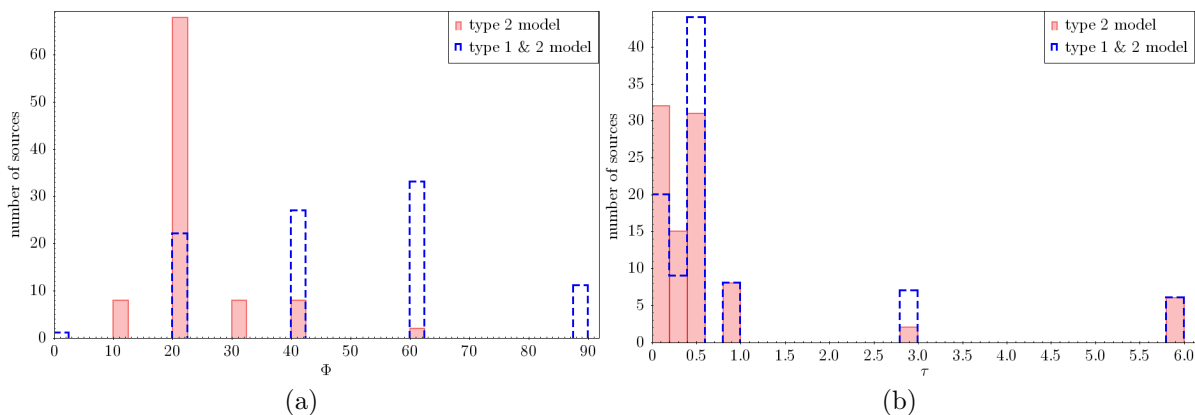

Figure 4.14: Comparison of the distribution of two torus parameters between the best-fit values obtained with ("type 2") and without ("type 1 & 2") imposing a *edge-on* angle of sight. (a) Φ: angle between the line of sight and the equatorial plane; (b) τ: torus equatorial optical depth at $9.7\,\mu$m. Several sources that were fitted with a *face-on* model need lower values of optical depths to be fitted as *edge-on*.

Star formation rates

The mean SFR obtained from the $8 - 1000\,\mu$m is $\mathrm{SFR}^{8-1000\mu\mathrm{m}} = (\,33.2 \pm 3.0\,)\,\mathrm{M}_\odot/\mathrm{yr}$. The mean SFR is within the $1\,\sigma$ error of the mean SFR obtained using "type 1 & 2" models. As we can see from figures 4.15, there is no evidence for significant differences between the SFR obtained adopting the two models.

AGN IR luminosities

Using the "type 2" models, twenty sources have only an upper limit on their AGN IR luminosity, in contrast with the eight obtained using "type 1 & 2" models. Moreover, if we add to these sources those with their $1\,\sigma$ lower end compatible with zero, we have thirty-one sources with an upper limit on their AGN $8 - 1000\,\mu$m luminosity. From
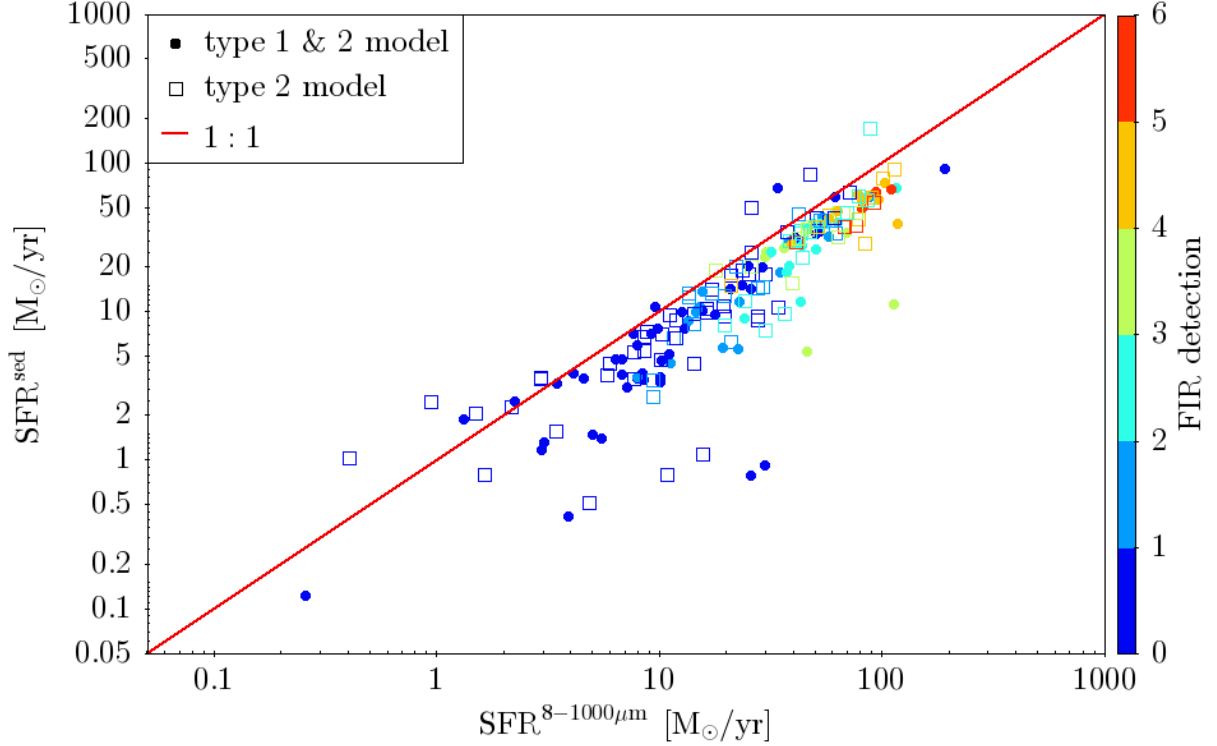
Figure 4.15: Comparison between the SFR obtained from optical-NIR bands with those from FIR, obtained imposing only *edge-on* models ("type 2" model in the legend) or allowing both *edge-on* and *face-on* ("type 1 & 2" model). SFR^{sed} are derived through the modeling of the stellar emission in the UV-to-NIR; $SFR^{8-1000\mu m}$ from the IR emission integrated in the rest-frame wavelength range $8 - 1000\,\mu m$ assuming the Kennicutt (1998b) SFR calibration converted to a Chabrier (2003) IMF. The color code indicates the number of photometric points available for each source in the FIR band. The red line is a 1:1 line. We note that there is no significant difference between the SFR obtained using the two models (i.e. "type 2" and "type 1 & 2" models).

figure 4.16 we see that a significant fraction of the sources with lower values for the AGN IR luminosity become sources with only an AGN luminosity upper limit when we impose *edge-on* only models.

Without considering the lower limits, the two models yield compatible luminosities (fig 4.17). The mean ratio between "type 2" model luminosities and those from "type 1 & 2" models is 1.01, with a standard deviation of 0.02.
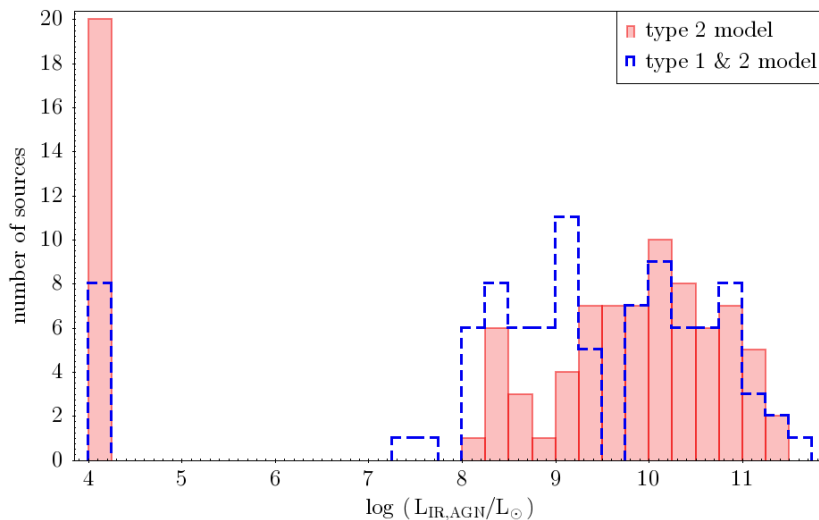

Figure 4.16: Distribution of the best-fit AGN $8 - 1000\,\mu$m luminosities obtained using only *edge-on* models (red histogram) and with both *edge-on* and *face-on* torus models. We see that the sources with lower AGN luminosities become sources with only an AGN luminosity upper limit ($\log L_{\text{IR,AGN}} = 4$ is the luminosity lower limit of our code) when we impose *edge-on* models.

Bolometric luminosities

As for the AGN IR luminosities, imposing only *edge-on* models increases the number of sources with an upper limit on the AGN bolometric luminosity. Without considering these sources, the mean of the bolometric luminosity is $L_{\text{bol}}^{\text{sed}} = (7.0 \pm 1.0) \cdot 10^{44}$ erg/s, totally compatible with the mean obtained using "model 1 & 2" $L_{\text{bol}}^{\text{sed}} = (6.5 \pm 1.2) \cdot 10^{44}$ erg/s. As we can see from figure 4.18, there are no significant differences in the AGN bolometric luminosities obtained using the two type of models.

"Type 2" conclusion

We investigated whether the imposing on *edge-on* torus would provide significantly different results with respect to models with both *edge-on* and *face-on* torus.
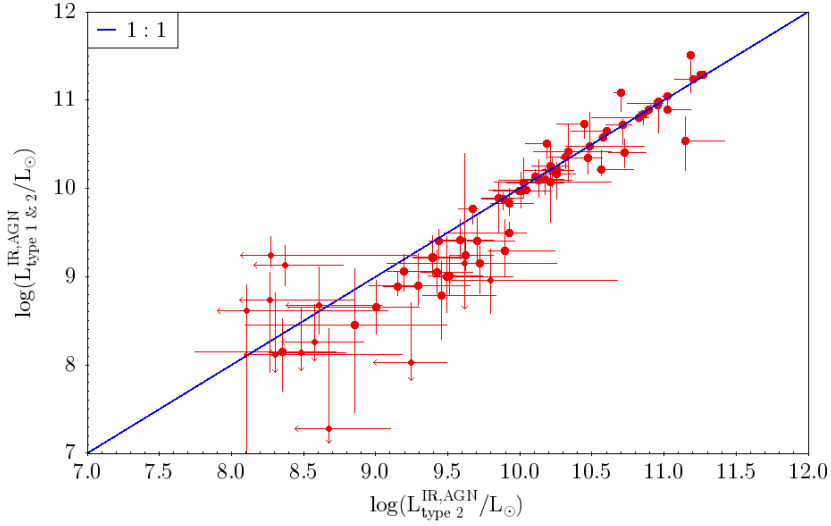
Figure 4.17: Comparison between the AGN $8 - 1000\,\mu$m luminosities obtained imposing only *edge-on* models and those using both *edge-on* and *face-on* torus models. Despite the differences in the models, the AGN IR luminosities are very similar.
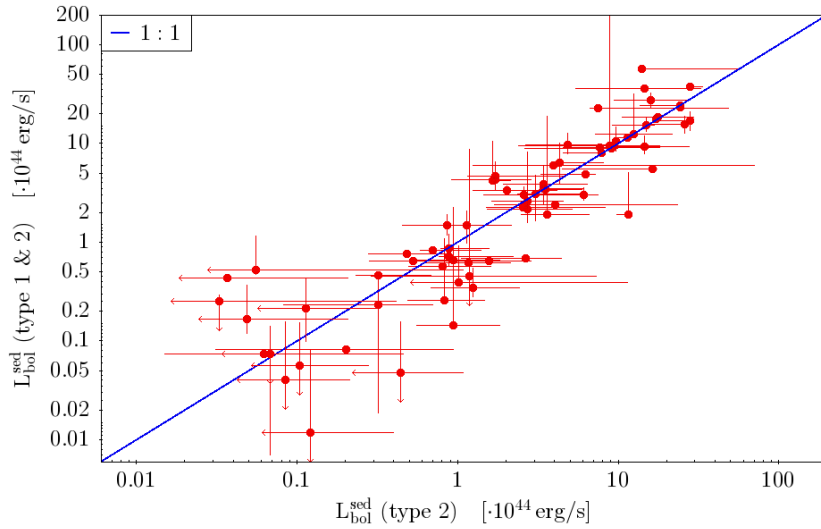

Figure 4.18: Comparison between the AGN bolometric luminosities obtained imposing only *edge-on* models and those using both *edge-on* and *face-on* torus models. Despite the differences in the models, the AGN bolometric luminosities are totally compatible.

About the torus parameters, the most significant differences are in the angle of sight and equatorial optical depth of the torus. However, we knew a priori that there are degeneracies between the torus parameters and that these cannot be used to derive firm conclusions on the AGN properties. We rely, instead, on the AGN luminosity and the derived properties.

According to the comparison of the best-fit χ^2, we do not find significant improvement or worsening of the fit between the two models, nor we note any differences in the SFR. The main differences in the AGN luminosities is the increase in the number of sources that are best-fitted with a negligible AGN contribution. Except for those, the AGN bolometric luminosities and the AGN IR luminosities have compatible values between the two models.

In conclusion, the lower number of sources with AGN luminosity upper limits and the fact that, except for those, the two models provided compatible results justified the choice of using both *face-on* and *edge-on* models for the SED-fittings.

4.6 Summary of the results

In the AGN-galaxy co-evolution scenario, a galaxy merger triggers most of the growth of both the stellar mass and the SMBH that lies in the galaxy core. The matter infalling into the SMBH activates the AGN and, because of the large amount of dust and gas, the AGN appears as an obscured source. Thus, this first phase of the AGN cycle is marked by obscured AGN activity and by high SF of the host-galaxy.

To characterize both the AGN and the host-galaxy properties, we performed a SED-fitting analysis of a sample of 94 [Ne V] selected type 2 AGN. We used optical-to-FIR data from the COSMOS2015 catalog, that ensures us up to 33 photometric points. The *sed3fit* SED-fitting code allows us to separate the AGN emission, in particular the mid-IR emission of the obscuring torus, from the stellar and SF-heated dust emission.

We used the mid-IR AGN emission to study AGN properties and make comparison with the results from the X-ray spectral analysis. The code provided us with the AGN IR $(8 - 1000 \, \mu\mathrm{m})$ luminosity, that was used to obtain the AGN IR fraction, defined as $f^{\mathrm{AGN}} = \mathrm{L}_{\mathrm{IR}}^{\mathrm{AGN}}/\mathrm{L}_{\mathrm{IR}}^{\mathrm{tot}}$. We obtained a mean AGN fraction of $f_{8-1000\mu\mathrm{m}}^{AGN} = 0.08 \pm 0.01$. For eight sources, the best-fit AGN contributions to the SED is low and we can only place upper limits to the AGN IR luminosity and AGN fraction. The SED-fitting analysis allowed us to obtain an estimate of the bolometric power. This is particularly important for the X-ray undetected sources, for which it was not possible to compute the intrinsic $2 - 10$ keV luminosity. The mean bolometric luminosity is $\mathrm{L}_{\mathrm{bol}}^{\mathrm{sed}} = (6.5 \pm 1.2) \cdot 10^{44}$ erg/s. We compared these luminosities with those obtained from the rest-frame $2-10$ keV intrinsic luminosity, for the sources with X-ray detection, using the Lusso et al. (2012) bolometric correction. Finally, using the Gandhi et al. (2009) relation, we computed the rest-frame $2 - 10$ keV luminosity from the AGN $12 \, \mu\mathrm{m}$ luminosity, obtaining a mean

$L_{2-10keV}^{sed} = (1.9 \pm 0.4) \cdot 10^{43}$ erg/s. We compared these values with those obtained from the X-ray spectral analysis. On average, the two luminosities are in agreement. The fact that we confirmed the existence of two correlations (bolometric luminosities from the IR emission and from X-ray spectral analysis, and $2 - 10$ keV luminosities from the $12\,\mu m$ and from the X-ray) is important, as these correlations can be used to estimate the AGN power when X-ray data are not available or are too shallow.

Finally, we re-fitted the SED using models without the AGN component with the aim of testing the AGN significance via an F-test. Half of our sample has an AGN significance ≥ 2 and a third has ≥ 3. Thirteen sources are better fitted using models without an AGN component. As our sample was composed of AGN, these thirteen sources are an indication of the importance of a multi-wavelength approach to type 2 AGN study and investigation. We explained the fact that we obtained AGN level of significance < 2 for half of our sample as caused by the poor coverage of the mid-IR wavelength, the lack of photometric FIR data along with a lower power of these AGN, that make it harder to separate the AGN and the SF emissions.

We also used the optical-to-FIR data to obtain the stellar mass and the SFR of the galaxies. The mean stellar mass of our sample is $M_* = (7.8 \pm 0.5) \cdot 10^{10}\,M_\odot$. We obtained two different estimates of the SFR, via the UV-optical-NIR emission, using the Bruzual (2007) library, and from the galaxy $8-1000\,\mu m$ luminosity, using the Kennicutt (1998b) relation. The mean $SFR^{8-1000\mu m} = (37.1 \pm 3.6)\,M_\odot/yr$ is, on average, 1.5 times the SFR estimate from UV-optical-NIR emission. We compared the SFR with those expected from the SFR-M_* correlation (Schreiber et al. 2015). The $SFR^{8-1000\mu m}$ are closer to the "main sequence" with respect to the SFR obtained from the UV-optical-NIR emission, which tend to underestimate the SFR. We ascribe this difference to the fact that the optical-NIR band of the SED could suffer from a not-well-modeled dust extinction or to a contribution of old populations to the FIR SED. If we limit our sample only to sources with at least two far-IR detections, all sources are within $1\,\sigma$ from the "main sequence", except one that has a higher SFR. This indicates that our sample does not differ significantly from "normal" galaxies and that the AGN has had a low impact on the host-galaxy SF. Finally, we used the galaxy emission to confirm the goodness of our fits via the IR8 relation (Elbaz et al. 2011): the majority of our sources lies within $1\,\sigma$ of the IR8 relation and the most distant sources are those with few FIR detections. We interpreted this as an indication of the importance of FIR photometric data in constraining properly the SED.

Chapter 5

Conclusions and future perspectives

In my thesis work I presented the results of the X-ray spectral analysis and of the optical-to-FIR SED-fitting performed on a sample of 94 [NeV]-selected type 2 AGN in the COSMOS field at $z \sim 1$.

The importance of studying type 2 AGN is twofold: on the one hand, in the BH-galaxy co-evolution scenario, the first phase of growth is likely associated to obscured AGN activity; on the other hand, type 2 AGN should be the main contributors to the X-ray background at energies above 30 keV. For what concerns the first issue, the presence of scaling relations between SMBH and galaxy properties called for their simultaneous growth. This growth, likely triggered by a wet galaxy merger, is characterized by an intense star formation, due to the disruption of the ISM equilibrium, and by an obscured AGN activity as a large quantity of gas is funneled into the central SMBH. The study of both the galaxy and AGN properties can help in shedding light into this first phase of co-evolution and into the feedback processes that will eventually stop both growths. Regarding the XRB, at energies above 30 keV only a fraction of it has been resolved into individual sources, and XRB synthesis models predict that between 10% and 40% of the missing XRB is produced by Compton Thick (CT) AGN (i.e. obscured AGN with $N_H > 10^{24}$ cm^{-2}); the density of such objects with luminosity in the $10^{43} - 10^{44}$ erg/s range should peak at $z \sim 1$ (Gilli 2013).

The use of the [NeV] selection method allows to properly select objects that should be the very responsible of the missing XRB flux at energy E> 30 keV. The high energy photons (> 97 eV) required to ionized Neon atoms from NeIV to NeV ensures that [NeV] emission cannot be produced by processes linked to star formation and that a harder energy source is involved (i.e. the AGN). Therefore, being its origin linked to the AGN nuclear emission that illuminates the NLR, the [NeV] flux correlates with the AGN intrinsic power. The X/[NeV] ratio can then be used to study the obscuration of the AGN, as the observed X-ray flux is linked to the nuclear emission but also affected by obscuration (Gilli et al. 2010).

The sample under investigation in my thesis project was defined by Mignoli et al.

([2013](#)) and is composed of 94 AGN in the COSMOS field, selected on the basis of the detection of the high-ionization [NeV]3426Å line and including the objects with only narrow lines in their optical spectra. Due to the fact that the data for the selection came from VIMOS observations within the zCOSMOS-Bright survey (Lilly et al. [2007](#)), a selection based on [NeV] lines limited this analysis to AGN in the $0.65 < z < 1.20$ redshift range. Moreover, the fact that all the spectral data came from a single instrument, assures a uniform quality of the spectra for the whole sample.

My work is divided into two parts: the X-ray spectral analysis of the sample, to characterize the AGN properties such as obscuration and X-ray intrinsic luminosity (i.e. the derived luminosity once the effects of the obscuration are taken into account), and the SED-fitting, using optical-to-FIR data, to derive both AGN (torus) and host-galaxies properties.

X-ray analysis

I performed X-ray spectral analysis of the sample with the aim of studying, in particular, the column density distribution and the fraction of heavily obscured sources. The same sample was already studied by Vignali et al. ([2014](#)) using the X-ray data from the C-COSMOS survey; I used of the new COSMOS Legacy data (Civano et al. [2016](#), Marchesi et al. [2016](#)) that provided an improvement both in terms of exposure time and areal coverage. The use of new data increased the number of X-ray detections from 23 to 36 and provided a more uniform coverage of the whole COSMOS field. I divided our sources into two sub-samples, on the basis of the number of net (background-subtracted) counts, with a threshold of 90 counts. I used the Gaussian statistics for the source of the high-count sample (their mean net-count is 285 ± 96) and the Cash statistics for the low-count sample (which has a mean net-count number of 40 ± 5).

Although several sources were in the low-statistics regime (having few counts), the extremely low background achieved using the Chandra X-ray Observatory provided me with a good SNR and the possibility to perform the spectral fitting even for sources with ≈ 10 net-counts. To work with low-statistic sources, I chose for all the 36 sources with X-ray detection a simple spectral model: a power law with fixed photon index $\Gamma = 1.8$ and an absorption component to model the source obscuration, which resulted well suited to fit the source spectra. The mean N_H of the high-count sample is $\approx 7.5 \cdot 10^{22}$ cm^{-2}, while for the low-count sample I obtained $\approx 32.2 \cdot 10^{22}$ cm^{-2}. On the basis of their obscuration and following Gilli et al. ([2010](#)), I classified nine sources as highly obscured ($N_H > 10^{23}$ cm^{-2}) and two as CT objects.

Once the column density was derived, I was able to compute the intrinsic X-ray luminosity of our sources, obtaining a mean value of $L_{intr,\text{2-10 keV}} \approx 5 \cdot 10^{43}$ erg/s. This value is in the luminosity range predicted by XRB synthesis models for the majority of the XRB missing sources at $z \approx 1$ (which is $10^{43} < L < 10^{44}$ erg/s). Using the rest-frame $2 - 10$ keV luminosity, I computed the X/[NeV] ratio and used it to obtain a

further estimate of the source absorption. Since I obtained obscuration values compatible with those from the spectral analysis, I confirmed the reliability of the X/[NeV] ratio as obscuration tracer, as previously done by Gilli et al. (2010).

Using a KS test I tested and confirmed that the 58 sources without X-ray detection are not detected because of their lower flux and not because they fall in regions observed with lower sensitivity than the X-ray detected sources. I computed their upper limits of the rest-frame $2-10$ keV flux and used these values to obtain the X/[NeV] upper limits. The X/[NeV] ratio provided me with estimates on the source absorption: two thirds of the X-ray undetected sources are compatible with $N_H > 10^{23}$ cm^{-2}, and at least two objects are CT.

The better quality of the new data allowed me to obtain the spectral properties of eight sources previously undetected in Vignali et al. (2014) and to improve the values of the 28 already detected. For these sources our results are in good agreement with those of Vignali et al. (2014) within errors. Considering the whole [NeV] sample, I found that at least 50% of the sample is composed of sources with high absorption ($N_H > 10^{23}$ cm^{-2}), and at least 4% of the sources are CT AGN. Vignali et al. (2014), which used the previous C-COSMOS data, computed the X/[NeV] ratio in a similar way and obtained a CT fraction of $\approx 13 \pm 5\%$. It is important to note that the CT fraction estimates are lower limits, as they were obtained considering CT only the sources with X/[NeV]≤ 15. As reported in Gilli et al. (2010), while a X/[NeV]≤ 15 assures the CT nature of a source, CT objects can also be found in the $15 <$ X/[NeV] < 100 range, thus potentially increasing the true fraction of heavily obscured AGN in the current sample.

SED analysis

The use of a SED-fitting algorithm allowed me to separated the galaxy and the AGN emission. I used optical-to-FIR data from the COSMOS2015 catalog (Laigle et al. 2016), that ensures up to 33 photometric points. The SED-fitting code *sed3fit* (Berta et al. 2013 and da Cunha et al. 2008) makes use of three spectra libraries (i.e. of the optical stellar emission, of the galaxy dust IR emission and of the AGN emission) and is based upon the energy equilibrium between the radiation absorbed in the optical band and re-emitted in the IR wavelengths by the dust. The SED-fitting results suffer from a double degeneracy: one is related to the SF and the AGN contribution to the IR emission, the other intrinsic to the plethora of AGN torus models. The first is also linked to the number of mid-IR and far-IR detections; in particular, I found that with less than two far-IR photometric points it is difficult to place good constraints to the SF contribution. In this regard, it is worth mentioning that this difficulty in properly constraining the SF component makes it harder to establish the relative AGN/SF contribution in the mid-IR, where the AGN component can be incorrectly associated to the SF. The sub-optimal coverage of the mid-IR wavelengths surely played a role in this contest. As for the degeneracy within the torus parameters, I found that if we derive the AGN properties from the AGN best-fit

117

model, this degeneracy does not affect significantly our results, as previously reported by Pozzi et al. (2012). In fact, the probability distribution functions show that usually the AGN bolometric luminosity is well determined, even when the torus parameters are not so well constrained. Moreover, changing the torus models does not provide significantly different best-fit luminosities.

I found a mean AGN IR fraction of $f^{AGN}_{8-1000\mu m} = 0.08 \pm 0.01$, indicating that the sample is composed of "normal" (i.e. not extremely bright) AGN within star-forming galaxies, as the FIR band is dominated by the SF, and the AGN contributes to only a fraction of this luminosity. The SED-fitting analysis allowed me to obtain an estimate of the bolometric power, particularly important for the X-ray undetected sources, for which it was not possible to compute the intrinsic 2 - 10 keV luminosity and then convert it into a bolometric luminosity. The mean bolometric luminosity of the sample is $L^{sed}_{bol} = (6.5 \pm 1.2) \cdot 10^{44}$ erg/s. For the sources with X-ray detection, I found a correlation, within a factor ~ 2.8, between the bolometric luminosities from the SED-fitting and those computed from the intrinsic $2 - 10$ keV luminosities using the Lusso et al. (2012) bolometric correction. The relative good agreement between the results derived from the SED-fitting and from the X-ray confirms the validity of the SED-fitting procedure and the strength of the values we obtained.

As the torus absorbs the AGN emission, mostly in the optical wavelengths, it re-emits in the mid-IR bands. Thus the mid-IR AGN flux can be considered a proxy of the AGN intrinsic power. This allowed me to obtain an estimate of the AGN intrinsic $2 - 10$ keV luminosity, computed from the $12\,\mu m$ luminosity (derived from the SED-fitting) using the Gandhi et al. (2009) relation. The use of this luminosity is twofold: on the one hand, for the X-ray detected sources, I compared them with those obtained from the X-ray spectral analysis, finding a good correlation (their mean ratio is 1.0 ± 0.2) between them, especially for the source with at least two FIR datapoints; on the other hand, they allowed me to obtain the AGN intrinsic power even for sources without X-ray detection. Overall, I may reaffirm the importance of the two correlations ($L^{sed}_{bol} - L^x_{bol}$ and $L_{12\mu m} - L_{2-10keV,intr}$) to study the AGN properties of sources for which X-ray data are too shallow or not available. This type of multi-wavelength approach, which exploits the synergy between X-ray and IR data to place strictly constrain on obscured AGN properties, could be extended in the near future to the whole sky. The *Wide-field Infrared Survey Explorer* (WISE) has provided a four IR bands ($3.4, 4.6, 12$ and $22\,\mu m$) all-sky coverage, and, in the coming years, the *eROSITA* satellite will produce an all-sky coverage in the X-ray band up to 10 keV. Obviously, to put good constraints on the mid-IR AGN emission we have to first distinguish it from the SF component, therefore observations in the optical and far-IR wavelengths will be also needed. For example, the optical data could be provided by the *Sloan Digital Sky Survey* (SDSS), although, strictly speaking, it is not an all-sky survey. However, the selection and the study of obscured AGN will greatly benefit from the combination of these mid-IR and X-ray capabilities.

The distribution of the AGN IR luminosity, along with a visual inspection of the SED,

indicates that for a fraction of the sample the AGN component may be not significant. Comparing the χ^2 obtained using models with and without the torus emission allowed me to estimate the AGN significance. I found that half of our sample has an AGN significance $\geq 2\,\sigma$ and a third has $\geq 3\,\sigma$. I explain the low significance of the AGN component for half of our sample as probably caused by the fact that the code seems to assign the AGN emission to the SF component in case of few mid-and-far-IR datapoints and low AGN power. Furthermore, I found that the majority of the sources with low significance for the AGN ($< 2\,\sigma$) has low X-ray and [NeV] luminosities (i.e. low AGN intrinsic luminosities), thus indicating that the low significance should be due to the AGN component being possibly diluted in the galaxy stronger emission.

The SED-fitting also allowed me to characterize the host galaxy, in particular via the stellar masses and the SFR. I found that the sample is composed of galaxies with $6{\cdot}10^9 < M < 3{\cdot}10^{11}\,\mathrm{M_\odot}$, in agreement with the average galaxy masses at $z \sim 1$, which are $10 < \log(M/\mathrm{M_\odot}) < 12$ (e.g. van der Wel et al. 2006). Once the SED-fitting separates the AGN from the galaxy emission, I was able to obtain the SFR from the optical emission. I further investigated the SFR using the Kennicutt (1998a) relation, based on the fact that the dust absorbs the UV radiation of the SF and re-emits it in the far-IR band. This allowed me to estimate the SFR from the $8 - 1000\,\mu\mathrm{m}$ luminosity. I found a mean SFR of $\mathrm{SFR}^{8-1000\mu\mathrm{m}} = (\,37.1 \pm 3.6\,)\,\mathrm{M_\odot/yr}$. To check whether the galaxies of the sample would differ from "normal" galaxies, I used the SFR-M_* correlation (Schreiber et al. 2015). In fact, for "normal" galaxies the SFR correlates with the stellar mass and the galaxies compose the so called "main sequence" into the SFR-M_* diagram. Although with a certain dispersion, which can be understood if we consider the uncertainties in the whole process, I found a good agreement between the SFR and those expected from the SFR-M_* correlation. Moreover, if I consider only the sources with at least two far-IR photometric points (with one exception), all are within $1\,\sigma$ of the "main sequence". I conclude that our sample does not differ significantly from "normal" galaxies at $z \sim 1$ and that the AGN had a low impact on the host-galaxy SF. Moreover, this indicates also that the sample is not composed of starburst galaxies or, at least, of galaxies that are now in a strong starbust phase. In addition to the FIR luminosity, also the galaxy $8\,\mu\mathrm{m}$ emission is a proxy of the SFR, as it is mainly attributed to PAH molecules. Therefore, the ratio between the $8\,\mu\mathrm{m}$ and the $8 - 1000\,\mu\mathrm{m}$ luminosities, called IR8 (Elbaz et al. 2011), is approximately constant. I used this ratio to confirm the ability of the code to constrain the SF component. I found that the majority of our sources lies within $1\,\sigma$ of the IR8 relation and the most distant sources are those with few FIR detections. This supports the obtained SF values for the sources with at least two FIR detection and reaffirms the importance of FIR photometric data in constraining properly the SED.

Future perspectives

In my work I could only provide an indication of the AGN influence on the host galaxy via the comparison of the source SFR with the SFR-M_* "main sequence". Performing the same analysis as in this work on a sample of galaxies without evident AGN activity can provide interesting results. In fact, this would allow us to make a comparison of all the galaxies properties obtained in my work (e.g. stellar mass, gas content, relative fractions of different phases gas, star formation history), with the aim of looking for the influence of the AGN on the general properties of the host galaxy and, in particular, on the SF, as predicted by the AGN-galaxy co-evolution scenario. Moreover, given the size of the sample (94) analyzed in my work, it can be considered statistically relevant. Finally, the COSMOS field can be the right place to perform such an analysis, as it is wide enough to produce statistically significant results, but also with observations deep enough to detect faint objects and, equally importantly, it is covered at all the possible wavelengths, from the X-ray to radio bands, allowing the type of multi-wavelength approach we performed.

Another possible extension of the present work can be related to the evolution of the AGN properties as a function of the redshift. My work made use of the [NeV] line as selection method, which provided me with a well defined redshift range. The use of different lines allows to select different redshifts. As an example, AGN at $z < 0.8$ can be selected via the use of the [OIII]5007Å (Vignali et al. 2010), while a selection in the $1.5 < z < 3$ redshift range can be achieved via the use of C IV 1549Å line (Mignoli et al. 2019). Carrying out both X-ray analysis and optical-to-FIR SED-fitting on these samples can be used to investigate the redshift evolution of the AGN and host-properties. As both the AGN density and the SFR density should peak at $z \sim 1 - 2$, the so-called "cosmic noon", being able to obtain the evolution of several parameters for the AGN and the galaxy is not of secondary importance.

The BH-galaxy co-evolution scenario predicts that the SB activity and the AGN growth are triggered by a wet-merger; although I do not find on-going starburst activities, the study of the environment around the galaxies of the sample may provide insights into the mutual influence of the AGN activity and SF processes. Moreover, it can shed light whether past mergers started the AGN activity or if secular accretion (i.e. the cooling of gas external to the galaxies) responsible for its fueling (e.g. Kormendy et al. 2004, Schawinski et al. 2011).

Bibliography

ACIS Instrument Information (2010). The Chandra X-ray Center. URL: http://cxc.harvard.edu/cal/Acis/.

Alonso-Herrero, Almudena et al. (Aug. 2011). "Torus and Active Galactic Nucleus Properties of Nearby Seyfert Galaxies: Results from Fitting Infrared Spectral Energy Distributions and Spectroscopy". In: *ApJ* 736.2, 82, p. 82. arXiv: 1105.2368 [astro-ph.CO].

Antonucci, R. R. J. and J. S. Miller (Oct. 1985). "Spectropolarimetry and the nature of NGC 1068." In: *ApJ* 297, pp. 621–632.

Antonucci, Robert (Jan. 1993). "Unified models for active galactic nuclei and quasars." In: *ARA&A* 31, pp. 473–521.

Arnaud, K. A. (Jan. 1996). "XSPEC: The First Ten Years". In: *Astronomical Data Analysis Software and Systems V*. Ed. by George H. Jacoby and Jeannette Barnes. Vol. 101. Astronomical Society of the Pacific Conference Series, p. 17.

Barbosa, F. K. B. et al. (June 2009). "Gemini/GMOS IFU gas velocity 'tomography' of the narrow line region of nearby active galaxies". In: *MNRAS* 396.1, pp. 2–18.

Berta, S. et al. (Mar. 2013). "Panchromatic spectral energy distributions of Herschel sources". In: *A&A* 551, A100, A100. arXiv: 1301.4496 [astro-ph.CO].

Blandford, R. D. (Jan. 1990). "Physical processes in active galactic nuclei." In: ed. by R. D. Blandford et al., pp. 161–275.

Blandford, R. D. and M. J. Rees (Mar. 1978). "Extended and compact extragalactic radio sources: interpretation and theory." In: *Phys. Scr* 17, pp. 265–274.

Bruzual, G. (Dec. 2007). "Stellar Populations: High Spectral Resolution Libraries. Improved TP-AGB Treatment". In: *From Stars to Galaxies: Building the Pieces to Build Up the Universe*. Ed. by A. Vallenari et al. Vol. 374. Astronomical Society of the Pacific Conference Series, p. 303. arXiv: astro-ph/0702091 [astro-ph].

Capetti, A. et al. (Oct. 1996). "Radio Outflows and the Origin of the Narrow-Line Region in Seyfert Galaxies". In: *ApJ* 469, p. 554.

Cash, W. (Mar. 1979). "Parameter estimation in astronomy through application of the likelihood ratio." In: *ApJ* 228, pp. 939–947.

Chabrier, Gilles (July 2003). "Galactic Stellar and Substellar Initial Mass Function". In: *Publications of the Astronomical Society of the Pacific* 115.809, pp. 763–795. arXiv: astro-ph/0304382 [astro-ph].

Charlot, Stéphane and S. Michael Fall (Aug. 2000). "A Simple Model for the Absorption of Starlight by Dust in Galaxies". In: *ApJ* 539.2, pp. 718–731. arXiv: `astro-ph/0003128 [astro-ph]`.

Chartas, G. et al. (May 2016). "Gravitational lensing size scales for quasars". In: *Astronomische Nachrichten* 337.4-5, p. 356. arXiv: `1509.05375 [astro-ph.HE]`.

Civano, F. et al. (Mar. 2016). "The Chandra Cosmos Legacy Survey: Overview and Point Source Catalog". In: *ApJ* 819.1, 62, p. 62. arXiv: `1601.00941 [astro-ph.GA]`.

Collinson, James S. et al. (Feb. 2017). "Reaching the peak of the quasar spectral energy distribution - II. Exploring the accretion disc, dusty torus and host galaxy". In: *MNRAS* 465.1, pp. 358–382. arXiv: `1610.04221 [astro-ph.HE]`.

Combes, F. et al. (Mar. 2019). "ALMA observations of molecular tori around massive black holes". In: *Astronomy and Astrophysics* 623, A79, A79. arXiv: `1811.00984 [astro-ph.GA]`.

Crummy, J. et al. (Feb. 2006). "An explanation for the soft X-ray excess in active galactic nuclei". In: *MNRAS* 365.4, pp. 1067–1081. arXiv: `astro-ph/0511457 [astro-ph]`.

da Cunha, Elisabete, Stéphane Charlot, and David Elbaz (Aug. 2008). "A simple model to interpret the ultraviolet, optical and infrared emission from galaxies". In: *MNRAS* 388.4, pp. 1595–1617. arXiv: `0806.1020 [astro-ph]`.

De Marco, B. et al. (May 2013). "Discovery of a relation between black hole mass and soft X-ray time lags in active galactic nuclei". In: *MNRAS* 431.3, pp. 2441–2452. arXiv: `1201.0196 [astro-ph.HE]`.

Dekel, A. and J. Silk (Apr. 1986). "The Origin of Dwarf Galaxies, Cold Dark Matter, and Biased Galaxy Formation". In: *ApJ* 303, p. 39.

Delvecchio, I. et al. (Apr. 2014). "Tracing the cosmic growth of supermassive black holes to z 3 with Herschel". In: *MNRAS* 439.3, pp. 2736–2754. arXiv: `1401.4503 [astro-ph.GA]`.

Di Matteo, Tiziana, Volker Springel, and Lars Hernquist (Feb. 2005). "Energy input from quasars regulates the growth and activity of black holes and their host galaxies". In: *Nature* 433.7026, pp. 604–607. arXiv: `astro-ph/0502199 [astro-ph]`.

Done, C. et al. (Oct. 2007). "The Origin of the Soft Excess in AGN". In: *The Central Engine of Active Galactic Nuclei*. Ed. by L. C. Ho and J. -W. Wang. Vol. 373. Astronomical Society of the Pacific Conference Series, p. 121. arXiv: `astro-ph/0703449 [astro-ph]`.

Done, Chris (Aug. 2010). "Observational characteristics of accretion onto black holes". In: *arXiv e-prints*, arXiv:1008.2287, arXiv:1008.2287. arXiv: `1008.2287 [astro-ph.HE]`.

Efstathiou, A., J. H. Hough, and S. Young (Dec. 1995). "A model for the infrared continuum spectrum of NGC 1068". In: *MNRAS* 277.3, pp. 1134–1144.

Elbaz, D. et al. (Sept. 2011). "GOODS-Herschel: an infrared main sequence for star-forming galaxies". In: *A&A* 533, A119, A119. arXiv: `1105.2537 [astro-ph.CO]`.

Elitzur, Moshe (Aug. 2008). "The toroidal obscuration of active galactic nuclei". In: *New Astronomy Reviews* 52.6, pp. 274–288. arXiv: `0805.3699 [astro-ph]`.

Elvis, Martin et al. (Sept. 2009). "The Chandra COSMOS Survey. I. Overview and Point Source Catalog". In: *ApJS* 184.1, pp. 158–171. arXiv: 0903.2062 [astro-ph.CO].

Evans, I. N. et al. (Mar. 1991). "HST Imaging of the Inner 3 Arcseconds of NGC 1068 in the Light of [O iii] lambda 5007". In: *ApJ* 369, p. L27.

Fanaroff, B. L. and J. M. Riley (May 1974). "The morphology of extragalactic radio sources of high and low luminosity". In: *MNRAS* 167, 31P–36P.

Feltre, A. et al. (Oct. 2012). "Smooth and clumpy dust distributions in AGN: a direct comparison of two commonly explored infrared emission models". In: *MNRAS* 426.1, pp. 120–127. arXiv: 1207.2668 [astro-ph.CO].

Ferrarese, Laura and David Merritt (Aug. 2000). "A Fundamental Relation between Supermassive Black Holes and Their Host Galaxies". In: *ApJ* 539.1, pp. L9–L12. arXiv: astro-ph/0006053 [astro-ph].

Feruglio, C. et al. (July 2010). "Quasar feedback revealed by giant molecular outflows". In: *A&A* 518, L155, p. L155. arXiv: 1006.1655 [astro-ph.CO].

Fiore, F. et al. (May 2017). "AGN wind scaling relations and the co-evolution of black holes and galaxies". In: *A&A* 601, A143, A143. arXiv: 1702.04507 [astro-ph.GA].

Fritz, J., A. Franceschini, and E. Hatziminaoglou (Mar. 2006). "Revisiting the infrared spectra of active galactic nuclei with a new torus emission model". In: *MNRAS* 366.3, pp. 767–786. arXiv: astro-ph/0511428 [astro-ph].

Fruscione, Antonella et al. (June 2006). "CIAO: Chandra's data analysis system". In: *Proc. SPIE*. Vol. 6270. Society of Photo-Optical Instrumentation Engineers (SPIE) Conference Series, p. 62701V.

Gandhi, P. et al. (Aug. 2009). "Resolving the mid-infrared cores of local Seyferts". In: *A&A* 502, pp. 457–472. arXiv: 0902.2777.

Gebhardt, Karl et al. (Aug. 2000). "A Relationship between Nuclear Black Hole Mass and Galaxy Velocity Dispersion". In: *ApJ* 539.1, pp. L13–L16. arXiv: astro-ph/0006289 [astro-ph].

Genzel, Reinhard, Frank Eisenhauer, and Stefan Gillessen (Oct. 2010). "The Galactic Center massive black hole and nuclear star cluster". In: *Reviews of Modern Physics* 82.4, pp. 3121–3195. arXiv: 1006.0064 [astro-ph.GA].

Gierliński, Marek and Chris Done (Mar. 2004). "Is the soft excess in active galactic nuclei real?" In: *MNRAS* 349.1, pp. L7–L11. arXiv: astro-ph/0312271 [astro-ph].

Gilli, R. (Jan. 2013). "The cosmic X-ray background: abundance and evolution of hidden black holes." In: *Mem. Soc. Astron. Italiana* 84, p. 647. arXiv: 1304.3665 [astro-ph.CO].

Gilli, R., A. Comastri, and G. Hasinger (Feb. 2007). "The synthesis of the cosmic X-ray background in the Chandra and XMM-Newton era". In: *A&A* 463.1, pp. 79–96. arXiv: astro-ph/0610939 [astro-ph].

Gilli, R. et al. (Sept. 2010). "The X-ray to [Ne V]3426 flux ratio: discovering heavily obscured AGN in the distant Universe". In: *A&A* 519, A92, A92. arXiv: 1005.0373 [astro-ph.CO].

Harrison, F. A. et al. (Nov. 2016). "The NuSTAR Extragalactic Surveys: The Number Counts of Active Galactic Nuclei and the Resolved Fraction of the Cosmic X-Ray Background". In: *ApJ* 831.2, 185, p. 185. arXiv: 1511.04183 [astro-ph.HE].

Herrnstein, J. R. et al. (Aug. 2005). "The Geometry of and Mass Accretion Rate through the Maser Accretion Disk in NGC 4258". In: *ApJ* 629.2, pp. 719–738. arXiv: astro-ph/0504405 [astro-ph].

Hopkins, Philip F. et al. (Mar. 2006). "A Unified, Merger-driven Model of the Origin of Starbursts, Quasars, the Cosmic X-Ray Background, Supermassive Black Holes, and Galaxy Spheroids". In: *ApJS* 163.1, pp. 1–49. arXiv: astro-ph/0506398 [astro-ph].

Hopkins, Philip F. et al. (June 2007). "The Co-Formation of Spheroids and Quasars Traced in their Clustering". In: *ApJ* 662.1, pp. 110–130. arXiv: astro-ph/0611792 [astro-ph].

Ichimaru, S. (Jan. 1977). "Theory of Magnetic-Field Turbulence in Disk Plasmas and its Application to the Galaxy and Accretion Model of Compact X-Ray Binaries". In: *Plasma physics: Nonlinear Theory and Experiments*, p. 262.

Jaffe, W. et al. (May 2004). "The central dusty torus in the active nucleus of NGC 1068". In: *Nature* 429.6987, pp. 47–49.

Juneau, Stéphanie et al. (Aug. 2011). "A New Diagnostic of Active Galactic Nuclei: Revealing Highly Absorbed Systems at Redshift >0.3". In: *ApJ* 736.2, 104, p. 104. arXiv: 1105.3194 [astro-ph.CO].

Kaastra, J. S. et al. (Feb. 2000). "X-ray absorption lines in the Seyfert 1 galaxy NGC 5548 discovered with Chandra-LETGS". In: *A&A* 354, pp. L83–L86. arXiv: astro-ph/0002345 [astro-ph].

Kaspi, Shai et al. (Apr. 2000). "Reverberation Measurements for 17 Quasars and the Size-Mass-Luminosity Relations in Active Galactic Nuclei". In: *ApJ* 533.2, pp. 631–649. arXiv: astro-ph/9911476 [astro-ph].

Kaspi, Shai et al. (Aug. 2005). "The Relationship between Luminosity and Broad-Line Region Size in Active Galactic Nuclei". In: *ApJ* 629.1, pp. 61–71. arXiv: astro-ph/0504484 [astro-ph].

Kellermann, K. I. (Aug. 1989). "Book Review: Galactic and extragalactic radio astronomy. / Springer-Verlag, 1988". In: *The Observatory* 109.1091, p. 163.

Kennicutt Robert C., Jr. (Jan. 1998a). "Star Formation in Galaxies Along the Hubble Sequence". In: *ARA&A* 36, pp. 189–232. arXiv: astro-ph/9807187 [astro-ph].

— (Jan. 1998b). "Star Formation in Galaxies Along the Hubble Sequence". In: *ARA&A* 36, pp. 189–232. arXiv: astro-ph/9807187 [astro-ph].

Koekemoer, A. M. et al. (Sept. 2007). "The COSMOS Survey: Hubble Space Telescope Advanced Camera for Surveys Observations and Data Processing". In: *ApJS* 172.1, pp. 196–202. arXiv: astro-ph/0703095 [astro-ph].

Kormendy, John and Jr. Kennicutt Robert C. (Sept. 2004). "Secular Evolution and the Formation of Pseudobulges in Disk Galaxies". In: *ARA&A* 42.1, pp. 603–683. arXiv: astro-ph/0407343 [astro-ph].

Kormendy, John and Douglas Richstone (Jan. 1995). "Inward Bound—The Search For Supermassive Black Holes In Galactic Nuclei". In: *ARA&A* 33, p. 581.

Krolik, Julian H. and Mitchell C. Begelman (June 1988). "Molecular Tori in Seyfert Galaxies: Feeding the Monster and Hiding It". In: *ApJ* 329, p. 702.

Laigle, C. et al. (June 2016). "The COSMOS2015 Catalog: Exploring the 1 < z < 6 Universe with Half a Million Galaxies". In: *ApJS* 224.2, 24, p. 24. arXiv: 1604.02350 [astro-ph.GA].

Lanzuisi, G. et al. (Jan. 2015). "Compton thick AGN in the XMM-COSMOS survey". In: *A&A* 573, A137, A137. arXiv: 1409.1867 [astro-ph.GA].

Lanzuisi, G. et al. (Apr. 2019). "NuSTAR Measurement of Coronal Temperature in Two Luminous, High-redshift Quasars". In: *ApJ* 875.2, L20, p. L20. arXiv: 1904.04784 [astro-ph.HE].

Lilly, S. J. et al. (Sept. 2007). "zCOSMOS: A Large VLT/VIMOS Redshift Survey Covering 0 < z < 3 in the COSMOS Field". In: *ApJS* 172.1, pp. 70–85. arXiv: astro-ph/0612291 [astro-ph].

Lilly, Simon J. et al. (Oct. 2009). "The zCOSMOS 10k-Bright Spectroscopic Sample". In: *ApJS* 184.2, pp. 218–229.

Lo Faro, B. et al. (Jan. 2013). "The Complex Physics of Dusty Star-forming Galaxies at High Redshifts as Revealed by Herschel and Spitzer". In: *ApJ* 762.2, 108, p. 108. arXiv: 1211.6116 [astro-ph.CO].

Lusso, E. et al. (Sept. 2012). "Bolometric luminosities and Eddington ratios of X-ray selected active galactic nuclei in the XMM-COSMOS survey". In: *Monthly Notices of the Royal Astronomical Society* 425.1, pp. 623–640. arXiv: 1206.2642 [astro-ph.CO].

Manske, V., Th. Henning, and A. B. Men'shchikov (Mar. 1998). "Flared dust disks and the IR emission of AGN". In: *A&A* 331, pp. 52–60.

Marchesi, S. et al. (Jan. 2016). "The Chandra COSMOS Legacy survey: optical/IR identifications". In: *ApJ* 817.1, 34, p. 34. arXiv: 1512.01105 [astro-ph.GA].

Mathews, W. G. and E. R. Capriotti (Jan. 1985). "Structure and dynamics of the broad line region". In: *Astrophysics of Active Galaxies and Quasi-Stellar Objects*. Ed. by J. S. Miller, pp. 185–233.

McHardy, I. (Oct. 1990). "Book Review: Discovering the universe - 2nd ed. / W. H. Freeman, 1990". In: *The Observatory* 110.1098, p. 156.

Mignoli, M. et al. (Aug. 2013). "Obscured AGN at z 1 from the zCOSMOS-Bright Survey. I. Selection and optical properties of a [Ne v]-selected sample". In: *A&A* 556, A29, A29. arXiv: 1305.6167 [astro-ph.CO].

Mignoli, M. et al. (June 2019). "Obscured AGN at 1.5 < z < 3.0 from the zCOSMOS-deep Survey . I. Properties of the emitting gas in the narrow-line region". In: *Astronomy and Astrophysics* 626, A9, A9. arXiv: 1903.11085 [astro-ph.GA].

Mor, Rivay, Hagai Netzer, and Moshe Elitzur (Nov. 2009). "Dusty Structure Around Type-I Active Galactic Nuclei: Clumpy Torus Narrow-line Region and Near-nucleus Hot Dust". In: *ApJ* 705.1, pp. 298–313. arXiv: 0907.1654 [astro-ph.CO].

Moretti, A. et al. (Dec. 2012). "Spectrum of the unresolved cosmic X-ray background: what is unresolved 50 years after its discovery". In: *A&A* 548, A87, A87. arXiv: 1210.6377 [astro-ph.CO].

Mushotzky, Richard F., Christine Done, and Kenneth A. Pounds (Jan. 1993). "X-ray spectra and time variability of active galactic nuclei." In: *ARA&A* 31, pp. 717–717.

Nandra, K. and K. A. Pounds (May 1994). "GINGA observations of the X-ray spectra of Seyfert galaxies." In: *MNRAS* 268, pp. 405–429.

Nenkova, Maia, Željko Ivezić, and Moshe Elitzur (May 2002). "Dust Emission from Active Galactic Nuclei". In: *ApJ* 570.1, pp. L9–L12. arXiv: astro-ph/0202405 [astro-ph].

Nesvadba, N. P. H. et al. (June 2008). "Outflows in high-redshift radio galaxies and their relevance for AGN feedback". In: *Gas and Stars in Galaxies - A Multi-Wavelength 3D Perspective*, p. 37.

Noeske, K. G. et al. (May 2007). "Star Formation in AEGIS Field Galaxies since z=1.1: The Dominance of Gradually Declining Star Formation, and the Main Sequence of Star-forming Galaxies". In: *The Astrophysical Journal* 660.1, pp. L43–L46. arXiv: astro-ph/0701924 [astro-ph].

Osterbrock, Donald E. (Feb. 1978). "Observational Model of the Ionized Gas in Seyfert and Radio-Galaxy Nuclei". In: *Proceedings of the National Academy of Science* 75.2, pp. 540–544.

Padovani, P. et al. (Aug. 2017). "Active galactic nuclei: what's in a name?" In: *A&A Rev.* 25.1, 2, p. 2. arXiv: 1707.07134 [astro-ph.GA].

Peca, Alessandro (Sept. 2018). "AGN oscurati nel campo J1030: prospettiva in banda X e ottico/infrarossa". MA thesis. Alma Mater Studiorum - Universita' di Bologna.

Piconcelli, E. et al. (Mar. 2005). "The XMM-Newton view of PG quasars. I. X-ray continuum and absorption". In: *A&A* 432.1, pp. 15–30. arXiv: astro-ph/0411051 [astro-ph].

Pier, Edward A. and Julian H. Krolik (Dec. 1992). "Infrared Spectra of Obscuring Dust Tori around Active Galactic Nuclei. I. Calculational Method and Basic Trends". In: *ApJ* 401, p. 99.

Pogge, Richard W. (Sept. 1988). "Extended Ionized Gas in the Seyfert 2 Galaxy NGC 4388". In: *ApJ* 332, p. 702.

Pozzi, F. et al. (July 2010). "The HELLAS2XMM survey. XIII. Multi-component analysis of the spectral energy distribution of obscured AGN". In: *A&A* 517, A11, A11. arXiv: 1003.5563 [astro-ph.CO].

Pozzi, F. et al. (June 2012). "The AGN content in luminous infrared galaxies at z 2 from a global SED analysis including Herschel data". In: *MNRAS* 423.2, pp. 1909–1920. arXiv: 1204.1152 [astro-ph.CO].

Reis, R. C. and J. M. Miller (May 2013). "On the Size and Location of the X-Ray Emitting Coronae around Black Holes". In: *ApJ* 769.1, L7, p. L7. arXiv: 1304.4947 [astro-ph.HE].

Ricci, C. et al. (Oct. 2018). "BAT AGN Spectroscopic Survey - XII. The relation between coronal properties of active galactic nuclei and the Eddington ratio". In: *MNRAS* 480.2, pp. 1819–1830. arXiv: 1809.04076 [astro-ph.HE].

Sandage, Allan (May 1965). "The Existence of a Major New Constituent of the Universe: the Quasistellar Galaxies." In: *ApJ* 141, p. 1560.

Sanders, D. B. et al. (Feb. 1988). "Ultraluminous Infrared Galaxies and the Origin of Quasars". In: *ApJ* 325, p. 74.

Sanders, D. B. et al. (Dec. 1989). "Continuum Energy Distributions of Quasars: Shapes and Origins". In: *ApJ* 347, p. 29.

Schawinski, Kevin et al. (Feb. 2011). "HST WFC3/IR Observations of Active Galactic Nucleus Host Galaxies at z 2: Supermassive Black Holes Grow in Disk Galaxies". In: *ApJ* 727.2, L31, p. L31. arXiv: 1012.1855 [astro-ph.CO].

Schmidt, M. et al. (Jan. 1998). "The ROSAT deep survey. II. Optical identification, photometry and spectra of X-ray sources in the Lockman field". In: *A&A* 329, pp. 495–503. arXiv: astro-ph/9709144 [astro-ph].

Schreiber, C. et al. (Mar. 2015). "The Herschel view of the dominant mode of galaxy growth from z = 4 to the present day". In: *Astronomy and Astrophysics* 575, A74, A74. arXiv: 1409.5433 [astro-ph.GA].

Scoville, N. et al. (Sept. 2007). "The Cosmic Evolution Survey (COSMOS): Overview". In: *ApJS* 172.1, pp. 1–8. arXiv: astro-ph/0612305 [astro-ph].

Setti, G. and L. Woltjer (Oct. 1989). "Active galactic nuclei and the spectrum of the X-ray background." In: *A&A* 224, pp. L21–L23.

Shakura, N. I. and R. A. Sunyaev (June 1973). "Reprint of 1973A&A....24..337S. Black holes in binary systems. Observational appearance." In: *A&A* 500, pp. 33–51.

Shankar, Francesco, David H. Weinberg, and Jordi Miralda-Escudé (Jan. 2009). "Self-Consistent Models of the AGN and Black Hole Populations: Duty Cycles, Accretion Rates, and the Mean Radiative Efficiency". In: *ApJ* 690.1, pp. 20–41. arXiv: 0710.4488 [astro-ph].

Stenholm, L. (Oct. 1994). "Silicate dust discs as sources of the AGN IR-emission." In: *A&A* 290, pp. 393–398.

Terashima, Yuichi (Oct. 2005). *The Nature of Far Infrared Selected Type 2 QSOs*. XMM-Newton Proposal.

Tombesi, F. et al. (Oct. 2010). "Evidence for ultra-fast outflows in radio-quiet AGNs. I. Detection and statistical incidence of Fe K-shell absorption lines". In: *A&A* 521, A57, A57. arXiv: 1006.2858 [astro-ph.HE].

Tombesi, F. et al. (Apr. 2013). "Unification of X-ray winds in Seyfert galaxies: from ultra-fast outflows to warm absorbers". In: *MNRAS* 430.2, pp. 1102–1117. arXiv: 1212.4851 [astro-ph.HE].

Urry, C. Megan and Paolo Padovani (Sept. 1995). "Unified Schemes for Radio-Loud Active Galactic Nuclei". In: *PASP* 107, p. 803. arXiv: astro-ph/9506063 [astro-ph].

van der Wel, Arjen et al. (Mar. 2006). "Masses and Mass-to-Light Ratios of Early-Type Galaxies at High Redshift ? The Impact of Ultradeep FORS2 Spectroscopy". In: *The Messenger* 123, p. 45.

Vignali, C. et al. (May 2010). "Discovery of Compton-thick quasars in the Sloan Digital Sky Survey". In: *MNRAS* 404.1, pp. 48–59. arXiv: 1001.2005 [astro-ph.CO].

Vignali, C. et al. (Nov. 2014). "The space density of Compton-thick AGN at z ≈ 0.8 in the zCOSMOS-Bright Survey". In: *A&A* 571, A34, A34. arXiv: 1409.6361 [astro-ph.HE].

Weisskopf, Martin C. (2012). "Chandra x-ray optics". In: *Optical Engineering* 51.1, pp. 1 - 8 - 8.

Wilson, A. S. and Z. I. Tsvetanov (Apr. 1994). "Ionization Cones and Radio Ejecta in Active Galaxies". In: *AJ* 107, p. 1227.

Wolter, Hans (Jan. 1952). "Spiegelsysteme streifenden Einfalls als abbildende Optiken für Röntgenstrahlen". In: *Annalen der Physik* 445.1, pp. 94–114.